A Validation Model For the Transient Analysis of Tightly Coupled Reactors

by

Tamer Bahadır

M.S. in Nuclear Engineering, Hacettepe University
Ankara, August 1992
B.S. in Nuclear Engineering, Hacettepe University
Ankara, July 1990

Submitted to the Department of Nuclear Engineering in partial
fulfillment of the requirements for the degree of

DOCTOR OF PHILOSOPHY

at the

MASSACHUSETTS INSTITUTE OF TECHNOLOGY

September 1995

Author ______________________________
Department of Nuclear Engineering
July 13, 1995

Certified by ______________________________
Allan F. Henry
Supervisor

Certified by ______________________________
John E. Meyer
Thesis Reader

Accepted by ______________________________
Jeffrey P. Friedberg
Chairman, Department Committee on Graduate Students

A Validation Model for the Transient Analysis of Tightly Coupled Reactors

by

Tamer Bahadır

Submitted to the Department of Nuclear Engineering
on July 13, 1995, in partial fulfillment of the
requirements for the degree of
DOCTOR OF PHILOSOPHY

Abstract

Both the static and transient analysis of tightly coupled reactors differ from those of the loosely coupled systems, requiring use of at least two-dimensional multigroup, transport methods. Recently a few-group transient nodal method has been developed for tightly coupled reactors. Although the accuracy of the static part of this model can be tested easily, in the absence of a time dependent transport code, direct validation is not possible.

In this study, an indirect test, making use of a static, multigroup, discrete ordinate code, to measure the accuracy of the few-group nodal (as well as any other approximate method) has been developed. The validation is based on the fact that, at any stage during a transient calculation, the transient equations can be converted to a static eigenvalue problem by replacing the time derivatives of group-flux and delayed precursor concentration with instantaneous "frequencies" multiplied into the quantities themselves. These time constants are edited at any time step from the transient analyzed. A test of whether the nodal transient calculation would agree with a transient transport calculation is then to see if the dynamic frequencies inserted into the time-dependent equation (thereby converting it to a static equation) will yield an eigenvalue of unity. Moreover, transient flux shapes should match the corresponding pseudo-static flux shapes.

Various reactivity transients of the two- and three-element Advanced Neutron Source Reactor are analyzed by a few-group, space-time nodal model, an adiabatic approximation, and the point-kinetics model with and without thermal feedback. Applying the indirect procedure the relative accuracy with which transient behavior is predicted was found to correlate well with the closeness to unity of the pseudo-static eigenvalues using the dynamic frequencies obtained from transient models during the course of the transient.

Thesis Supervisor:	Allan F. Henry
Title:	Professor, Department of Nuclear Engineering

Acknowledgment

I would like to express my deepest gratitude to my thesis supervisor Professor Allan F. Henry, for his guidance and supervision. This research has largely benefited from his original ideas and great expertise. It has truly been a pleasure and an honor working with Professor Henry throughout my stay at MIT.

I am indepted to my undergraduate advisor, Prof. Dr. Osman K. Kadiroglu, for his guidance, support and trust in me. Without him, none of this would have been possible. I also would like thank my undergraduate co-advisor Prof. Dr. Yalçın Sanalan.

Thanks are also due Prof. Meyer who serves as a thesis reader.

I am gratefull for the superb educational environment and support by MIT Nuclear Enginnering Department. The financial support received from the Oak Ridge National Laboratoary is also gratefully acknowledged.

I would like to thank my friends at MIT: Erol Çubukcu, Sinan Keskin, Volkan Kubalı, Serhat Yesilyurt, Jeff Hughes and Paul Chodak for their support and friendship. I also would like to thank my friends Nejat Ugur and Dennis Butler for their company.

Last, but not least, I owe eternal gratitude to my family and my fiancee, Sibel, for their continuous encouragement and love. I am looking forward to a beautiful life with her.

Table of Contents

Chapter 1

Chapter 2

LIST OF FIGURES

LIST OF TABLES

Chapter 1

Introduction

1.1 Overview and Background

Accurate information about the neutron distribution in space, energy and time is essential for the analysis of any nuclear reactor. For the last two decades, for neutronic analysis, traditionally used diffusion theory models employing the finite difference approximation have been replaced with modern nodal methods. These methods reduce computational cost. In addition, situations where diffusion theory is invalid, such as near regions containing highly absorbing material (e.g. control rods) or near interfaces between regions having different scattering properties, are improved by introducing correction factors. For light water reactors, the correction factors, usually called discontinuity factors, are obtained from independent, detailed calculations (ideally fine mesh transport calculations with heterogeneity explicitly represented) for a few, representative assemblies with zero current or known albedo boundary conditions.

The accuracy of these and other approximate methods has been tested both theoretically and experimentally for static solutions. Although, for obvious reasons, experimental validation is prohibited for the severe transient analysis, validations have been made in many different ways by obtaining reference solutions numerically [Y-1, O-1, K-1]. Since the early days of nuclear technology, as a result of the studies conducted much experience has been gained about analysis methods and their accuracy for loosely coupled reactors.

However, for the reactors having long neutron mean free paths comparable to node sizes, the situation is significantly different. First of all, there is strong neutron coupling preventing generation of homogenized cross sections and correction factors from independent assembly size transport calculations. Also for these tightly coupled reactors, high absorbing regions are usually interspaced with low absorbing regions. That raises questions of the acceptability of the diffusion theory approximations. Finally, the spectral shapes change drastically throughout the core and can be altered significantly by perturbations. For accurate analysis, describing all these behaviors requires the use of at least two-dimensional, full core, multigroup transport methods. This requirement raises a problem: There are many static transport codes available for steady-state calculations (although they are very expensive in terms of computing time compare to diffusion theory models). However, there is no time-dependent transport code (two-dimensional, multigroup, discrete ordinate) that can be used for transient analysis.

The neutronic characteristics of reactors proposed for space-flight and for advanced neutron sources exhibit all the features discussed above for tightly coupled reactors. The Advanced Neutron Source (ANS) reactor is a new experimental facility originally planned (but now cancelled) for the Oak Ridge National Laboratory (ORNL) to meet the need for an intense steady state neutron source [R-1]. This small, high power density, high leakage, tightly coupled core is difficult to analyze and require the use of advanced reactor physics methods. Much research has gone into the steady-state and transient analysis of the ANS.

Early studies performed by Azmy and Ryskamp *et al.* from Oak Ridge National Laboratory and Idaho National Engineering Laboratory (INEL) showed that diffusion theory is not accurate enough for the ANS reactor [A-1, R-2]. Because of a small compact core, high fuel enrichments (varying from 93% to 50% for different core designs), and low D_2O moderator/coolant content in the core, the thermal flux gradient in the core and the fast flux gradient in the large D_2O reflector pool are extremely large, raising questions about the accuracy of diffusion calculations. Accordingly, a discrete ordinate transport method has been used for the conceptual design studies. The accuracy of the method has been tested for static calculations by Azmy [A-2].

Monte Carlo procedures are also attractive methods of analysis since complex geometries can be modelled easily. Redmond has shown the acceptability of the Monte Carlo code MCNP [B-1] for the analysis of the ANS [R-3]. He also performed some preliminary studies for transient analysis [R-4] using the Cartesian geometry, analytic nodal code QUANDRY [S-1]. Byers, in his thesis, used the *r-z* geometry nodal code ZAQ, and analyzed the control rod removal transient [B-2]. Redmond and Byers reached the conclusion that the point kinetics approximation is not accurate for transient analysis and that a space-time model is needed. In parallel with these studies, the use of a two-point kinetics model by Difilippo *et al.* also indicated that, if the transient is severe, it becomes sensitive to spatial effects which can not be described by the point kinetics approximation [D-1].

Recently a transient nodal method incorporating transport corrections was developed by

Mohamed [M-1]. In this model, few-group node-averaged cross sections and discontinuity factors are edited from full core (or to reduce the cost, where applicable, from partial core calculations) higher order reference multigroup transport solutions for various conditions expected during transients. For the transient problems, tables of nodal parameters are constructed, and their values as the transient proceeds are found by interpolation. Mohamed first suggested using Monte Carlo methods to generate these tables. However, statistical uncertainties associated with the Monte Carlo results prevented him from making precise, quantitative statements about the acceptability and accuracy of the method. He then used a multigroup discrete ordinate code for the same purpose and applied the method to rod ejection transients of the two-element ANS core.

It is not difficult to test the accuracy of the few-group nodal model for static cases. Using the transport code, the case in question can be analyzed and compared with the nodal results. However, without a time dependent transport code, the analogous validation for the time dependent problem is not possible.

1.2 Research Objectives

The main objective of this work is to develop a model which can be used to validate a space-time nodal model for tightly coupled reactors. The core characteristics of these reactors require multigroup, transport methods for validation. Since the direct validation by using a time-dependent multigroup, discrete ordinate code is not presently possible, the goal is achieved by an indirect method. The procedure is based on the fact that, at any stage during a transient calculation, transient equations can be converted to a static eigenvalue problem by replacing the time derivatives of group-fluxes and delayed precursor concentrations with "frequencies" multiplied into the quantities themselves. A static, multigroup, discrete ordinate code can then be used for validation.

The good test of whether the nodal transient calculation would agree with a transient transport calculation is to see if, when the dynamic frequencies are inserted into the time-dependent transport equation (thereby converting it to a static equation), an eigenvalue of unity results. Also, the flux shapes found from the transient model should match the corresponding pseudo-static flux shapes.

It is always desirable to have an inexpensive, acceptably accurate model for both static and transient analysis. If the space and time behaviors of the neutron flux are close to being separable, approximate methods such as the point-kinetics or adiabatic model will yield acceptably accurate results. An adiabatic model has been considered for the safety analyses of the ANS reactor by the design team. The second objective of this research is to investigate when these approximate methods can be used for tightly coupled reactor transients. This goal can be achieved by applying the indirect test described above and/or comparing results with theoretically more accurate space-time solutions if they can be generated.

Accurate analysis requires neutronic, thermal-hydraulic coupling. By incorporating a simple thermal feedback model, we shall investigate whether local values of changes in thermal-hydraulic properties (fuel temperature, moderator density etc.) must be used to predict accurate transient behavior or whether core-averaged values can be used.

The models and tests described in this study have been applied to the two- and three-element Advanced Neutron Source reactors. Our final objective is to perform for this reactor neutronic analysis of various transients.

1.3 Thesis Organization

Chapter 2 is devoted to background considerations. The few-group nodal diffusion theory model incorporating transport corrections is reviewed. First the steady-state finite difference nodal equations are derived. Then the use of Monte Carlo and discrete ordinate procedures to obtain the nodal parameters required for both the static and transient model is discussed. Finally, various transient models are outlined.

In Chapter 3, the procedure to validate the few-group diffusion theory model based on cross sections and discontinuity factors found from higher order reference solutions is developed. The pseudo-static diffusion and transport equations are derived starting from their time-dependent forms. The calculational steps of the validation procedure are discussed in detail.

In Chapter 4, application of the validation procedure for various reactivity transients involving the Advanced Neutron Source reactor is presented. The control rod withdrawal and the light water ingress events without feedback are analyzed by three different transient models, and the accuracy of the results is assessed.

Since feedback effects change the development of transients significantly, in Chapter 5, a simple feedback model is incorporated for the ANS reactor, and the reactivity transients are reevaluated.

Finally, Chapter 6 presents a summary and conclusions of this research. Recommendations for further research are also made.

Chapter 2

Theoretical Background

2.1 Introduction

This chapter contains background considerations that are used in the remaining portions of the dissertation. First, the theory underlying tightly coupled reactor neutronic analysis will be reviewed. For both static and transient analysis, the few-group nodal diffusion theory model including transport corrections will be summarized. For a complete description of that model, the reader is advised to consult reference [M-1]. Next, various time-dependent solution models used in this study will be outlined.

2.2 A Nodal Diffusion Theory Model Accounting Transport Corrections

The static and transient analysis of tightly coupled reactors differs from light water reactor analysis. Spectral shapes change dramatically with position in such reactors and can be altered significantly by perturbations. For that reason accurate analysis requires at least a two-dimensional multigroup, transport treatment. Although for static cases such methods can be applied, for transient analysis they would now be almost impossibly expensive.

One way around this difficulty is to apply a few-group nodal model, corrected by discontinuity factors, for the analysis of transients. According to a scheme proposed by Amr Mohamed [M-1], spatially-homogenized, few-group cross sections are edited from higher order reference transport solutions for various conditions expected during the transient; tables of the few-group parameters as a function of the variables of the transient (such as control rod position or coolant density etc.) are constructed, and the few-group, node-homogenized cross sections and discontinuity factors are found by interpolation as the transient progresses.

In subsequent sections, the elements of the neutronic model for tightly coupled reactors will be summarized: first the nodal equations will be derived from the static diffusion equation; then two candidates for a higher order reference solution (the Monte Carlo and discrete ordinate procedures) will be outlined.

2.3 Static Nodal Equations

Since our primary application is to the Advanced Neutron Source reactor, the nodal equations will be derived in *r-z* geometry which is the most suitable geometry for this reactor. A complete derivation can be found in reference [B-2].

Our starting point for the derivation is the few-group, steady state diffusion equation in P_1 form without any extraneous neutron source [H-1]

$$\nabla\cdot J_g(\underline{r})+\Sigma_{tg}(\underline{r})\phi_g(\underline{r}) = \sum_{g'=1}^{G}\left[\frac{1}{\lambda}\chi_g\nu\Sigma_{fg'}(\underline{r})+\Sigma_{gg'}(\underline{r})\right]\phi_{g'}(\underline{r}) \tag{2.1}$$

$$J_g(\underline{r}) = -D_g(\underline{r})\nabla\phi_g(\underline{r}) \tag{2.2}$$

where

$J_g(\underline{r})$ = net neutron current in group-g ($cm^{-2}s^{-1}$),

$\phi_g(\underline{r})$ = scalar neutron flux in group-g ($cm^{-2}s^{-1}$),

λ = reactor eigenvalue,

$\Sigma_{tg}(\underline{r})$ = macroscopic total cross section for group-g (cm^{-1}),

χ_g = fission spectrum for group-g,

$\nu\Sigma_{fg}(\underline{r})$ = mean number of neutrons emitted per fission times the macroscopic fission cross section for group-g (cm^{-1}),

$\Sigma_{gg'}(\underline{r})$ = macroscopic transfer cross section from g' to g (cm^{-1}),

$D_g(\underline{r})$ = diffusion coefficient for group-g (cm),

G = total number of energy groups.

For cylindrical geometry, defining nodes that are each hollow right circular cylinders bounded above and below by planes normal to the axis of the reactor, and then integrating the few-group diffusion equation over the volume of a node and using Gauss's divergence theorem, yields the following balance equation

$$2\pi\Delta z_k\left[\mathcal{J}^k_{gr}(r_{i+1})r_{i+1}-\mathcal{J}^k_{gr}(r_i)r_i\right]+\pi\left(r^2_{i+1}-r^2_i\right)\left[\mathcal{J}^i_{gr}(z_{k+1})-\mathcal{J}^i_{gr}(z_k)\right] \tag{2.3}$$
$$+\Sigma^{i,k}_{tg}\bar{\phi}^{i,k}_g V^{i,k} = \sum_{g'=1}^{G}\left[\frac{1}{\lambda}\chi^{i,k}_g\nu\Sigma^{i,k}_{fg'}+\Sigma^{i,k}_{gg'}\right]\bar{\phi}^{i,k}_{g'}V^{i,k}$$

where

$$\mathcal{J}^k_{gr}(r) = \frac{2\pi r\int_{z_k}^{z_{k+1}} dz J_{gr}(r,z)}{2\pi r\Delta z_k}\ , \tag{2.4}$$

$$\mathcal{J}^i_{gz}(z) = \frac{2\pi\int_{r_i}^{r_{i+1}} r dr J_{gz}(r,z)}{\pi\left(r^2_{i+1}-r^2_i\right)}\ , \tag{2.5}$$

$$\bar{\phi}^{i,k}_g = \frac{\int_{r_i}^{r_{i+1}} 2\pi r dr\int_{z_k}^{z_{k+1}} dz\phi_g(r,z)}{V^{i,k}}\ , \tag{2.6}$$

$$\Sigma^{i,k}_{\alpha g} = \frac{\int_{r_i}^{r_{i+1}} 2\pi r dr\int_{z_k}^{z_{k+1}} \Sigma_{\alpha g}(r,z) dz\phi_g(r,z)}{\int_{r_i}^{r_{i+1}} 2\pi r dr\int_{z_k}^{z_{k+1}} dz\phi_g(r,z)}\ , \tag{2.7}$$

$$V^{i,k} = \int_{r_i}^{r_{i+1}} 2\pi r dr\int_{z_k}^{z_{k+1}} dz = \pi\left(r^2_{i+1}-r^2_i\right)\Delta z_k\ . \tag{2.8}$$

The currents in these equations can be expressed in terms of the fluxes using the second P_1 equation (2.2). For example, on the outer radial face of the node *i,k*, integrating the $J_{gr}(r)$ from z_k to z_{k+1}, we obtain:

$$\mathcal{J}^{i,k}_{gr}(r_{i+1}) \equiv -D^{i,k}_g\frac{d}{dr}\left(\frac{2\pi r}{2\pi r\Delta z_k}\int_{z_k}^{z_{k+1}} dz\phi_g(r,z)\right). \tag{2.9}$$

One can approximate the derivative in this equation as a simple difference as follows

$$J_{gr}^{i,k}(r_{i+1}) \equiv -D_g^{i,k}\frac{\left[\bar{\phi}_g^{i,k} - \phi_{gr}^{i,k}(r_{i+1})\right]}{\Delta r_i/2} \tag{2.10}$$

where the surface-averaged flux on the outer nodal face is defined by

$$\phi_{gr}^{i,k}(r_{i+1}) = \frac{2\pi\int_{z_k}^{z_{k+1}} dz\phi_g(r,z)}{2\pi\Delta z_k} \quad . \tag{2.11}$$

Substituting these expressions, along with analogous expressions for the current across the other surfaces of a node, yields one of the standard finite-difference forms of the group diffusion equations. However, since equation (2.10) is an approximation, the resultant equation is not very accurate, especially for large node sizes. There are also errors coming from node averaged cross sections. This difficulty is overcome by altering equation (2.10) so that it is forced to be exact. One scheme is to force (2.10) to be correct by dividing the surface fluxes on the both sides of each nodal interface by correction factors. Since these correction factors for each side of the same surface are generally not equal, the corrected surface averaged fluxes must be discontinuous. For that reason, these correction factors are called *discontinuity factors* [H-2]. If reference values of the currents and the fluxes in eq (2.10) are known, then we can define the discontinuity factors on the plus and minus side of the radial interface between nodes *i,k* and *i+1,k* at r_{i+1} so that,

$$J_{gr}^{i,k}(r_{i+1})^{+} \equiv -D_g^{i+1,k}\frac{\left[\bar{\phi}_g^{i,k} - \phi_{gr}^{i,k}(r_{i+1})/f_{gr}^{i+1,k-}\right]}{\Delta r_{i+1}/2} \tag{2.12}$$

$$J_{gr}^{i,k}(r_{i+1})^{-} \equiv -D_g^{ik}\frac{\left[\phi_{gr}^{i,k}(r_{i+1})/f_{gr}^{i,k+} - \bar{\phi}_g^{i,k}\right]}{\Delta r_i/2} \tag{2.13}$$

Since the face averaged current is continuous, equations (2.12) and (2.13) can be combined to yield:

$$J_{gr}^{i,k}(r_{i+1}) = \left[\frac{\Delta r_i}{2D_g^{i,k}} - \frac{f_{gr}^{i+1,k-}}{f_{gr}^{i,k+}}\frac{\Delta r_{i+1}}{2D_g^{i+1,k}}\right]^{-1}\left(\bar{\phi}_g^{i,k} - \frac{f_{gr}^{i+1,k-}}{f_{gr}^{i,k+}}\bar{\phi}_g^{i+1,k}\right) \tag{2.14}$$

One of the important properties of this corrected finite-difference coupling equation is that discontinuity factors appear as a ratio. This ratio for the equation given above can be expressed as:

$$\frac{f_{gr}^{i+1,k-}}{f_{gr}^{i,k+}} = \frac{2D_g^{i,k}\bar{\phi}_g^{i,k} - \Delta r_i J_{gr}^{i,k}(r_{i+1})^{+}}{2D_g^{i+1,k}\bar{\phi}_g^{i+1,k} + \Delta r_{i+1} J_{gr}^{i,k}(r_{i+1})^{-}} \cdot \frac{D_g^{i+1,k}}{D_g^{i,k}} \tag{2.15}$$

Deriving similar discontinuity factor ratios and current expressions for other faces, and introducing them into the nodal balance equation, permits rewriting the nodal balance equation as;

$$\begin{aligned}
&\frac{2\pi r_{i+1}\Delta z_k}{V^{i,k}}\left[\frac{\Delta r_i}{2D_g^{i,k}} - \frac{f_{gr}^{i+1,k-}}{f_{gr}^{i,k+}}\frac{\Delta r_{i+1}}{2D_g^{i+1,k}}\right]^{-1}\left(\bar{\phi}_g^{i,k} - \frac{f_{gr}^{i+1,k-}}{f_{gr}^{i,k+}}\bar{\phi}_g^{i+1,k}\right)\\
&+\frac{2\pi r_i\Delta z_k}{V^{i,k}}\left[\frac{\Delta r_i}{2D_g^{i,k}} - \frac{f_{gr}^{i-1,k+}}{f_{gr}^{i,k-}}\frac{\Delta r_{i-1}}{2D_g^{i-1,k}}\right]^{-1}\left(\bar{\phi}_g^{i,k} - \frac{f_{gr}^{i-1,k+}}{f_{gr}^{i,k-}}\bar{\phi}_g^{i-1,k}\right)\\
&+\frac{\pi\left(r_{i+1}^2 - r_i^2\right)}{V^{i,k}}\left[\frac{\Delta z_k}{2D_g^{i,k}} - \frac{f_{gz}^{i,k+1-}}{f_{gz}^{i,k+}}\frac{\Delta z_{k+1}}{2D_g^{i,k+1}}\right]^{-1}\left(\bar{\phi}_g^{i,k} - \frac{f_{gz}^{i,k+1-}}{f_{gz}^{i,k+}}\bar{\phi}_g^{ik+1}\right)\\
&+\frac{\pi\left(r_{i+1}^2 - r_i^2\right)}{V^{i,k}}\left[\frac{\Delta z_k}{2D_g^{i,k}} - \frac{f_{gz}^{i,k-1+}}{f_{gz}^{i,k-}}\frac{\Delta z_{k-1}}{2D_g^{i,k-1}}\right]^{-1}\left(\bar{\phi}_g^{i,k} - \frac{f_{gz}^{i,k-1+}}{f_{gz}^{i,k-}}\bar{\phi}_g^{ik-1}\right)\\
&+\Sigma_{tg}^{i,k}\bar{\phi}_g^{i,k} = \sum_{g'=1}^{G}\left[\frac{1}{\lambda}\chi_g^{i,k}\nu\Sigma_{fg'}^{i,k} + \Sigma_{gg'}^{i,k}\right]\bar{\phi}_{g'}^{i,k}
\end{aligned} \tag{2.16}$$

If all of the discontinuity factors are set to unity, the above equation simplifies to the coarse mesh finite difference equation. With the appropriate boundary conditions, the corrected finite difference equations yield very accurate results for the reactor eigenvalue and flux distributions provided that good approximations for the homogenized cross sections and discontinuity factor ratios can be found. (Exact homogenized cross sections and discontinuity factors yield exact eigenvalues and flux distributions.)

In the next two section, we shall describe how the few-group node homogenized cross-sections and discontinuity factor ratios appearing in Equation (2.16) can be edited from higher order reference solutions.

2.4 Monte Carlo Methods

One transport theory method that can be used to get the corrected finite difference equation parameters is the Monte Carlo technique. As the name suggest, the Monte Carlo method is a statistical procedure wherein the expected characteristics of a neutron population in a reactor are estimated by drawing samples from a large number of case histories of neutrons whose individual lives are simulated. This method is best suited for the analysis of geometrically complex reactors for which other numerical schemes are extremely time consuming.

A general purpose, continuous-energy, generalized-geometry, coupled neutron/photon Monte Carlo transport code MCNP [B-1] has been widely used by many authors for the neutronic analysis of the Advanced Neutron Source as well as other geometrically complex reactors [R-3, H-3]. However none of these early studies attempted to edit few-group parameters from the Monte Carlo calculations.

In his dissertation [M-1], Mohamed, first attempted to use MCNP, and investigated the acceptability of the Monte Carlo technique for editing the required nodal parameters at different times during a transient.

The case analyzed was the removal of the one of the central control rods of the two element ANS core. (The core description can be found in Appendix A-1.) For that transient, full core criticality calculations were performed for the central control rod in three different locations (fully inserted, half removed from the first node, fully withdrawn from the first node). Two-group homogenized cross sections and discontinuity factor ratios for the *r-z* nodal code ZAQ were edited from the MCNP calculations.

The Monte Carlo code MCNP edits reaction rates and fluxes (and hence energy- group cross sections) only over homogeneous material compositions. To avoid modelling each composition separately, the graded fuel was simulated as homogeneous. Using the total, absorption, fission, and nu-fission interaction rate tallies from the MCNP calculations for each node *(i,k)*, Σ_{tg}, Σ_{ag}, Σ_{fg}, and $\nu\Sigma_{fg}$ were determined by

$$\Sigma_{\alpha,g}^{i,k} = \frac{\alpha\text{-}type\ interaction\ rate\ in\ node\ (i,k)}{volume\ \text{-}\ integrated\ flux\ in\ node\ (i,k)}. \tag{2.17}$$

Edits for the discontinuity factor ratios were made using equation (2.15) for the finite difference model. In those expressions the diffusion coefficients were arbitrarily set to

$$D_g^{i,k} = \frac{1}{3\Sigma_{tg}^{i,k}}. \tag{2.18}$$

Unfortunately MCNP does not edit scattering events so that group-to-group scattering cross section had to be determined by neutron balance. Specifically, the homogenized group-one to-group-two cross section, Σ_{21}, for the nodes could be edited from either the group-one or group-two balance equation. Because of statistical errors (particularly in the current terms) and failure to account for *(n,2n)* and upscattering events, the two values of Σ_{21} did not agree. For the test cases the thermal group balance, which had better statistics compared to the fast group, was used.

Because of the way they are defined, the discontinuity factors were expected to force the nodal equation to match exactly results edited from the reference Monte Carlo calculations. But results showed that this did not happen. The difference in the eigenvalue and fluxes between the reference and nodal exact results were higher than the statistical error in the MCNP predictions.

The discrepancy was even larger when nodal parameters for the partially inserted rod were found by interpolation from the rod-in and rod-out data and compared with reference, partially inserted MCNP calculations. The error in the nodal flux was as great as 60% for the axial node below the node containing the partially inserted rod. Attempts to improve matters, by running extra MCNP cases for intermediate rod positions and applying a least square fit before interpolating, were successful. However statistical fluctuations in the MCNP results, prevented them making precise, quantitative statements about the accuracy with which homogenized nodal parameters can be found by Monte Carlo methods.

Because of this failure, attention was switched to deterministic discrete ordinate procedures [M-1].

2.5 Discrete Ordinates Transport Methods

We shall start our discussion from the time independent transport equation, and its solution using discrete ordinate methods and then outline how few-group parameters can be edited from a discrete ordinate solution.

2.5.1 Theory

The time-independent Boltzman transport equation for the directional flux density $\Psi(r,\Omega,E)$ is [H-1]

$$\begin{aligned}&\underline{\Omega}\cdot\nabla\Psi(\underline{r},\underline{\Omega},E)+\Sigma_t(\underline{r},E)\Psi(\underline{r},\underline{\Omega},E)\\ &=\int dE'\int d\underline{\Omega}'\left[\frac{\chi(E)}{\lambda}\nu\Sigma_f(\underline{r},E')+\Sigma_s(\underline{r},\underline{\Omega}'\rightarrow\underline{\Omega},E'\rightarrow E)\right]\Psi(\underline{r},\underline{\Omega},E')\end{aligned} \tag{2.19}$$

where

$\underline{\Omega}\cdot\nabla\Psi(\underline{r},\underline{\Omega},E)\,dEd\underline{\Omega}dV$ = rate at which the number of neutrons in volume dV change because of leakage in the range dEdΩ,

$\Sigma_t(\underline{r},E)\Psi(\underline{r},\underline{\Omega},E)\,dEd\underline{\Omega}dV$ = rate at which neutrons in dEdΩ are removed by absorption and scattering from the volume dV,

$\int dE'\int(d\underline{\Omega}'\chi(E)\nu\Sigma_f(\underline{r},E')\Psi(\underline{r},\Omega',E'))\,dV$ = rate at which fission neutrons in dV appear in the range dEdΩ,

$\int dE'\int(d\underline{\Omega}'\Sigma_s(\underline{r},\underline{\Omega}'\rightarrow\underline{\Omega},E'\rightarrow E)\Psi(\underline{r},\underline{\Omega}',E'))\,dV$ = rate at which neutron enter dEdΩ in dV due to scattering,

λ = reactor eigenvalue.

There are several deterministic methods that provide solutions to the neutron transport equation. The first two of them, the spherical harmonics and Fourier-Transform techniques are intractable for complex situations. For these geometrically complex problems, the discrete ordinate method has become the most important tool for obtaining the numerical solution for the integrodifferantial form of the transport equation. In reactor physics calculations, the discrete ordinate method, which has its earlier roots in radiation transport calculations, looks for solution to the transport equation in a number of discrete angular directions. Thus the unknown function $\Psi(r,\Omega,E)$ is replaced by the *D* functions $\Psi(r,\Omega_d,E)$ (d=1,...,D) and the left-hand side of (2.19) is replaced by .

$$\underline{\Omega}_d \cdot \nabla\Psi(\underline{r},\underline{\Omega}_d,E) + \Sigma_t(\underline{r},E)\Psi(\underline{r},\underline{\Omega}_d,E) \; .$$

By expanding the angular dependency of the flux in an infinite series of spherical harmonics $Y_n^m(\underline{\Omega})$, the directional flux density can be written as,

$$\Psi(\underline{r},\underline{\Omega},E) = \sum_{n=0}^{\infty} \sum_{m=-n}^{n} \Psi_n^m(\underline{r},E) Y_n^m(\underline{\Omega}) \; . \tag{2.20}$$

The expansion coefficients are defined formally as

$$\Psi_n^m(\underline{r},E) = \int d\underline{\Omega} \bar{Y}_n^m(\underline{\Omega})\Psi(\underline{r},\underline{\Omega},E) \tag{2.21}$$

where $\bar{Y}_n^m$ is the complex conjugate of Y_n^m. Similarly scattering kernels can be written using Legendre polynomials:

$$\Sigma_s(\underline{r},E' \rightarrow E,\mu_0) = \sum_{l=0}^{\infty} (2n+1)\Sigma_{sl}(\underline{r},E' \rightarrow E) P_n(\mu_0) \tag{2.22}$$

where

$$\mu_0 = \underline{\Omega}' \cdot \underline{\Omega} \text{ and } \Sigma_{sl}(\underline{r},E' \rightarrow E) = \int_{-1}^{1} \frac{d\mu_0}{2} \Sigma_s(\underline{r},E' \rightarrow E,\mu_0) P_n(\mu_0) \; .$$

In the discrete ordinate treatment of angle, the integral over Ω becomes a summation

$$\int d\underline{\Omega} f(\underline{\Omega}) \cong \sum_{d=1}^{D} w_d f_d \; , \tag{2.23}$$

where w_d 's are a set of quadrature weights chosen in such a way that the sum matches the integrals as closely as possible.

Accordingly, expanding $\Psi(\underline{r}, \underline{\Omega}', E)$ as in eq. (2.20) and $\Sigma_s(\underline{r}, E' \rightarrow E, \underline{\Omega}' \rightarrow \underline{\Omega})$ as in eq. (2.22), making use of relation (2.23) and terminating the polynomial expansion (2.22) at $l=L$, the Boltzman transport equation given in (2.19) is replaced by D equations for the $\Psi(\underline{r}, \Omega_d, E)$. For example in two-dimensional *r-z* geometry the transport equations becomes:

$$\frac{\Omega_{rd}}{r}\frac{\partial}{\partial r}(r\Psi(\underline{r},\Omega_d,E)) + \Omega_{zd}\frac{\partial}{\partial z}\Psi(\underline{r},\Omega_d,E) + \Sigma_t(\underline{r},E)\Psi(\underline{r},\Omega_d,E) \tag{2.24}$$

$$= \int dE' \left\{ \frac{\chi(E)}{\lambda}\nu\Sigma_f(\underline{r},E') \sum_{d'=1}^{D} w_{d'}\Psi(\underline{r},\Omega_{d'},E') \right.$$

$$\left. + \sum_{n=0}^{L}\sum_{m=-n}^{n} \Sigma_{sn}(\underline{r},E'\rightarrow E)\left[\sum_{d'=1}^{D} w_{d'}Y_n^m(\Omega_{d'})\Psi(r,\Omega_{d'},E')\right]Y_n^m(\Omega_{d'}) \right\} \qquad d=1,\ldots,D$$

These equations are referred to as S_N equations. The mathematical form of the equations is much better suited to solution by iterative procedures than the spherical harmonics equations.

For the numerical solution, the energy variable can be discretized by first partitioning the energy range into intervals (energy groups). Then the equation is integrated over each energy group ΔE_n, and the integral over E' is replaced by a sum over all energy groups.

The group fluxes are defined as

$$\Psi_g(\underline{r},\underline{\Omega}) = \int_{\Delta Eg} dE\Psi(\underline{r},E,\underline{\Omega}) \ .$$

The spatial domain of the problem is partitioned into fine mesh intervals, and the cross-sections are taken to be piecewise continuous in these intervals.

2.5.2 TWODANT Multigroup Transport Code

TWODANT [A-3] is a two-dimensional multigroup discrete ordinate transport code developed by Los Alamos National Laboratory. It has been used to generate cross sections sets and discontinuity factors required for the static as well as transient analysis of the ANS. It solves the multigroup form of the steady state Boltzman transport equation in *x-y, r-z* and *r-theta* geometries. The discrete ordinates form of approximation is used for treating the angular variation of the particle distribution and the diamond difference scheme is used for space angle discretization. For the iterative solution a standard inner (within group) iteration, outer (energy-dependent source) iteration technique is used. Both inner and outer iterations are accelerated using the diffusion synthetic acceleration method. The diffusion solver uses the multigroup method and Chebychev acceleration of the fission source. The details of the code features and iteration strategy can be found in reference [A-3].

2.5.3 Nodal Parameters Edits

In this section, we describe how coarse mesh few-group nodal parameters, derived in Section 2.3, can be edited using fine mesh multigroup transport code TWODANT results. Figure 2.1 shows the fine and coarse mesh layout in *r-z* geometry.

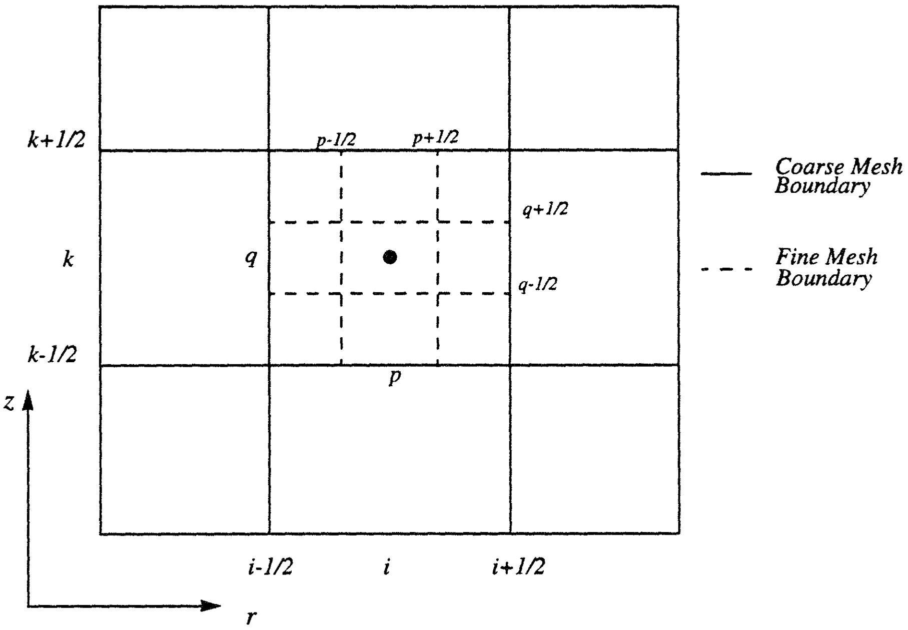

Figure 2.1: Cell centered spatial mesh in *r-z* geometry

As was discussed in Section 2.3, surface-averaged currents and node averaged fluxes are needed for the determination of the nodal parameters. The converged multigroup directional fluxes will be written as $\Psi_{n,d}^{p,q}$ where p and q are indices for fine mesh (similarly i,k are indices for coarse mesh), n is the index for energy-group, and d is one of the chosen directions. Using the converged $\Psi_{n,d}^{p,q}$, the nodal parameters are calculated as follows:

The multigroup scalar fluxes, $\phi_n^{p,q}$, for each fine mesh *(p,q)* and the currents at each fine mesh boundary, $J_n^q\left(r_{p+\frac{1}{2}}\right)$, are approximated by

$$\phi_n^{p,q} = \sum_{d=1}^{D} w_d \Psi_{n,d}^{p,q} \tag{2.25}$$

$$J_n^q(r_{p+1/2}) = \sum_{\mu_d>0} w_d \mu_d \Psi_{n,d}^{p+1/2,q} - \sum_{\mu_d<0} w_d |\mu_d| \Psi_{n,d}^{p+1/2,q} . \tag{2.26}$$

As a next step, multigroup fluxes and cross sections for each coarse mesh are calculated applying flux-volume weighting and preserving the reaction rates. For example, the volume weighted flux, $\bar{\phi}_n^{i,k}$, and α-type average cross section, $\Sigma_{\alpha n}^{i,k}$, for coarse mesh *(i,k)*, which comprises fine meshes *(p,q)*'s, are respectively,

$$\bar{\phi}_n^{i,k} = \frac{\sum\limits_{p\subset i, q\subset k} \phi_n^{p,q} V^{p,q}}{V^{i,k}} , \tag{2.27}$$

$$\Sigma_{\alpha n}^{i,k} = \frac{\sum\limits_{p\subset i, q\subset k} \Sigma_{\alpha n}^{p,q} \phi_n^{p,q} V^{p,q}}{\bar{\phi}_n^{i,k} V^{i,k}} \tag{2.28}$$

where *V* is the either fine or coarse mesh volume.

For the currents, if A^q is the surface area of the right face of fine mesh node *(p,q)* and A^k is the surface area of the right face of coarse mesh *(i,k)* for which we want to find the surface averaged current, then,

$$J_n^k = \frac{\sum\limits_{z_k \le z_q \le z_{k+1}} J_n^q(r_{p+1/2}) A^q}{A^k} . \tag{2.29}$$

Finally, the few-group parameters can be found from,

$$\Sigma_{\alpha g}^{i,k} = \frac{\sum\limits_{n\subset g} \Sigma_{\alpha n}^{i,k} \bar{\phi}_n^{i,k}}{\sum\limits_{n\subset g} \bar{\phi}_n^{i,k}} \quad , \quad \Sigma_{gg'}^{i,k} = \frac{\sum\limits_{n\subset g} \sum\limits_{n'\subset g'} \Sigma_{nn'}^{i,k} \bar{\phi}_{n'}^{i,k}}{\sum\limits_{n'\subset g'} \bar{\phi}_{n'}^{i,k}} .$$

where the symbol $\sum\limits_{n\subset g}$ indicates a sum over all multigroups having *n* energy intervals ΔE_n lying in the larger energy interval ΔE_g.

The diffusion coefficient appearing in the discontinuity factor ratios can be set to

$D_g^{i,k} = \frac{1}{3\Sigma_{tg}^{i,k}}$ for isotropic scattering, and

$D_g^{i,k} = \frac{1}{3[\Sigma_{tg}^{i,k} - \Sigma_{g1}^{i,k}]}$ for the anisotropic scattering where Σ_{g1} is the P_1 component of the group-g scattering cross section.

2.5.4 Early ANS Studies with the Discrete Ordinate Transport Code TWODANT

For deterministic models, homogenized nodal cross sections and discontinuity factors that cause the nodal model to match, exactly, the reference results can always be found. In his thesis, Mohamed investigated how to do so at minimum expense [M-1]. He first showed that discrete ordinate methods can be used to generate nodal parameters for tightly coupled reactor analysis. As with the MCNP studies discussed in Section 2.4, the case analyzed was the removal of one of the control rods from the two-element ANS core. When nodal solution (ZAQ) results were compared with reference TWODANT results, it was found that the eigenvalue agreed to within roundoff and the fluxes to within 0.1% for the nodes in the outer reflector (where the values were a factor of 10^{10} lower than those in the core) and to within roundoff in the interior of the reactor.

When interpolated nodal (ZAQ) parameters for the rod half withdrawn from the node were used, agrement was found to be 0.015% in eigenvalue and 0.03% in the interior fluxes.

Mohamed also showed that, expense could be reduced by generating nodal parameter sets from partial core calculations. The final conclusion was that the discrete ordinate method provides more accurate interpolated values of the nodal parameters than the Monte Carlo technique.

2.6 Models for Time Dependent Solution

In this section we outline the transient models used throughout this study. Our main objective is to point out the differences between the various models, not to describe them in detail.

2.6.1 Time Dependent Corrected Finite Difference Equations

Our starting point will be the time dependent diffusion equation. If fuel is stationary, the time dependent nodal balance equation in the absence of an external source is [H-1]

$$\frac{1}{\upsilon_g}\frac{\partial}{\partial t}\phi_g(\underline{r},t) = -\nabla\cdot J_g(\underline{r},t) - \Sigma_g(\underline{r},t)\phi_g(\underline{r},t) + \sum_{g'=1}^{G}[\chi_g^p(1-\beta)\nu\Sigma_{fg'}(\underline{r},t) + \Sigma_{gg'}(\underline{r},t)]\phi_{g'}(\underline{r},t) + \sum_{d=1}^{D}\chi_g^d\lambda_d c_d(\underline{r},t) \tag{2.30}$$

$$\frac{\partial}{\partial t}c_d(\underline{r},t) = \beta_d\sum_{g'=1}^{G}\nu\Sigma_{fg'}(\underline{r},t)\phi_{g'}(\underline{r},t) - \lambda_d c_d(\underline{r},t) \tag{2.31}$$

Where, in addition to the static equation notation,

$\chi_g{}^p$ = fraction of prompt fission neutrons appearing in group-g,

$\chi_g{}^d$ = fraction of delayed neutrons from family d, appearing in group-g,

$c_d(\underline{r},t)$= density of delayed neutron precursors in family-d,

λ_d = decay constants for delayed neutron precursor family-d,

β_d = fractional yield of delayed neutrons in family-d,

β = total fractional yield of delayed neutrons,

υ_g = neutron speed for group-g,

D = total number of delayed precursors families.

Proceeding as in Section (2.3), Equations (2.1)-(2.16), and adopting a matrix notation permits us to derive from eq. (2.30), corrected time-dependent nodal equations:

$$[\upsilon^{-1}]\frac{d\Phi}{dt} = [M_p]\Phi - [L]\Phi + \sum_{d=1}^{D}\lambda_d c_d \tag{2.32}$$

$$\frac{dc_d}{dt} = [M_d]\Phi - \lambda_d c_d \qquad d=1,\ldots,D \tag{2.33}$$

where

N = total number of nodes,

Φ = The vector NGx1, $\{\bar{\phi}_g\}$,

c_d = the vector NGx1 $\{\chi_d^g \bar{c}_d\}$,

$[\upsilon^{-1}]$ = the matrix NGxNG $\{\upsilon_g^{-1}\}$,

$[M_p]$ = the matrix NGxNG $\{\chi_g^p \nu \Sigma_{fg'}\}$,

$[M_d]$ = the matrix NGxNG $\{\chi_g^d \nu \Sigma_{fg'}\}$,

$[D]$ = a matrix NGxNG consisting of diffusion operator and discontinuity factor ratios,

$[\Sigma_t]$ = the matrix NGxNG $\{\Sigma_{tg}\}$,

$[\Sigma_{gg'}]$ = the matrix NGxNG $\{\Sigma_{gg'}\}$,

$[L] = -[D] + [\Sigma_t] - [\Sigma_{gg'}]$.

2.6.2 Point Kinetics Equations

To derive the point kinetics equations, the flux is partitioned into a shape function *S*, which is a function of space, energy and time, and an amplitude function *T*, which is a function of only time, such that, for the nodal model

$$[\Phi] = [S]\,T(t) \tag{2.34}$$

where the amplitude function (a scalar) and the NG element shape functions are formally defined as

$$T(t) = W^T[\upsilon^{-1}][\Phi]; \qquad [S] = \frac{1}{T(t)}[\Phi]. \tag{2.35}$$

Here W is a vector weight function having the same dimension as the flux, but time independent. In accord with first order perturbation theory, this weight function is chosen as the adjoint flux associated with a static reference calculation. It can be proven that this choice reduces significantly the error due to approximating the shape function.

If we define the matrix representing the total fission neutron production as

$$[M] = (1-\beta)\,[M_p] + \sum_{d=1}^{D} \beta_d [M_d] \tag{2.36}$$

it can be shown that the amplitude function is a solution of the system:

$$\frac{d}{dt}T(t) = \frac{\rho(t)-\beta(t)}{\Lambda(t)}T(t) + \sum_{d=1}^{D} \beta_d C_d(t) \tag{2.37}$$

$$\frac{d}{dt}C_d(t) = \frac{\beta_d(t)}{\Lambda(t)}T(t) - \lambda_d C_d(t) \qquad d=1,\ldots D \tag{2.38}$$

where

$$\rho(t) = \frac{W^T([M(t)]-[L(t)])S(t)}{W^T[M(t)]S(t)}, \tag{2.39}$$

$$\beta_d(t) = \frac{W^T[M_d(t)]S(t)}{W^T[M(t)]S(t)}, \tag{2.40}$$

$$\Lambda(t) = \frac{W^T[\upsilon^{-1}]S(t)}{W^T[M(t)]S(t)}, \tag{2.41}$$

$$C_d(t) = \frac{W^T C_d(t)}{W^T[\upsilon^{-1}]S(t)}. \tag{2.42}$$

The point kinetics equations can also be derived starting from the transport equation [H-4].

It has to be emphasized that equations (2.37) and (2.38) have been derived in a formal fashion without making any approximation. The utility of the point kinetics equations depends on the possibility of computing, by some simple procedure, good approximations to the point kinetics parameters defined by equations (2.39) through (2.42).

Having summarized the time dependent nodal equations and the point kinetics equations we can now discuss various methods for analyzing time-dependent problems. Here we describe only three of them: the point kinetics approximation, adiabatic model and quasi-static space-time model.

2.6.3 Point Kinetics Approximation

In the point kinetics approximation, only the time variation of the flux amplitude is determined. The initial, unperturbed flux, which is the solution of equation:

$$[L(t_0)]\Phi(t_0) = \frac{1}{\lambda}[M(t_0)]\Phi(t_0) \tag{2.43}$$

is usually taken as the shape function. Using the corresponding unperturbed adjoint function, Φ_0^*, as a weight function, reactivity at any instant of time can be calculated from:

$$\rho(t) = \frac{\left(\Phi_0^*\right)^T([M(t)] - [L(t)])\Phi(t_0)}{\left(\Phi_0^*\right)^T[M(t)]\Phi(t_0)} \tag{2.44}$$

Other point kinetics parameters are defined similarly. Because of the simplification that only the initial shape function (or more generally, a constant shape function) is required, the point kinetics equations can be solved using only the instantaneous production and loss operators.

2.6.4 The Adiabatic Model

In the adiabatic approximation, the shape function appearing in the definition of the point kinetics parameters is found from fundamental solutions of the static equation. Thus equations (2.32) and (2.33) can be combined by introducing an eigenvalue, λ, appropriate to the conditions in the reactor at time, t, and neglecting the time derivatives of the flux and delayed precursor concentrations:

$$[L(t)]\Phi^{(\lambda)}(t) = \frac{1}{\lambda}[M(t)]\Phi^{(\lambda)}(t). \tag{2.45}$$

If $\Phi^{(\lambda)}(t)$ is used as a shape function, reactivity becomes:

$$\rho(t) = \frac{\left(\Phi_0^*\right)^T([M(t)] - [L(t)])\Phi^{(\lambda)}(t)}{\left(\Phi_0^*\right)^T[M(t)]\Phi^{(\lambda)}(t)}. \tag{2.46}$$

The use of equation (2.45) yields a simple expression for the reactivity:

$$\rho(t) = \frac{\left(\Phi_0^*\right)^T\left([M(t)] - \frac{1}{\lambda}[M(t)]\right)\Phi^{(\lambda)}(t)}{\left(\Phi_0^*\right)^T[M(t)]\Phi^{(\lambda)}(t)} = 1 - \frac{1}{\lambda}. \tag{2.47}$$

Since some of the time dependent changes in the system are reflected in $\Phi^{(\lambda)}(t)$, the adiabatic approximation is expected to give much better results than the point kinetics approximation. However, it should also be emphasized that the adiabatic model doesn't distinguish the shape of the delayed neutron source from the prompt neutron source. In other words, in the adiabatic model, all neutrons are treated as prompt neutrons. Therefore if there is a significant difference between those two source shapes, the model can fail to predict reactor behavior accurately. This flux shape difference is particularly important when the response of the reactor is sensed with localized neutron detectors. Even if the perturbations don't change the shape function significantly, small changes in the shape may be as significant in determining the detector response as small perturbations in the amplitude function [B-3].

For time-dependent solutions, reactivity tables as a function of transient variables, such as control rod position, are calculated from a series of static calculations, and the transient is run by using these precalculated rod calibration curves. If feedback effects are neglected, the shape and amplitude equations become completely independent, and time-dependent shape functions can be precalculated [O-2].

In this study, for the ANS studies, the adiabatic model with precalculated shape functions was used for transient analysis. For various transients, time-dependent shape functions and reactivity curves were precalculated using the static mode of the nodal code ZAQ, and throughout the transient, their values were found by interpolation assuming both values change linearly between any two state points. For some cases, to measure the sensitivity to changes in the shape function, the initial flux shape was used throughout the transient.

2.6.5 The Space-Time Model

The space-time model which will be described here is an extension of the improved quasi-static method used in the nodal code ZAQ [B-2]. This method solves Equations (2.32) and (2.33), replacing the derivatives in the flux equation by a first order backward difference approximation. Delayed precursors can either be directly integrated, or a similar backward difference scheme can be applied to eliminate the time derivatives. Defining the time steps $\Delta t_n = t_n - t_{n-1}$ over the discretized time domain, and application of a "theta method" to the right hand side results in the following algebraic equations:

$$[\upsilon^{-1}]\frac{\Phi^n-\Phi^{n-1}}{\Delta t_n} = \theta\{[M_p]^n\Phi^n+[L]^n\Phi^n+\sum_d \lambda_d c_d^n\} + (1-\theta)\{[M_p]^{n-1}\Phi^{n-1}+[L]^{n-1}\Phi^{n-1}+\sum_d \lambda_d c_d^{n-1}\} \tag{2.48}$$

$$\frac{c_d^n-c_d^{n-1}}{\Delta t_n} = \theta\{[M_p]\Phi^n-\lambda_d c_d^n\}+(1-\theta)\{[M_p]\Phi^{n-1}-\lambda_d c_d^{n-1}\} \tag{2.49}$$

Because of stability considerations, theta is usually chosen to be either 1 or 1/2.

In the improved quasi-static model, since the shape of the flux is slowly varying, this first order-difference form is applied over larger time intervals. The error in the more rapidly varying amplitude function can be compensated, at the end of each time step, by recalculating the amplitude function using the point kinetics equations over the same interval but with a set of much smaller time increments. The required point-kinetics parameters for the recalculation are determined by the shape function at the end of time step. For example, if the unperturbed adjoint is chosen as the weight function, reactivity is found from the equation

$$\rho(t) = \frac{\left(\Phi_0^*\right)^T([M(t)]-[L(t)])\Phi(t)}{\left(\Phi_0^*\right)^T[M(t)]\Phi(t)}. \tag{2.50}$$

where $\Phi(t)$ is assumed to vary linearly between its value at the beginning and at the end of the large time step.

At the end of each large time step, nodal flux amplitudes and precursor concentrations are corrected using the point kinetics results. For the next time interval, flux amplitudes and precursor concentrations are extrapolated.

The time and space dependent cross sections and discontinuity factor ratios in the time-dependent nodal and point kinetic equations are found from a higher order reference solution as has already been discussed in previous sections. The various interpolation schemes permit finding them at any instant of time during the transient solution.

2.7 Summary

In this chapter, we reviewed the nodal diffusion theory model taking into account transport corrections. The components of that model were presented: First the steady-state finite difference nodal equations were derived; then the use of the Monte Carlo and discrete ordinate procedures to obtain the nodal parameters appearing in the nodal equations was discussed. In the last section we outlined the various transient models.

The remaining question is "*how accurate is the model for analyzing transients of interest for tightly coupled reactors?*". In Chapter 3, we shall develop a procedure which can be used to validate transient models. Chapter 4 presents the application of that procedure for various transients associated with the ANS. For almost all cases, thermal-hydraulic feedback changes the development of transients significantly. In Chapter 5, we shall introduce a simple thermal-hydraulic feedback model for the Advance Neutron Source Reactor and reevaluate the transients in the presence of feedback comparing the various time dependent models.

Chapter 3

A Validation Model

3.1 Introduction

This chapter is devoted to the development of a procedure to validate the few-group diffusion theory nodal model based on cross sections and discontinuity factors found from higher order reference solutions. First, pseudo-static equations will be derived starting from time-dependent diffusion and time-dependent transport equations. Then calculational steps will be presented. Finally, studies concerned with extrapolation schemes will be discussed in detail.

3.2 The Pseudo-Static Eigenvalue Test

In the previous chapter we summarized a few-group, transient nodal method based on few-group cross sections and corrected by discontinuity factors found from static, multigroup transport calculations. In the absence of a transient multigroup transport code, a direct theoretical determination of the accuracy of the transient few-group nodal method is not possible. Accordingly, an indirect test has been developed based on the fact that at any stage during a transient calculation, the transient equations can be converted to a static eigenvalue problem by introducing instantaneous pointwise group-flux and delayed precursor frequencies. These time constants can be edited at any time step from the transient analyzed. A test of whether the nodal transient calculation would agree with a transient transport calculation is then to see if the dynamic frequencies inserted into the time-dependent equation (thereby converting it to static equation) will yield an eigenvalue of unity.

In the following subsections we derive the pseudo-static diffusion and transport equations from their time-dependent forms and then describe how to edit and infer the dynamic frequencies from the time-dependent solution.

3.2.1 Pseudo-Static Diffusion Equations

At any stage during a transient calculation, by replacing the time derivatives of group-flux and delayed precursor concentrations with "frequencies" multiplied into the quantities themselves, the transient equations can be converted to pseudo-static equations. Thus we write:

$$\frac{\partial}{\partial t}\phi_g(\underline{r},t) = \omega_g(\underline{r},t)\phi_g(\underline{r},t) \tag{3.1}$$

$$\frac{\partial}{\partial t}c_d(\underline{r},t) = \omega_d(\underline{r},t)c_d(\underline{r},t). \tag{3.2}$$

Use of equations (3.1) and (3.2) in the transient model converts it to a pseudo-static model at the instant *t*. In the case of the transient, multigroup diffusion equations for the flux and the delayed precursor concentrations, equations (2.30) and (2.31) become,

$$\begin{aligned} &\frac{\omega_g(\underline{r},t)}{\upsilon_g}\phi_g(\underline{r},t) - \nabla\cdot D_g(\underline{r},t)\nabla D_g(\underline{r},t) + \Sigma_g(\underline{r},t)\phi_g(\underline{r},t) \\ &= \sum_{g'=1}^{G}\frac{1}{\lambda_{ps}}[\chi_g^p(1-\beta)\nu\Sigma_{fg'}(\underline{r},t) + \Sigma_{gg'}(\underline{r},t)]\phi_{g'}(\underline{r},t) + \sum_{d=1}^{D}\chi_g^d\lambda_d c_d(\underline{r},t) \end{aligned} \tag{3.3}$$

$$\omega_d(\underline{r},t)c_d(\underline{r},t) = \beta_d\sum_{g'=1}^{G}\nu\Sigma_{fg'}(\underline{r},t)\phi_{g'}(\underline{r},t) - \lambda_d c_d(\underline{r},t). \tag{3.4}$$

Equation (3.4) can be solved for c_d and the result substituted in equation (3.3) to give pseudo-static equation at time *t*:

$$\begin{aligned} &-\nabla\cdot D_g(\underline{r},t)\nabla\phi_g(\underline{r},t) + \left[\Sigma_{tg}(\underline{r},t) + \frac{\omega_g(\underline{r},t)}{\upsilon_g}\right]\phi_g(\underline{r},t) - \sum_{g'=1}^{G}\Sigma_{gg'}(\underline{r},t)\phi_{g'}(\underline{r},t) \\ &= \sum_{g'=1}^{G}\frac{1}{\lambda_{ps}}\left[\chi_g^p(1-\beta) + \sum_{d=1}^{D}\frac{\chi_g^d\beta_d\lambda_d}{\lambda_d+\omega_d(\underline{r},t)}\right]\nu\Sigma_{fg'}(\underline{r},t)\phi_{g'}(\underline{r},t) \end{aligned} \tag{3.5}$$

where λ_{ps}, the pseudo-static eigenvalue, is introduced for later mathematical convenience. It can be seen that equation (3.5) has the same form as the steady state diffusion equation except that the total cross section and fission spectrum terms are modified by instantaneous omega values.

Before deriving the transport form of the pseudo-static equations, some background information about the flux and delayed precursor omegas will be given to understand the nature of the problem.

3.2.2 Asymptotic Omega Modes

For transient analysis, ω-modes, or so called period eigenfunctions are often used to provide approximate solutions or to prove certain characteristics of the system. The simplest form of omega modes can be derived by assuming that, with a constant value of reactivity, delayed neutrons appear instantaneously, and the reactor without any external source is on an asymptotic period. Thus the neutron density behaves in time as $\phi e^{\omega t}$ [H-1]. Notice that, the omega, here, has neither space nor energy dependency. With that assumption the time-dependent diffusion equation becomes the eigenvalue equation

$$\upsilon (M-L)\phi_n^{(\omega)} = \omega_n \phi_n^{(\omega)} \tag{3.6}$$

where, for a reactor of finite size there will be a least negative, real eigenvalue and a corresponding all-positive eigenfunctions such that the neutron flux will behave as $\phi_0^{(\omega)} e^{\omega_0 t}$. For a critical case, solution of eq. (3.6) yields the eigenvalue $\omega_0 = 0$.

If delayed neutrons are not assumed to appear instantaneously (again for the constant values of reactivity and when the source term is negligible in comparison with the fission rate), they will also eventually behave as $C_i e^{\omega t}$. For this case the eigenvalue ω_0 is the most positive root of the inhour equation [H-4]

$$\rho = \omega\Lambda + \sum_i \frac{\beta_i \omega}{\omega + \lambda_i}. \tag{3.7}$$

Under these circumstances the stationary shape function $\phi_0(r, E)$ is one of the solutions of Equation (3.5) where the space and energy dependent frequencies are replaced by the asymptotic value ω_0. Constant values of ω found from that simplified pseudo-static equation are the same as the roots of Equation (3.7).

Generally the omega modes divide into two classes [B-3]: (i) delayed modes characterized by small values of ω and (ii) rapidly decaying modes (prompt modes) characterized by large values of omega. Except for the prompt critical situation, the most positive (least negative) value of ω is such that $|\omega/\upsilon_g| \ll \Sigma_{tg}$, and the corresponding stationary solution is one associated with a delayed neutron yield term differing from the equilibrium value. These ω-values, related to delayed neutrons, form clusters such that for every λ_i there corresponds a group of ω_i's which are slightly smaller in magnitude than λ_i [G-1].

For rapidly varying modes corresponding to very large values of $|\omega|$, the stationary solution is one corresponding to a change in the absorption cross section by an amount ω/υ_g and the complete absence of any delayed neutrons.

Even for these asymptotic cases, the solution of Equation (3.5) for the eigenvalue ω is not mathematically straight forward.

3.2.3 Instantaneous Omega Modes

The flux and delayed precursor omegas appearing in Equation (3.5) differ from the asymptotic omega values. They are not eigenvalues, but, rather are functions of space, energy and time. Although they can not be found by solving Equation (3.5), values of the instantaneous ω_d's and ω_g's can be edited from a space-time problem at the time in question. Then if those values of group parameters are substituted into Equation (3.5), the resultant "pseudo-static" eigenvalue, λ_{ps}, should have unity value. (Here it is assumed that before starting the time dependent solution, the fission source is divided by the static eigenvalue, λ, if that value differs from unity.) The pseudo-static eigenvalue is determined by the omega values. It seems reasonable to expect that only a correct prediction of the space-time behavior of the flux and delayed precursor concentrations can yield an eigenvalue of unity. Therefore deviation from unity can be used to measure the accuracy of the space-time model in question. Moreover, for a given set of ω values, there is a particular solution of pseudo-static flux ϕ corresponding to the largest value of λ_{ps} and that pseudo-static flux shape should match the transient flux shape at time, *t*. This pseudo-static flux shape test is important especially for measuring the accuracy of time dependent models in which approximate shape functions are used in calculations, such as the point kinetics and adiabatic models.

As was mentioned before, the accurate transient analysis of the tightly coupled reactors requires a multigroup, transport solution. Hence, the accuracy and the validity of the few group diffusion theory model has to be tested against that solution. Thus the pseudo-static eigenvalue and flux shape test must be extended to the discrete-ordinate transport model. In the next section the pseudo-static transport equation will be derived.

3.2.4 The Pseudo-Static Transport Equation

The time dependent neutron transport equation is [H-4]

$$\frac{1}{\upsilon_g}\frac{\partial}{\partial t}\Psi_g(\underline{r},\underline{\Omega},t) = -\underline{\Omega}\cdot\nabla\Psi_g(\underline{r},\underline{\Omega},t) - \Sigma_{tg}(\underline{r},t)\Psi_g(\underline{r},\underline{\Omega},t)$$
$$+\int d\Omega'\sum_{g'}\left[\chi_g^p(1-\beta)\nu\Sigma_{fg'}(\underline{r},t) + \Sigma_{gg'}(\underline{r},\underline{\Omega}'\rightarrow\underline{\Omega},t)\right]\Psi_g(\underline{r},\underline{\Omega}',t) + \sum_d \chi_g^d\lambda_d c_d(\underline{r},t) \tag{3.8}$$

$$\frac{\partial}{\partial t}c_d(\underline{r},t) = \int d\underline{\Omega}'\sum_{g'}\nu\Sigma_{fg'}(\underline{r},t)\Psi_g(\underline{r},\underline{\Omega}',t) - \lambda_d c_d(\underline{r},t) \tag{3.9}$$

Delayed precursor and directional flux "frequencies" can be defined as,

$$\omega_g(\underline{r},\underline{\Omega},t) = \frac{1}{\Psi_g(\underline{r},\underline{\Omega},t)}\frac{\partial}{\partial t}\Psi_g(\underline{r},\underline{\Omega},t) \tag{3.10}$$

$$\omega_d(\underline{r},t) = \frac{1}{c_d(\underline{r},t)}\frac{\partial}{\partial t}c_d(\underline{r},t). \tag{3.11}$$

Notice that, although the transport theory expression for the delayed neutron precursor frequency is same as its diffusion theory counterpart, there is an additional directional dependency for the flux frequency. Equations (3.10) and (3.11) can be used to eliminate the time derivatives in equations (3.8) and (3.9), and then the pseudo-static transport equation is obtained as:

$$\Omega\cdot\nabla\Psi_g(\underline{r},\underline{\Omega},t)+\left[\Sigma_{tg}(\underline{r},t)+\frac{\omega_g(\underline{r},\underline{\Omega},t)}{\upsilon_g}\right]\Psi_g(\underline{r},\underline{\Omega},t)$$
$$-\int d\underline{\Omega}'\sum_{g'}\Sigma_{gg'}(r,\underline{\Omega}'\rightarrow\underline{\Omega},t)\Psi_{g'}(r,\underline{\Omega}',t)$$
$$=\int d\underline{\Omega}'\frac{1}{\lambda_{ps}}\sum_{g'}\left[\chi_g^p(1-\beta)+\sum_d\frac{\chi_g^d\beta_i\lambda_d}{\lambda_d+\omega_d(\underline{r},t)}\right]\nu\Sigma_{fg'}(\underline{r},t)\Psi_g(\underline{r},\underline{\Omega}',t) \tag{3.12}$$

For the discrete ordinate method a similar pseudo-static form can be obtained by replacing the definition of the directional flux frequency in equation (3.10) with

$$\omega_g(\underline{r},\Omega_d,t)=\frac{1}{\Psi_g(\underline{r},\Omega_d,t)}\frac{\partial}{\partial t}\Psi_g(\underline{r},\Omega_d,t)\quad d=1,..,D. \tag{3.13}$$

Provided that the flux and delayed precursor frequencies are known, the pseudo-static transport equation, either in the form of equation (3.12) or the form that can be obtained starting from the discrete ordinate equations, can be solved for the pseudo-critical eigenvalue, λ_{ps}, and the pseudo-critical flux shapes using a static transport code.

By inferring the omega values required for the pseudo-static transport equations from the time-dependent transient model in the question, the pseudo-static eigenvalue test described in the previous section can be extended and used to measure the accuracy of the few-group nodal transient solution.

3.3 Calculation Steps

Figure 2.1 shows the calculational path for the validation of the few-group nodal transient model. The overall scheme is as follows:

1. Find few-group cross sections and discontinuity factors for various reactor conditions anticipated during the transient of interest by editing multigroup transport solutions as described in section 2.5.3.

2. Form interpolation tables for those few-group nodal parameters.

3. Analyze the transient of interest using the transient version of the few-group nodal code.

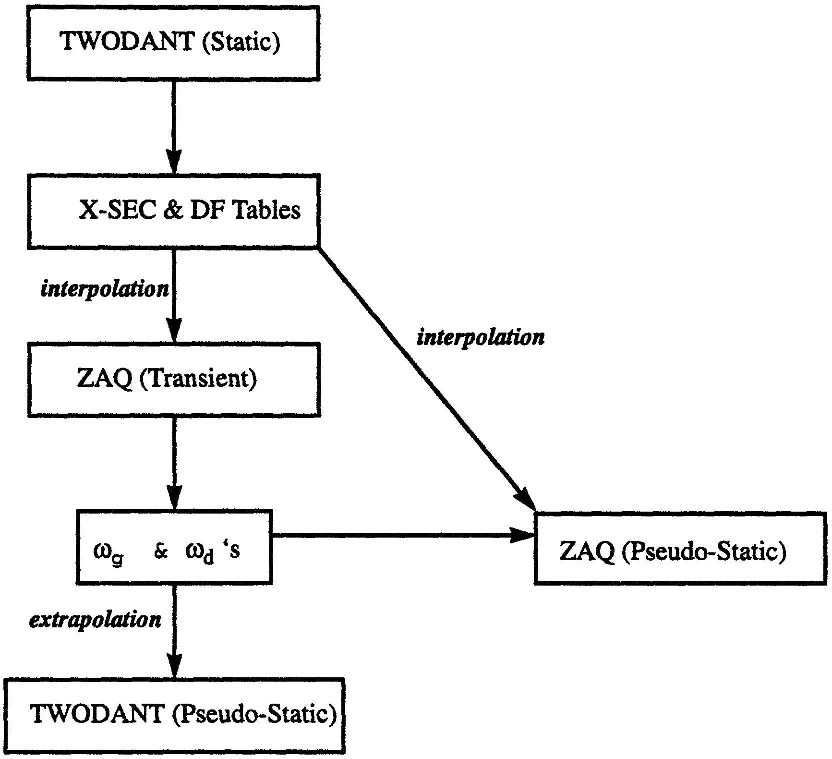

Figure 3.1: Calculational steps for the pseudo-static test

4. At particular times during the transient edit ω_d's and few group ω_g's for the nodes comprising the reactor.

5. Run the pseudo-static problem by using the nodal code itself and check the pseudo-static eigenvalue and compare the pseudo-static fluxes with the transient fluxes. This step although it is not sufficient to validate the few-group nodal transient solution, can be used for sensitivity studies and to distinguish the accuracy of the point-kinetics and other approximate methods.

6. By some extrapolation scheme, infer ω's to be used for the pseudo-static, multigroup transport problem.

7. Run that problem and see if its eigenvalue is 1 and if few-group nodal fluxes edited from the results match the transient nodal fluxes at the time in question.

If this procedure is to provide a meaningful numerical test of the accuracy of a few-group nodal model based on cross sections and discontinuity factor ratios found from static multigroup transport solutions, a number of questions have to be addressed.

The major question is how to infer the multigroup transport omegas from the few-group transient results. There are also questions of convergence, accuracy vs. roundoff error and sensitivity. One other issue is to find interpolation schemes that minimize interpolation errors for the nodal parameters required by the transient model.

In the following sections these issues will be addressed, and the major components of the validation model will be discussed in detail.

3.3.1 Interpolation Procedures

In the validation procedure in order to distinguish between accurate and erroneous results, it is important to perform the pseudo-static eigenvalue problem as accurately as possible. In this connection errors arising from the interpolation procedures used to determine homogenized, two-group cross sections and discontinuity factor ratios for the *r-z* nodal code ZAQ from eight-group, static, transport (TWODANT) results should be kept minimum. For this investigation, tests were conducted to examine the behavior of nodal parameters as the transient progresses. Two transients were analyzed for the three-element ANS core (core description given in Appendix B): control rod withdrawal and light water ingress.

Control Rod Withdrawal

To analyze the behavior of nodal parameters throughout the transient, seven TWODANT criticality problems corresponded to the tips of one of the central control rods located at different positions in the node were run. Homogenized two-group cross sections and discontinuity factor ratios for the node in question were edited from the TWODANT results. Figure 3.2 shows the total cross section and discontinuity factor ratios for a node through which the control rod is moving. Results from various interpolation schemes which use reference values only for the rodded, half rodded, and unrodded or only for the rodded and unrodded cases are compared with reference results corresponding to the other intermediate rod positions.

The best match for total cross section (and all other cross sections) comes from an average (suggested by Mohamed [M-1]) of a linear shape and a shape found from a prescription due to Gehin [G-2]. Thus, if t is the fraction of the rod removed from the node, with superscripts r and u indexing the rodded and unrodded portion of the node, the interpolation formula for the

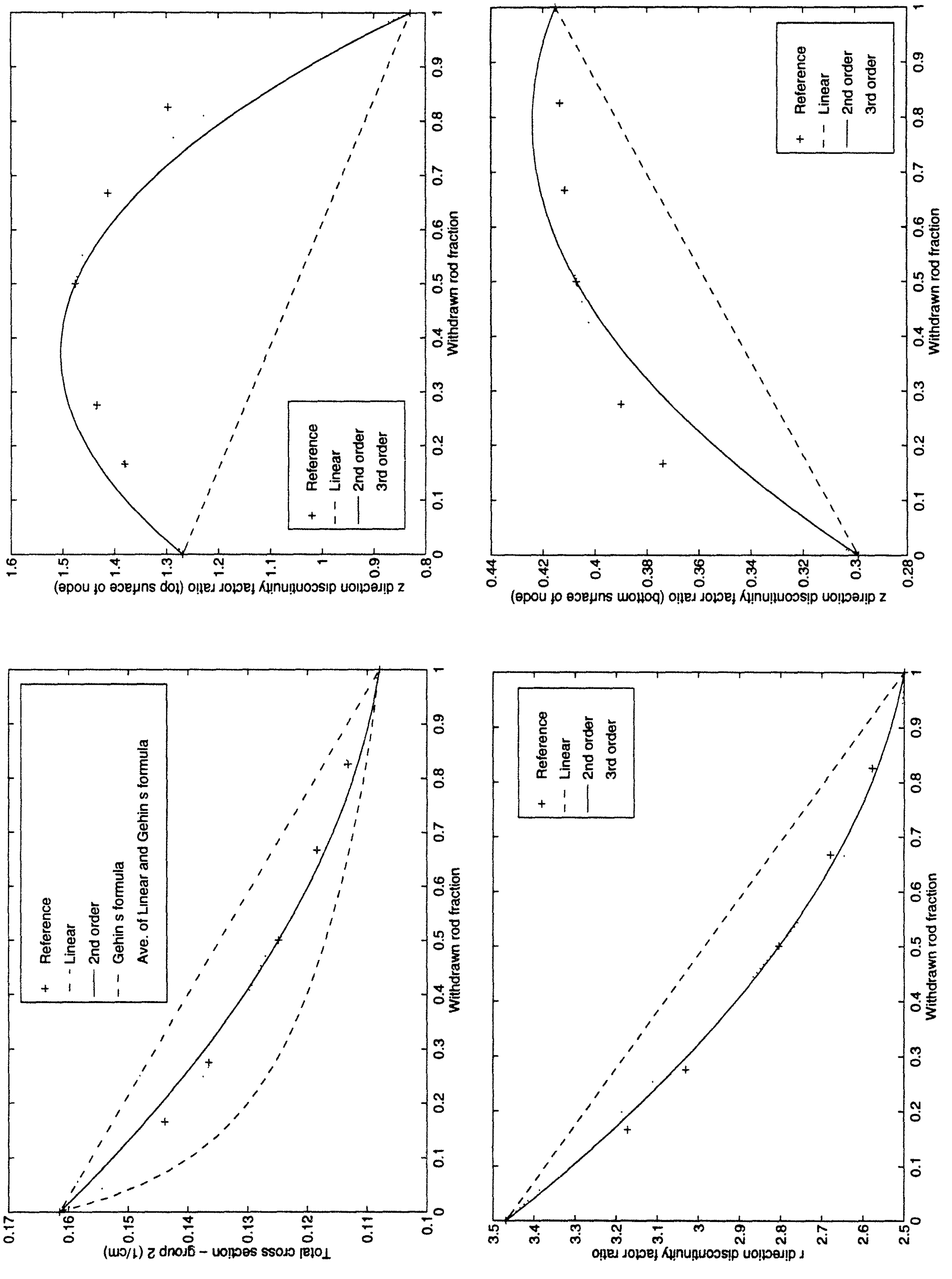

Figure 3.2: Interpolation curves for the thermal group cross sections and discontinuity factor ratios vs. fraction of rod withdrawn from a node

corrected cross section is given by

$$\Sigma_{\alpha}\Big|_{t} = \frac{[(2-t)\phi^{r}+t\phi^{u}](1-t)\Sigma^{r}_{\alpha}+[(1+t)\phi^{u}+(1-t)\phi^{r}]t\Sigma^{u}_{\alpha}}{2[t\phi^{u}+(1-t)\phi^{r}]} \tag{3.14}$$

where the unrodded and rodded fluxes are approximated as the average of the flux in the partially rodded node and its lower neighbor or upper neighbor respectively.

Examination of the radial discontinuity factor ratio behavior indicates that a second order polynomial fit is quite accurate. For the axial discontinuity factor ratios a much more accurate fit comes from a third order polynomial shape which uses three reference conditions, rodded, half rodded and unrodded and the assumption of an extremum at $t_e=0.4$ for the factor at the top surface of a node and $t_e=0.6$ for the factor at the bottom surface of a node [G-3].

Although changes in cross-sections and discontinuity factor ratios are greatest for a node through which control rod is moving, that motion also affects those parameters in other nodes throughout the reactor because of the tightly coupled characteristics of the reactor being analyzed. Accordingly the following interpolation procedures were used to infer two-group, nodal parameters from the static eight-group transport calculations:

For a node through which the rod tip is moving:

- cross sections interpolated using an average of a linear shape and shape from flux weighted Gehin's formula,
- axial discontinuity factor ratios found using a third order interpolation procedure,
- radial discontinuity factor ratios found using a second order interpolation procedure,

For all other nodes:

- cross sections and discontinuity factor ratios found using a second order interpolation procedure.

The Light Water Ingress Event

The light water ingress event is considered as an accident resulting in a mixture of light and heavy water entering the reactor. (A complete description of the event will be given in Chapter 4.) The mathematical modelling is the same as for the withdrawal of a control rod. As was done for the rod ejection transient, sets of cross sections and discontinuity factor ratios for a node were edited from multigroup TWODANT results for various heavy water-light water mixture front locations in a node. The mixture was assumed to be 95% D_2O and 5% H_2O. Figures 3.3 shows the behavior of some of the nodal parameters for a fueled node thorough which the heavy water-light water mixture is rising. As can be seen from these figures, except for the axial discontinuity factor ratio, all the nodal parameters change linearly. For the axial discontinuity factor ratios a second order interpolation scheme is much more accurate. It was also found that for all other nodes a linear interpolation scheme is sufficiently accurate for both cross sections and discontinuity factors.

3.3.2 Omega Edits

A transient of interest can be run using the interpolation schemes discussed above to find the nodal parameters required for the various transient models. The instantaneous flux and delayed precursor frequencies at time step *n* are then calculated from the following expressions:

$$\omega_g(\underline{r},t_n) = \frac{1}{\Delta t_n} ln\left(\frac{\phi_g(\underline{r},t_n)}{\phi_g(\underline{r},t_{n-1})}\right) \tag{3.15}$$

$$\omega_d(\underline{r},t_n) = \frac{1}{\Delta t_n} ln\left(\frac{c_d(\underline{r},t_n)}{c_d(\underline{r},t_{n-1})}\right) \tag{3.16}$$

Where ϕ_g and c_d's are the space time dependent flux and delayed precursor concentrations.

As will be recalled from the previous chapter, the point-kinetics model uses constant flux shape throughout the whole transient. For this model the ω_g and ω_d's vary in time, but are the same for all nodes at a given time, and the group-one and group-two ω_g's are equal at all times.

For the adiabatic model, with the amplitude function *T(t)* during the transient computed by the point kinetics equations and detailed flux shapes during the transient found by interpolation of the static λ-mode shapes, the space-time behavior of the group-fluxes during the transient can be reconstructed. The flux omegas can then be edited from these reconstructed group-fluxes.

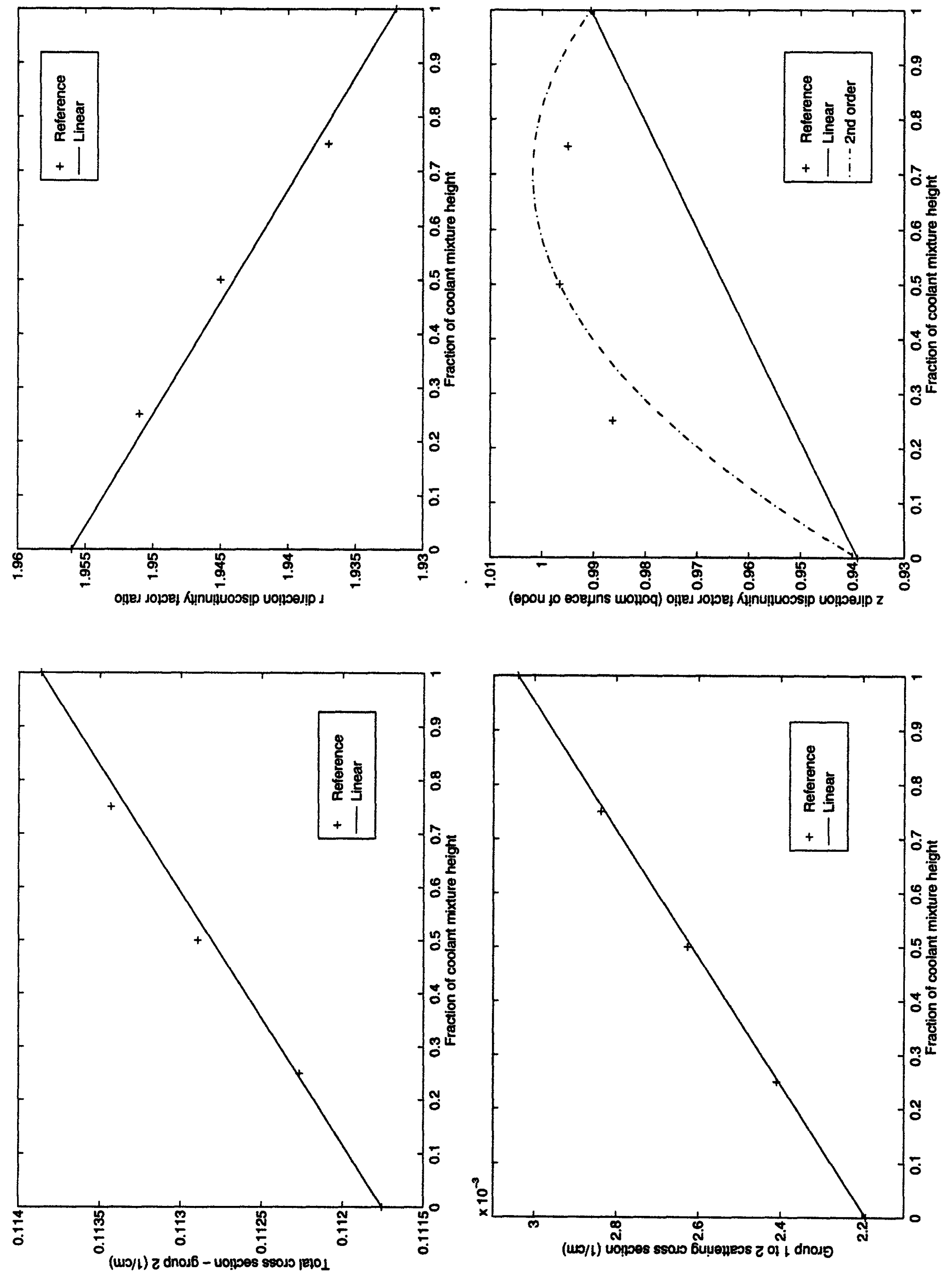

Figure 3.3: Interpolation curves for the thermal group cross sections and discontinuity factor ratios vs. fraction of the heavy water-light water mixture height in a node.

3.3.3 Extrapolation Procedures: Energy group expansion

To carry out the validation procedure described in the previous sections, it is necessary to infer values of the ω's for the multigroup discrete ordinate equations from the few-group nodal transient results. This may be difficult to do, especially if the pseudo-critical value of λ_{ps} for the discrete ordinate equations is sensitive to the inferred ω values.

We first discuss the extrapolation of the flux and precursor omegas from few-group to multigroup structure, leaving examination of angular dependency of the flux omegas for the next section.

Tests were conducted for two different types of transients, control rod ejection and light water ingress. For the control rod ejection two cases were examined, the first for the rod withdrawn in 10 seconds, and the second for the rod withdrawn in 0.1 seconds. Since the nature of the transients differ, in the subsequent sections extrapolation procedures and sensitivity studies will be presented for each transient separately.

Figure 3.4 shows the simplified *r-z* geometry model of the three-element ANS design used throughout our studies. Figure 3.5 shows the initial steady-state flux shapes for the fast and thermal groups. The origin *(1,1)* is at the lower central node of the reactor, and the plots are for 19 mesh spacings in the radial direction and 48 mesh spacings in the axial direction. The logarithmic plot makes it possible to see flux shape behavior outside the core region.

Control Rod Withdrawal Transients

The transients analyzed were the complete withdrawal of one of the central control rods from its initial position with the tip at the plane between the upper and the lower reactor halves in 10 seconds and in 0.1 seconds.

As a first step in investigating the extrapolation procedures, the nature of the ω's inferred when the transient is analyzed by the two-group nodal method was examined. Values computed using the nodal code ZAQ for the thermal flux omegas, ω_2, and the ratio of thermal to fast flux omega ($= \omega_2/\omega_1$) at various times during the 10 second withdrawal are shown in Figure 3.6. The positive blips along the central axis show the sudden increase in ω_2 in the node from which the rod is being withdrawn. The corresponding fast group blips are smaller since decreased fast capture is compensated by increased slowing down. The effects are small

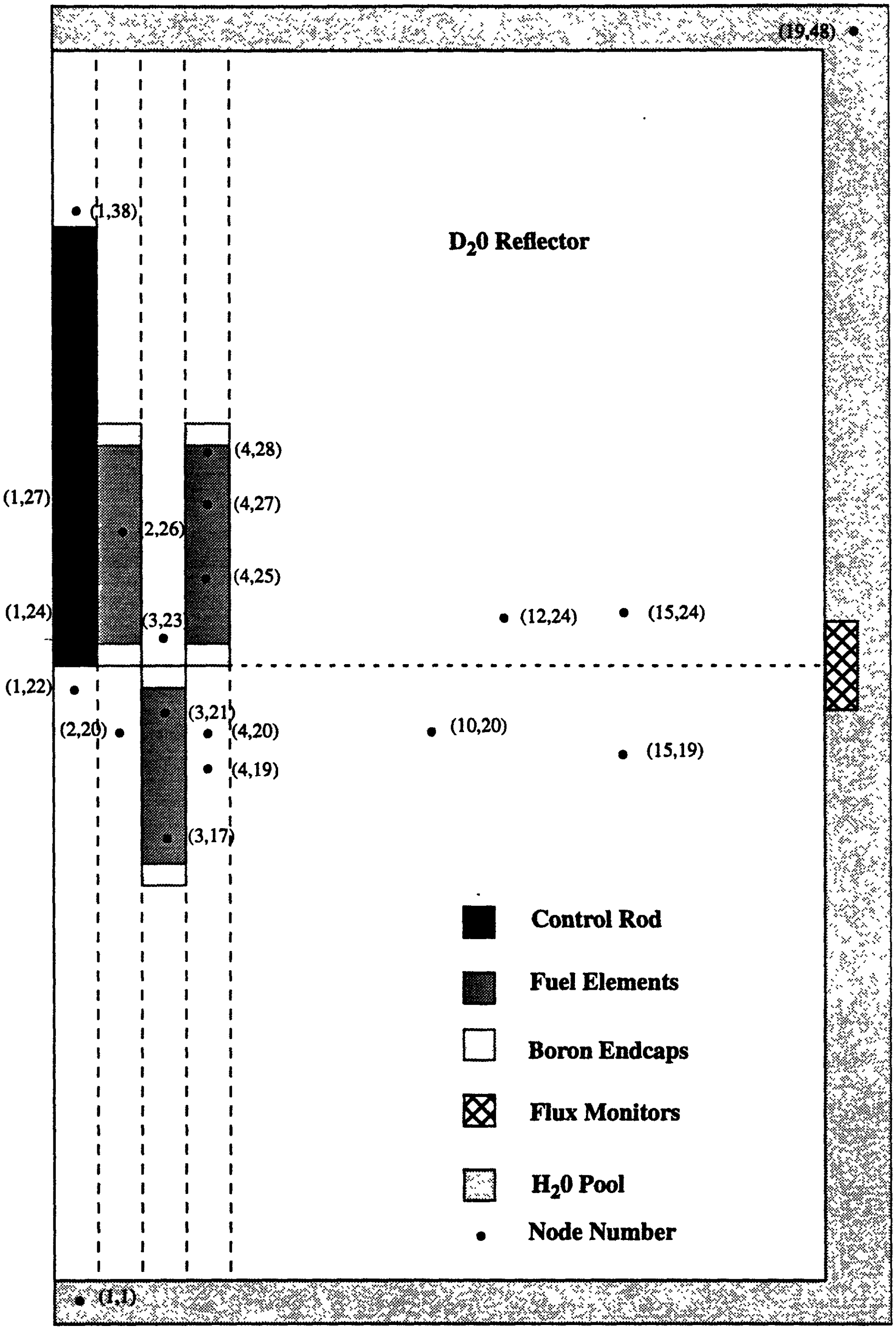

Figure 3.4: R-Z Model of the three-element ANS core

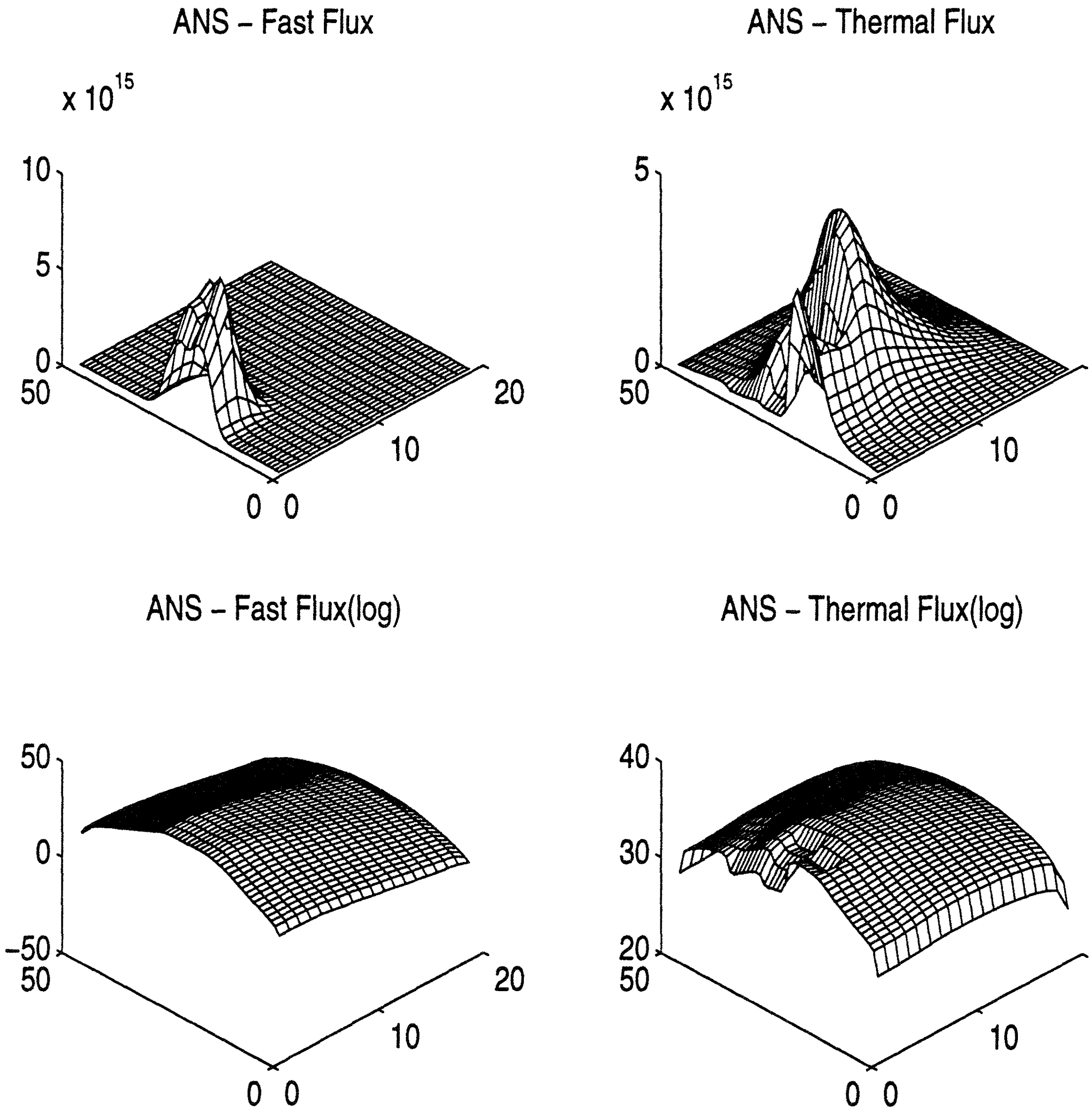

ANS - Fast Flux

ANS - Thermal Flux

ANS - Fast Flux(log)

ANS - Thermal Flux(log)

Figure 3.5: Steady-state flux plots

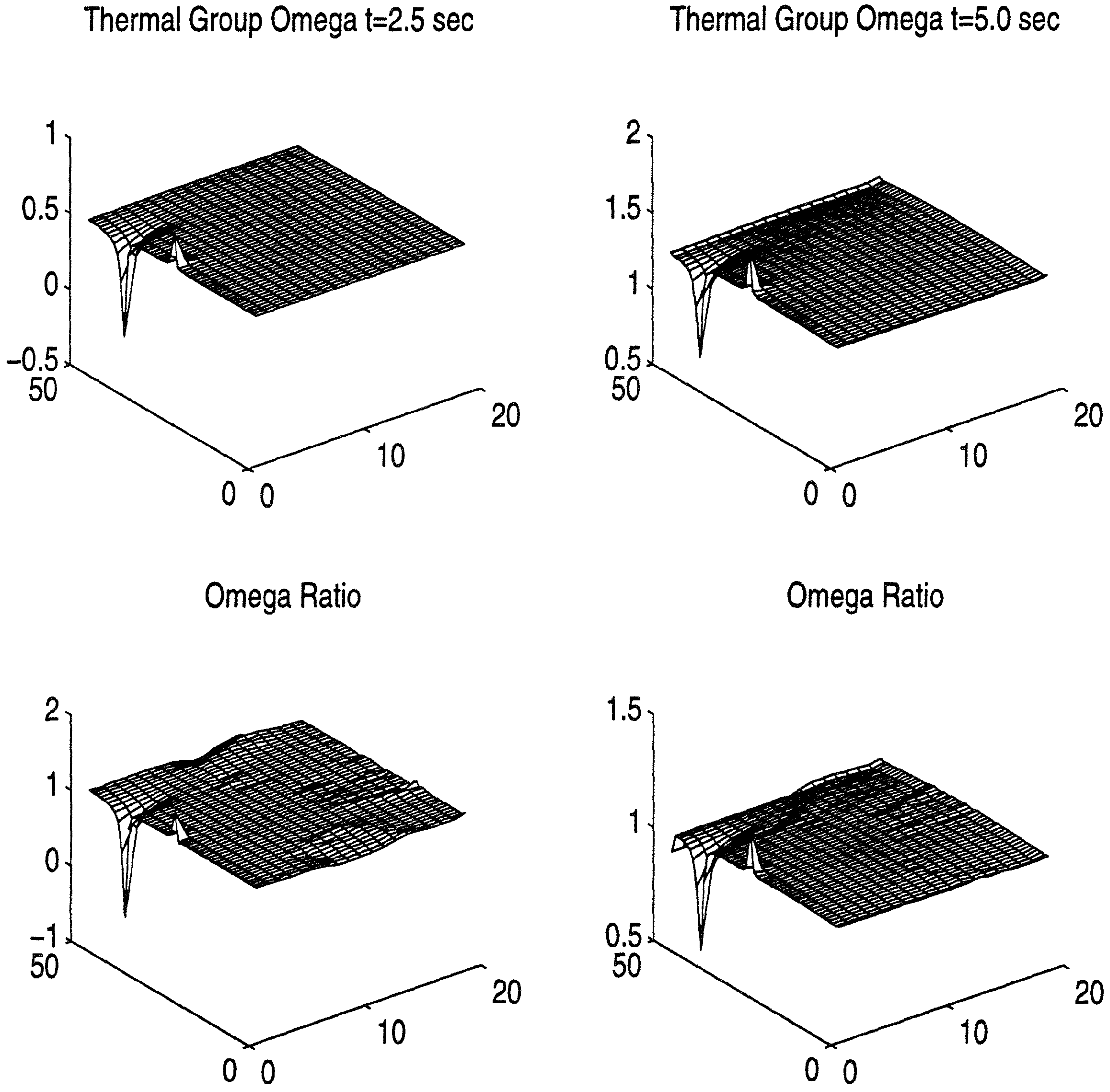

Thermal Group Omega t=2.5 sec

Thermal Group Omega t=5.0 sec

Omega Ratio

Omega Ratio

Figure 3.6: Flux omegas for the 10 second rod withdrawal transient

since the rod being removed is one of three and thus shielded by the two rods that do not move. The much larger dip in thermal flux and very large dip in the thermal-to-fast ω-ratio is conceivably due to the insertion of the upper end of the control rod in the D_2O region. There the other two fixed rods are not present to shield the effect.

Figure 3.7 is analogous to the Figure 3.6 except that the rod is withdrawn in 0.1 seconds. At t=0.05 seconds, the omega behavior is very similar to the slow rod removal except that the magnitude of omegas are much larger. At t=0.2 seconds this part of the transient behavior has smoothed out. (Recall that the control rod was fully withdrawn at 0.1 seconds.) The fact that the ω_2's are not the same throughout the reactor illustrates the lag in flux shape due to the relatively slow rate at which delayed neutron precursor concentrations change.

As can be seen from plots of the thermal-to-fast ratios of the instantaneous periods for both transients, except for the nodes through which the control rod is moving, the ratios are close to unity. This observation encouraged us to hope that an accurate procedure for inferring multigroup ω's from few-group values could be found.

Since there is no transient, multigroup, discrete ordinate code, the question of inferring multigroup discrete ordinate ω_g's and ω_d's from few-group transient nodal results was explored by comparing the ω's generated by a two-group nodal model with those generated by an eight-group nodal model, both simulations being run using the transient nodal code ZAQ.

For both the two- and eight-group simulations, group cross sections and discontinuity factors were interpolated (vs. control rod position) from values found from static eight-group discrete ordinate (TWODANT) calculations. Thus, the initial nodal (ZAQ) eight- and two-group eigenvalue and the initial two-group ZAQ flux shapes match exactly those reduced from the eight-group TWODANT calculations.

The two- and eight-group flux omegas were edited from the nodal transient solutions at various times during the transient. Figure 3.8 shows eight-group ω-values (solid lines) and two-group ω-values (dotted lines) for various nodes at time t=0.02 seconds for the rod withdrawn in 0.1 seconds. The locations of the nodes are indicated on Figure 3.4.

The curves make qualitative sense. In node *(1,24)*, from which, the control is moving, the low energy fluxes are rising faster than the high energy fluxes. The opposite is true for node *(1,38)* into which the control is moving. For fueled nodes all ω_g's - both eight-group and two-

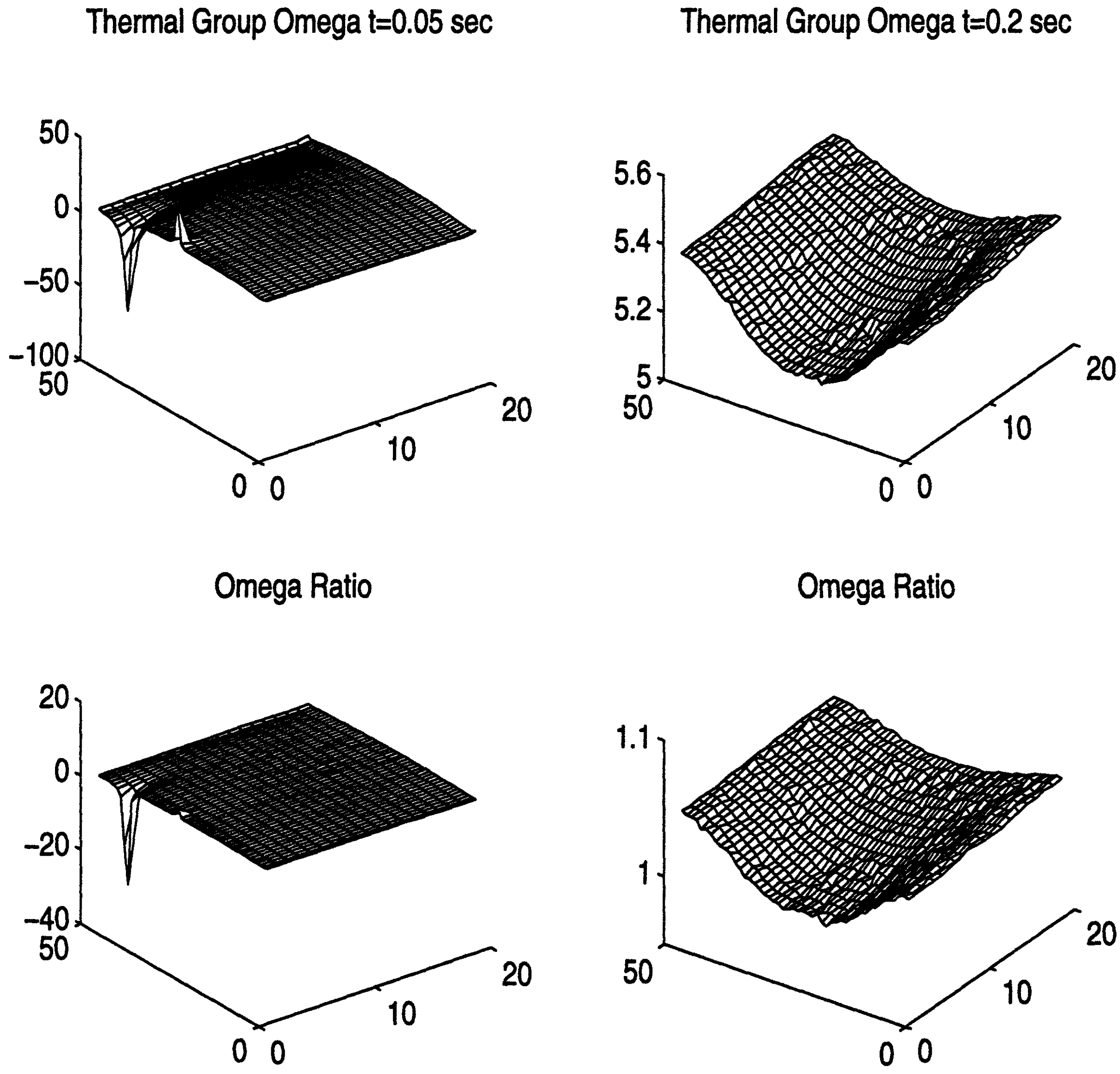

Thermal Group Omega t=0.05 sec

Thermal Group Omega t=0.2 sec

Omega Ratio

Omega Ratio

Figure 3.7: Flux omegas for the 0.1 second rod withdrawal transient

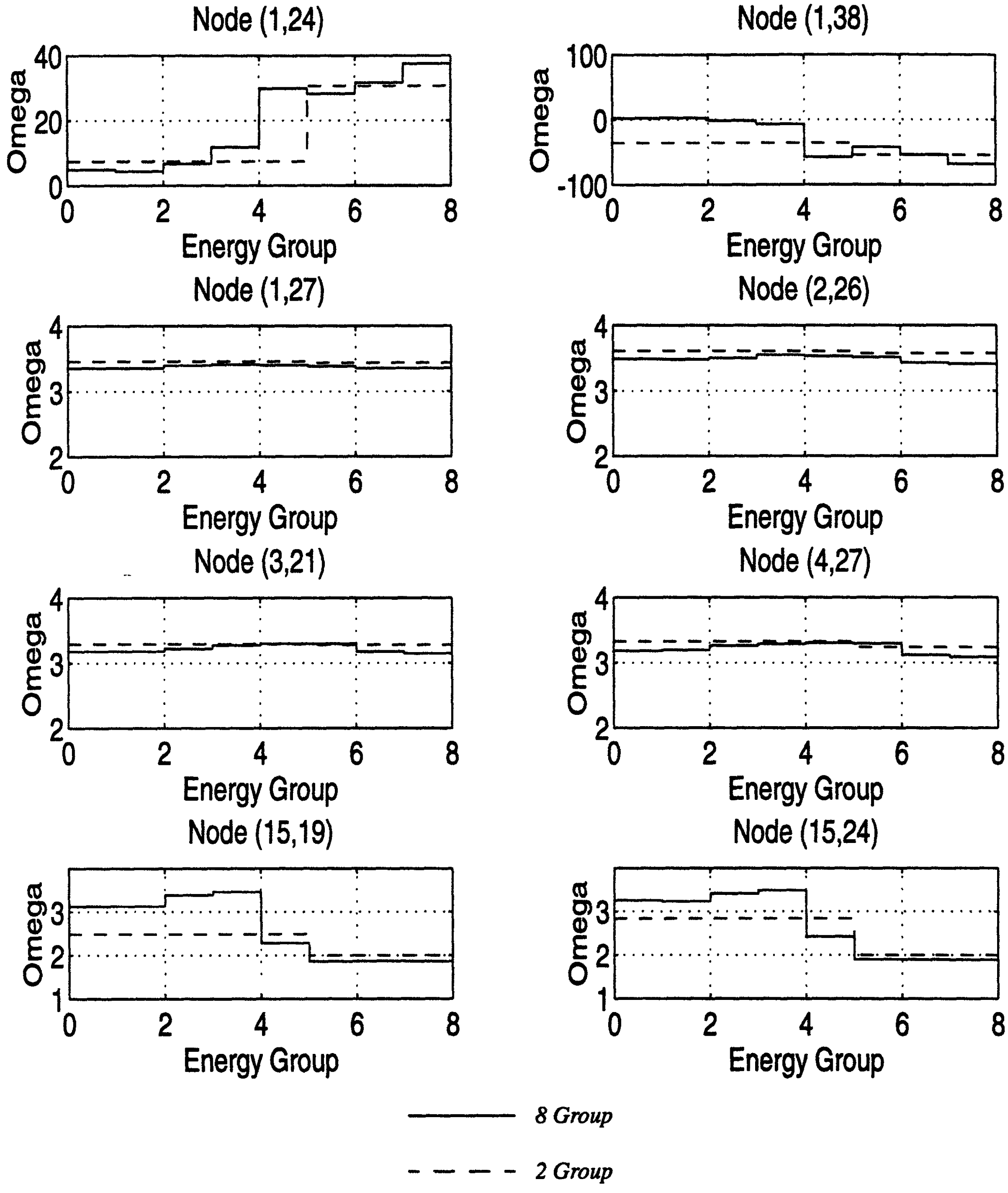

Figure 3.8: Two- and eight-group values of ω_g for various nodes at time 0.02 seconds for the 0.1 second rod withdrawal transient (groups 6,7,8 of the 8-group scheme make up the thermal group of the 2-group scheme). The ω's have units of sec^{-1}.

group - are almost the same.

The bottom two curves on Figure 3.8 are for nodes *(15,19)* and *(15,24)* out in the reflector. Examination of these omega behaviors show that eight group flux omegas, in the nodes where ratio is not unity, fall into two classes such that there is a fictitious thermal cutoff at energy group 4. The two-group values, with thermal cutoff at energy group 5, do not match them very well. This behavior is related to the fact that the thermal group of the two-group model is composed of the last three groups (6,7 and 8) of the eight-group model. There is, however, upscattering from group-6 to group-5 and from group-7 to group-5. Thus there is also upscattering from the thermal to the fast group in the two-group model. The two-group model puts upscattered neutrons into the entire fast group (groups 1-5 of the eight group scheme). However, the eight-group upscattering puts neutrons into only group-5. This suggests that a more accurate two-group model might be one for which the thermal group includes the lowest four groups for the eight-group scheme. Accordingly, the transients were rerun with the fast and thermal groups of the two-group scheme defined as the highest and lowest four groups of the eight-group scheme. Figure 3.9 shows the results at t=0.02 seconds. It can be seen that the eight-group omega values fall into two unique sets both in the reflector and in the nodes where the rod is moving, and the two-group values match them much better.

This omega behavior suggests that using the fast, two-group value of ω for the four fast groups of an eight-group scheme and the thermal two-group value for the four lowest energy groups should yield an eight group pseudo-static eigenvalue very close to 1.

This conclusion was confirmed by using this new thermal energy cut off for the rod removal transient in 10 seconds. Figure 3.10 shows the eight- and two-group omega values at t=2.0 seconds for this transient.

Examination of Equation (3.5) shows that the flux omegas are only part of the picture. Values of the ω_d's also affect the pseudo-static eigenvalue. In fact, for the 10-seconds rod withdrawal transient, the ω_g's are so small ($<2\ \text{sec}^{-1}$ throughout the transient) that (ω_g/υ_g) is almost negligible in comparison with Σ_{tg}. It is chiefly the delayed precursor ω_d's that determine the pseudo-critical eigenvalue.

The two-group model yields a set of $\omega_d(r,t)$'s at all times during a transient, and these can be compared directly to the corresponding ω_d's from the eight-group model. (No extrapolation

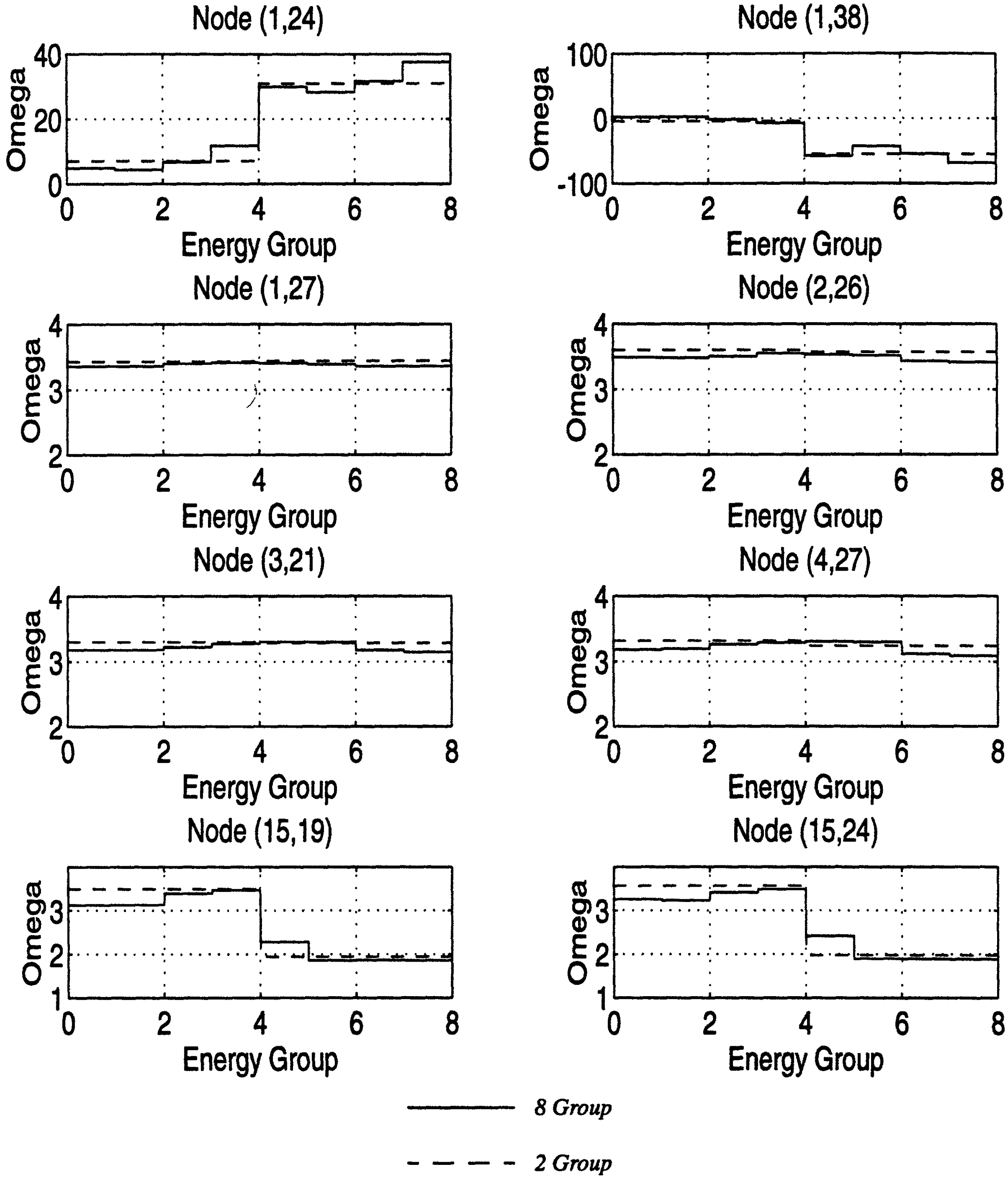

Figure 3.9: Two- and eight-group values of ω_g for various nodes at time 0.02 seconds for the 0.1 second rod withdrawal transient (groups 5,6,7,8 of the 8-group scheme make up the thermal group of the 2-group scheme). The ω's have units of sec^{-1}.

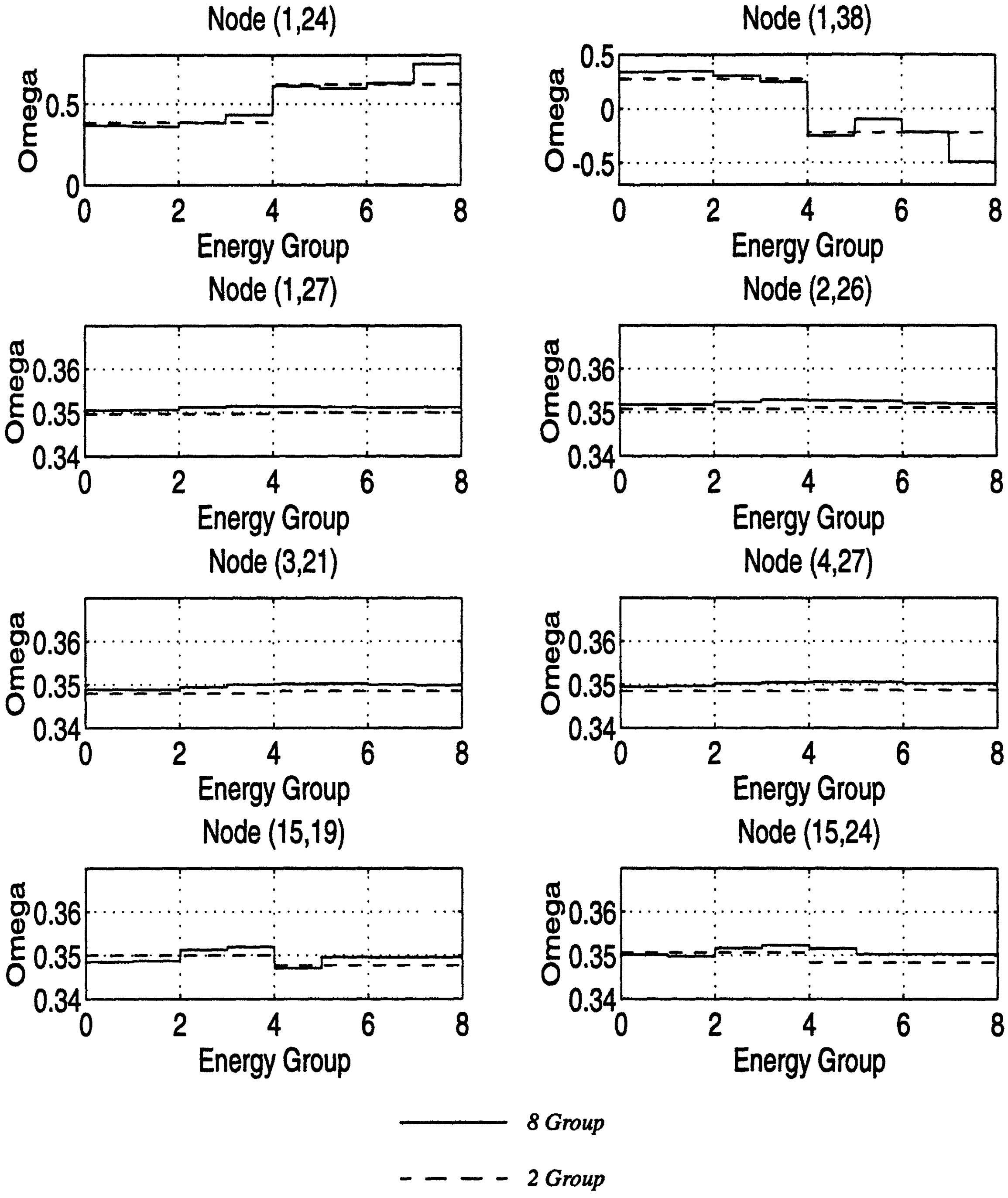

Figure 3.10: Two- and eight-group values of ω_g for various nodes at time 2.0 seconds for the 10 second rod withdrawal transient (groups 5,6,7,8 of the 8-group scheme make up the thermal group of the 2-group scheme). The ω's have units of sec^{-1}.

is required.)

For the 10-second rod withdrawal Figure 3.11 shows the values of ω_d's for the six precursors groups edited at 1.25 seconds into the transient from the eight-group (solid line) and two-group (dotted line) calculations for various fueled nodes. The agreement is excellent and suggests that two-group values of the ω_d's can be used as approximations to the eight-group values.

Table 3.1 shows sensitivities of pseudo-static eigenvalues, λ_{ps}, to ω_d and ω_g values for the 0.1 second rod withdrawal transient. Ideally λ_{ps} should be 1 for the cases where the reference ω_d's and ω_g's are used. The second column of the table shows that for both the two-group and eight-group models, the reference ω's yield values of λ_{ps} differing from the unity by at most 4 pcm (1 pcm=10^{-5}). This deviation is within the round off limits. The last three rows of the second column (using two-group reference values of ω's to represent eight-group values of those quantities and inserting them into eight-group pseudo-static criticality equation) yield the pseudo-static eigenvalue within the same convergence limits. Setting ω_g's to zero makes little difference for this mild transient. As was described earlier, this slow rod removal transient falls into the category characterized by the delayed omega modes. Setting ω_d values to zero affects the pseudo-critical eigenvalue significantly. Numbers in parenthesis show the differences in λ_{ps} value with and without ω's set to zero (the so called omega worth). The close agreement in pseudo-static eigenvalues and delayed precursor omega worths between two-group, eight-group, and eight-group extrapolated from two-group indicates that the procedure we are using for inferring eight-group values of ω_d's from two-group results is quite accurate.

In the fast rod withdrawal transient, the pseudo-critical eigenvalue is governed by very large values of the flux omegas. Table 3.2 shows the sensitivity of pseudo static eigenvalues to these ω-values for the fast rod removal transient. As happens with the slow rod withdrawal transient, reference values of ω_g's and ω_d's result in pseudo-static eigenvalues were close to unity for both the two- and eight-group as well as when the eight-group values are inferred from the two-group results. The values of (λ_{ps} - 1) that result from setting ω_g's to zero are two orders of magnitude greater than when reference ω-values are used. For this fast transient, sensitivity to the ω_d's is less. Again the close agreement in the flux omega worths indicates the accuracy of the extrapolation scheme for the flux omegas.

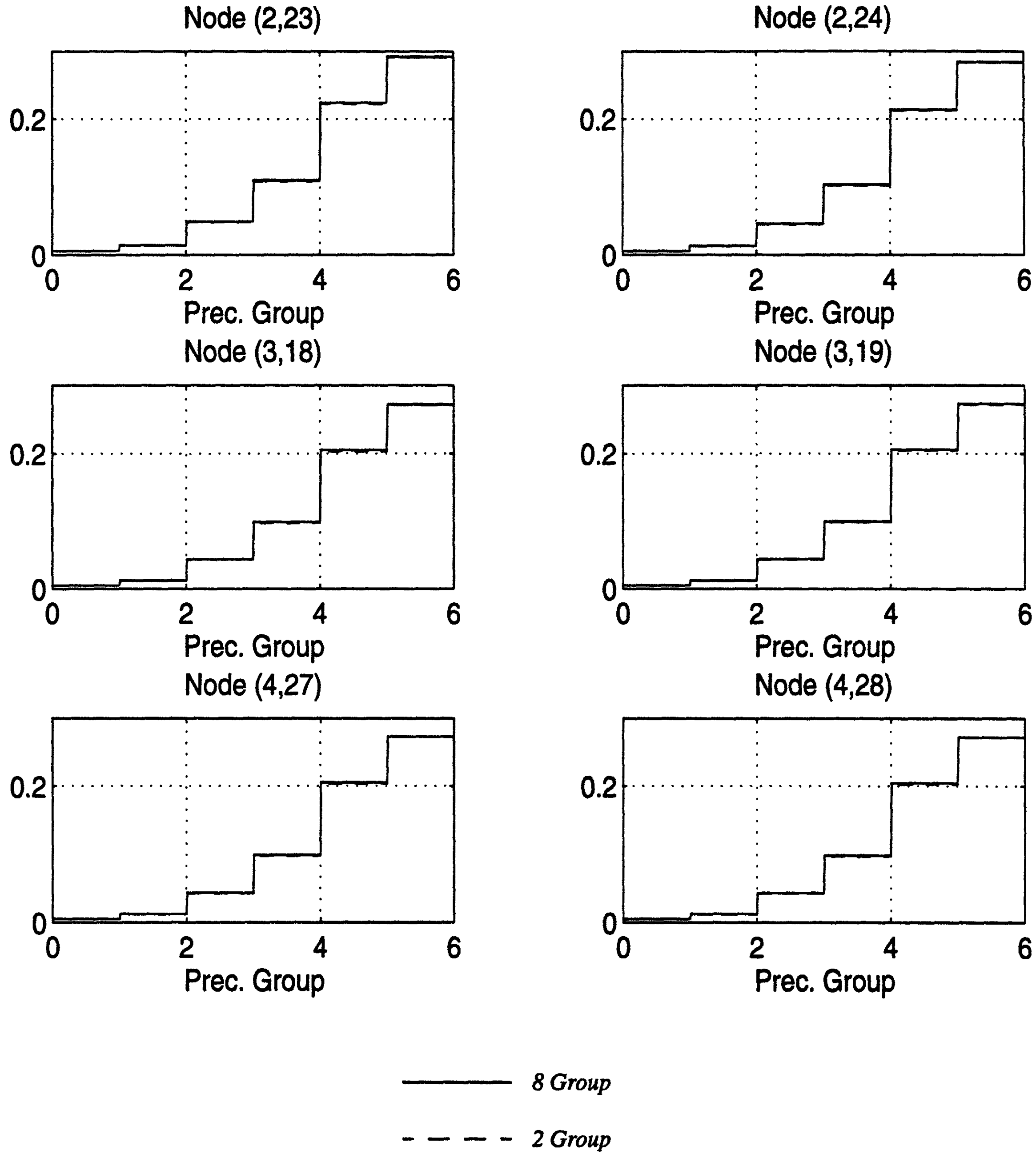

Figure 3.11: Values of ω_d's at t=1.25 seconds at various fuel nodes for the 10 seconds rod withdrawal transient. The ω's have units of sec^{-1}.

Table 3.1: Sensitivity of pseudo-static eigenvalues to ω_g's and ω_d's for the 10 second rod withdrawal transient

Time (sec)	λ_{ps} ω_g, ω_d	λ_{ps} $\omega_g=0$	λ_{ps} $\omega_d=0$
2 group calculation using 2 group omegas			
0.9	1.00003	1.00024 (21)*	1.00123 (120)
1.8	1.00003	1.00030 (27)	1.00210 (207)
2.7	1.00004	1.00042 (38)	1.00301 (297)
8 group calculation using 8 group omegas			
0.9	1.00003	1.00023 (20)	1.00123 (120)
1.8	1.00003	1.00029 (26)	1.00210 (207)
2.7	1.00003	1.00040 (37)	1.00302 (299)
8 group calculation using 2 group expanded omegas			
0.9	1.00002	1.00023 (21)	1.00123 (121)
1.8	1.00004	1.00031 (27)	1.00211 (207)
2.7	1.00003	1.00041 (38)	1.00301 (298)

(*) Numbers in parenthesis are the difference in the eigenvalue in pcm with and without setting the ω's to zero

Table 3.2: Sensitivity of pseudo-static eigenvalues to ω_g's and ω_d's for the 0.1 second rod withdrawal transient

Time (sec)	λ_{ps} ω_g, ω_d	λ_{ps} $\omega_g=0$	λ_{ps} $\omega_d=0$
2 group calculation using 2 group omegas			
0.009	0.99998	1.00128 (130)*	1.00008 (10)
0.018	1.00001	1.00207 (206)	1.00031 (30)
0.027	0.99996	1.00282 (286)	1.00053 (57)
8 group calculation using 8 group omegas			
0.009	1.00001	1.00132 (131)	1.00012 (11)
0.018	1.00002	1.00207 (205)	1.00029 (27)
0.027	0.99999	1.00283 (284)	1.00055 (56)
8 group calculation using 2 group expanded omegas			
0.009	0.99997	1.00130 (133)	1.00008 (11)
0.018	1.00005	1.00215 (210)	1.00033 (28)
0.027	0.99994	1.00284 (290)	1.00049 (55)

(*) Numbers in parenthesis are the difference in the eigenvalue in pcm with and without setting the ω's to zero

The Light Water Ingress

As was done for the control rod ejection transient, to investigate the question of how multigroup omegas can be inferred from few-group results, the ω's generated by the two-group nodal model were compared to those generated by an eight-group model using the nodal transient code ZAQ. Interpolation tables of nodal parameters as a function of heavy water-light water mixture location in the core were generated from the static, eight-group TWODANT calculations. Since change in the scattering cross section is the most important contributor to this transient, the thermal group cutoff was changed to energy group 5 allowing an upscattering from group 2 to group 1 in two-group scheme. Thus, groups 1-5 of the eight-group scheme form the fast group of the two-group scheme and groups 6-8 of the eight-group scheme form the thermal group of the two-group scheme. Omegas edited from eight-group and two-group transient solutions were compared. Figure 3.12 shows that comparison for various nodes in the core at 0.18 seconds. At that time, the heavy water-light water mixture front reaches the top of the lower fuel element. (Figure 4.7 shows the mixture front location at time 0.18 seconds.) The locations of the nodes can be seen in Figure 3.4.

In nodes that have already been occupied by the heavy water-light water mixture, low energy fluxes are rising faster than the high energy fluxes. The figures show that, especially for the last two energy groups, two-group omegas match the eight-group omegas very well. We believe that those are the omegas that determine the pseudo-static eigenvalue. Since flux omegas appear as ω_g/υ_g in the pseudo-static equations, for higher energy groups which have higher group speeds, ω_g/υ_g terms are small compared to the corresponding group removal cross sections. (For example, collision frequencies, $\Sigma\upsilon_g$, for outer D_2O reflector nodes from the energy group-one to energy group-eight are 1.7×10^8, 6.2×10^7, 1.0×10^6, 2.4×10^5, 1.5×10^5, 1.0×10^5, 5.6×10^3, 2.3×10^4 $\sec^{-1}$ respectively.) For the nodes in the reflector region and the nodes which are not occupied by the mixture, all ω_g's-both eight-group and two-group- are almost same. Because of that observation, the fast two-group value of omegas was used for the first five groups of eight-group scheme, and the thermal two-group value of omegas was used for the lowest three energy groups. However, the omega behavior in the lower plenum nodes, such as *(10,20)*, suggests that a three-group scheme might there yield more accurate results for this particular transient.

Figure 3.13 displays analogous results for the delayed precursor periods (ω_d's) at 0.18

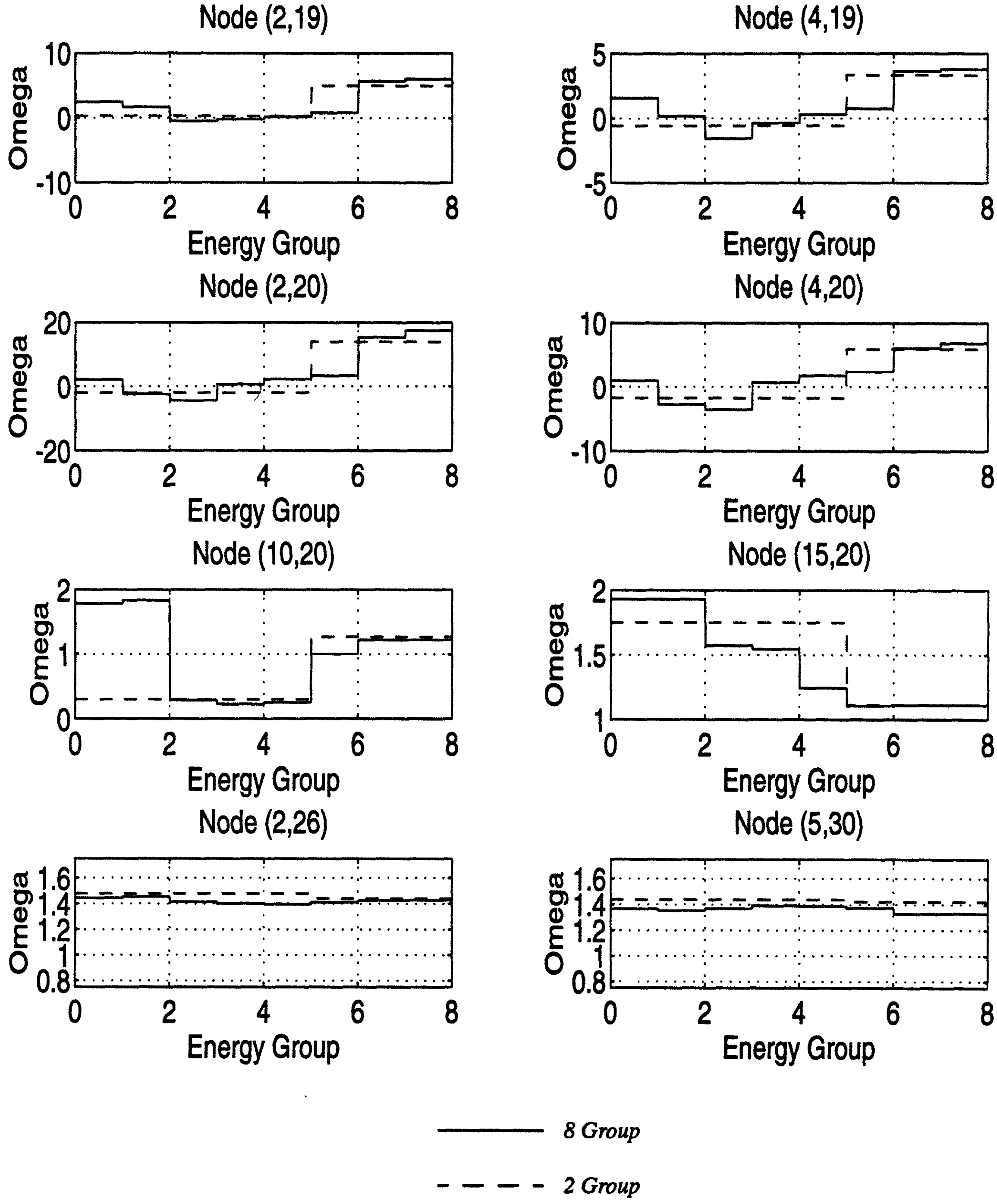

Figure 3.12: Two- and eight group values of ω_g's for various nodes at time 0.18 sec for the light water ingress event (groups 6,7,8 of the 8-group scheme make up the thermal group of the 2-group scheme). The ω's have units of sec^{-1}.

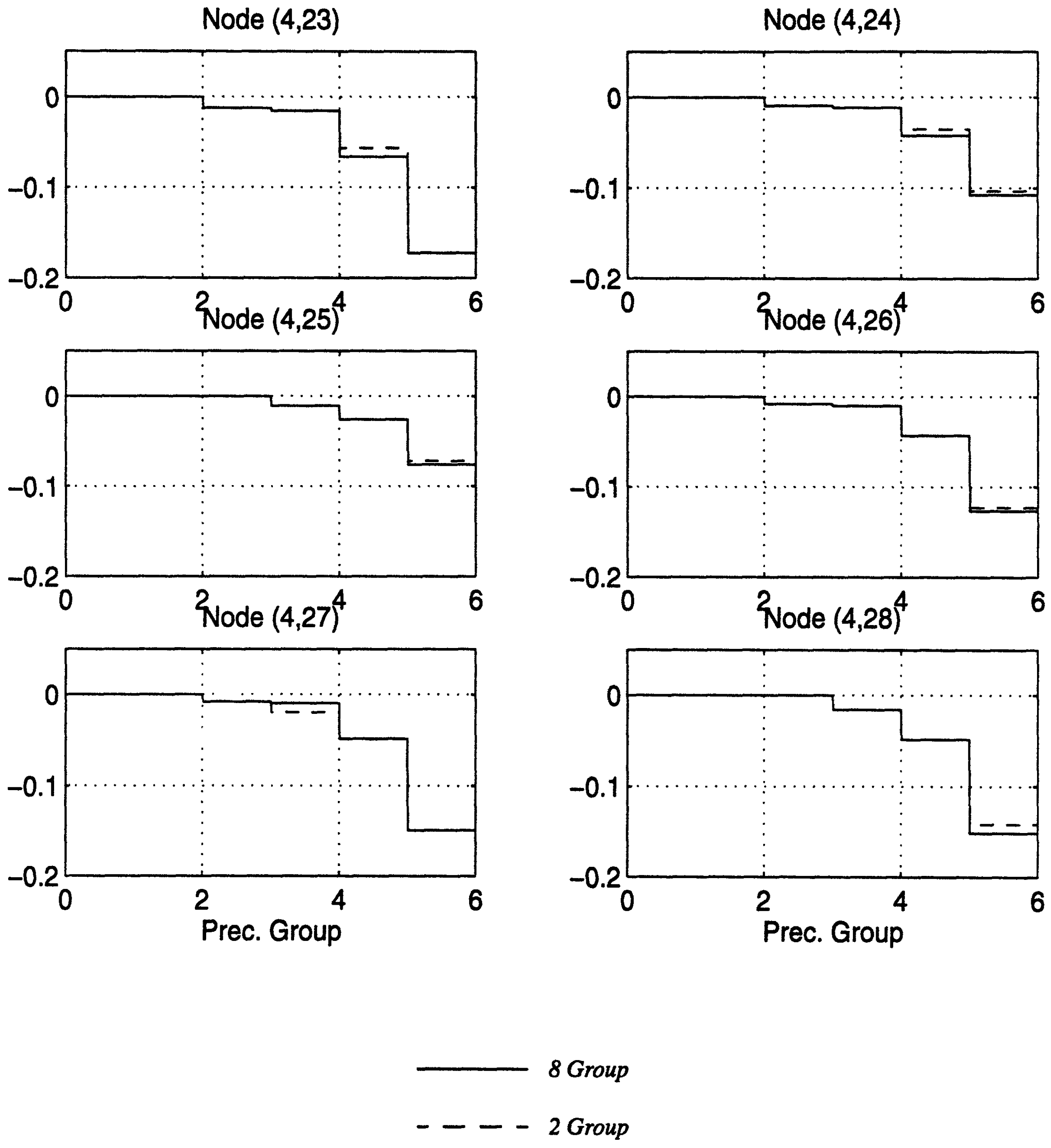

Figure 3.13: Two - and eight group values of ω_d's for the outer fuel element nodes at time 0.18 sec. for the light water ingress event. The ω's have units of sec^{-1}.

seconds. As for the rod withdrawal transients, the agreement is excellent. At that time step, because of the initial negative reactivity insertion (this will be explained in Section 4.4), the delayed precursor periods are negative.

The sensitivity of the pseudo-static eigenvalue to these flux and precursor omegas was also examined. Table 3.3 shows, for the first half of the transient, the pseudo-static eigenvalues calculated by using the omegas found from two-group and eight-group as well as eight-group values inferred from two-group values.Again the extrapolation schemes yield good results and the sensitivity of λ_{ps} to ω values is as expected.

Table 3.3: Sensitivity of pseudo-static eigenvalues to ω_g's and ω_d's for the light water ingress event

<table>
<tr><th>Time (sec)</th><th>λ_{ps}
ω_g, ω_d</th><th>λ_{ps}
$\omega_g=0$</th><th>λ_{ps}
$\omega_d=0$</th></tr>
<tr><td colspan="4">2 group calculation using 2 group omegas</td></tr>
<tr><td>0.100</td><td>0.99995</td><td>0.99992 (-3)*</td><td>0.99999 (4)</td></tr>
<tr><td>0.167</td><td>0.99996</td><td>0.99961 (-35)</td><td>0.99971 (-25)</td></tr>
<tr><td>0.182</td><td>0.99998</td><td>1.00108 (110)</td><td>0.99988 (-10)</td></tr>
<tr><td colspan="4">8 group calculation using 8 group omegas</td></tr>
<tr><td>0.100</td><td>1.00001</td><td>0.99998 (-3)</td><td>1.00000 (-1)</td></tr>
<tr><td>0.167</td><td>1.00000</td><td>0.99961 (-39)</td><td>0.99971 (-29)</td></tr>
<tr><td>0.182</td><td>1.00002</td><td>1.00112 (110)</td><td>0.99988 (-14)</td></tr>
<tr><td colspan="4">8 group calculation using 2 group expanded omegas</td></tr>
<tr><td>0.100</td><td>0.99998</td><td>0.99996 (-2)</td><td>1.00001 (3)</td></tr>
<tr><td>0.167</td><td>0.99994</td><td>0.99958 (-36)</td><td>0.99969 (-25)</td></tr>
<tr><td>0.182</td><td>0.99996</td><td>1.00107 (111)</td><td>0.99985 (-11)</td></tr>
</table>

(*) Numbers in parenthesis are the difference in the eigenvalue in pcm with and without setting the ω's to zero

3.3.4 Extrapolation Procedures: Flux Omega Angular Dependency

In the previous section we have shown that, with proper choice of the thermal group cut off, flux omegas can be expanded from few-group to multigroup quite accurately. Unfortunately, in the discrete ordinate form of the pseudo-static equations, for the flux omega there is an additional directional dependency. From the diffusion theory approximation, no such angular dependency information is available.

For space dependent kinetics problems, according to Henry [H-5], ω-modes can be found from the solution of a generalized inhour equation. If ω_i's are the roots of the inhour equation, the time dependent flux during any time can be written as the sum

$$\Psi(\underline{r},\underline{\Omega},E,t) = \sum_i A_i \Psi_i^{(\omega)}(\underline{r},\underline{\Omega},E)e^{\omega_i t} \tag{3.17}$$

where the $\Psi_i^{(\omega)}(\underline{r}, \underline{\Omega}, E, t)$'s are eigenfunctions (ω-modes) corresponding to the ω_i's.

The ω-modes corresponding to higher order energy and angular effects die out very quickly so that the asymptotic time behavior of the flux and delayed precursors is determined primarily by the seven roots and corresponding eigenfunctions of the standard inhour equation. Of course asymptotic time behavior is not reached in the transients if the reactivity is not constant. Hence, the situation is more complicated for the instantaneous flux and precursor omegas which are used in our pseudo-static validation model. Nevertheless we believe that adjustments in spectra and angular distribution following a perturbation occur very quickly so that the $\Psi_i^{(\omega)}$'s in Equation (3.17) that persist all have the same angular dependence. Hence all their spherical harmonic components behave as $e^{\omega_i t}$. Thus we assume that there is no directional dependency in the time behavior of the angular flux. For all directions the omega value is the same for a given node and energy:

$$\omega_g(r,\Omega_1,t) = \omega_g(r,\Omega_2,t) = \ldots = \omega_g(r,\Omega_D,t) = \omega_g(r,t)$$

Once this assumption is made, the scalar flux omegas found from the transient nodal solution can be used for the directional flux omegas.

Moreover, a self sustaining reactor has a very short memory such that a neutron, while creating its own chain, diffuses away from its birth place, and the distribution, a few scattering mean free paths beyond its birth place, is independent of the initial condition imposed on it [G-1]. This implies that perturbations are local and supports the assumption of direction independent flux omega behavior.

In order to test the validity of this assumption, angular flux shapes found from static transport solutions (8 energy group, S_4, P_1 approximation) for two different control rod positions were compared. The first case corresponds to a fully inserted control rod position. For the second case the control rod was 20% withdrawn from a node. Note that, when transient equations are solved, time steps are chosen so small that the fraction of the rod removed is much less than 20% during a time step. Hence, no such severe changes are expected during actual transient solutions. Other high order calculations (S_{10}, P_3) show that the neutron distribution in the D_2O reflector tank is isotropic [H-6]. In Figure 3.14, changes in the angular flux shapes ($= ln\ (\Psi_2/\Psi_1)$, where Ψ_1 is the angular flux shape for rod in and Ψ_2 is the angular flux shape for 20% withdrawn rod positions) for energy group-8 and for each discrete directions (12 discrete directions for an S_4 approximation) are plotted for various regions in the core. In the calculations, both flux shapes were normalized to the same power level. It was found that the isotropic distribution does not change with the transient variable (e.g. control rod position) for the nodes in the reflector. Although, the neutron distribution is not isotropic in the central fuel and control rod regions, other than for nodes in which, or near which the perturbation is introduced, no strong directional time dependency of angular flux was observed. Similar comparisons for other energy groups show the same trend.

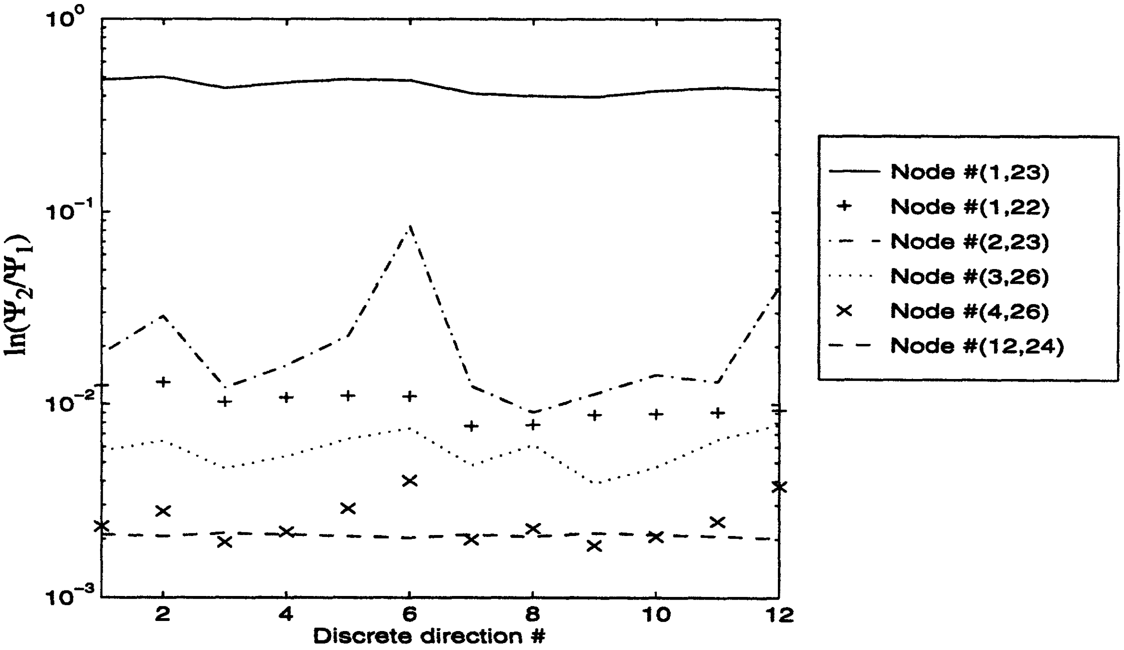

Figure 3.14: Changes in angular flux shapes as a result of control rod removal (Location of nodes can be seen in Figure 3.4)

As has already been emphasized, flux omegas play an important role for the regions where the absorption cross section is small. Even though the magnitude of the flux omegas is high in the nodes where a perturbation is introduced, because of the large absorption cross section, the time variation of the angular fluxes is much smaller than the collision frequency $\upsilon\Sigma_t$. Hence the use of scalar flux omegas for directional flux omegas does not affect the pseudo-static eigenvalue test.

3.4 Summary

In this chapter, we introduced an indirect test for the validation of a few-group, time-dependent nodal model for transient analysis of tightly coupled reactors. The crucial part of this validation model is the expansion of the few-group omegas to multigroup omegas. Since there is no theoretical basis for that expansion, calculational studies were conducted to examine the nature of the group flux and delayed precursor omegas. It was found that for all transients, few-group values of the delayed precursor omegas can be used for multigroup values. By choosing properly the thermal group cut off for the two-group scheme, two-group omegas can also be expanded to multigroup. It was also found that, flux omegas play a major role:

- for the transients in which the rate of reactivity change is large,
- for the nodes where the absorption cross section is small,
- for the lower energy groups.

Finally we investigated the angular dependency of the flux omegas, and argued that they do not play a significant role in the determination of the pseudo-static eigenvalue.

In the next chapter, we shall analyze various reactivity transients for the ANS reactor and apply the indirect test to investigate the accuracy of the different transient models.

Chapter 4

Application of the Validation Model to Transients of the ANS Reactor

4.1 Introduction

In this chapter, results of the various reactivity transients of the Advanced Neutron Source reactor will be presented. Before it was cancelled in early 1995, the preconceptual design of the ANS reactor had been changed considerably. One of the major design changes was the replacement of the two-element core with the three-element core in order to reduce the power density because of safety concerns. The present validation studies were first started for the two-element ANS core. The control rod withdrawal transients were analyzed and pseudo-static tests were applied. Following the design changes, the latest three-element core [S-2] was taken as a final model in our studies. In addition to the control rod withdrawal transients, a light water ingress event has also been analyzed for the new core. Since the nature of the transient is independent of the core configuration (either two- or three element core), we shall here present the studies and results in detail for the three-element ANS core. Results of the two-element ANS core control rod removal transients are given in Appendix A-2. In each transient, indirect eigenvalue and flux shape tests have been applied to various transient models. Some important parameters of interest were also compared.

4.2 The Three-Element ANS Core Transient Model

The model being considered for the transient analysis is the same one used in the previous chapter (shown in Figure 3.4). The cross-section and discontinuity factor sets for various conditions expected throughout transients were generated from eight-group TWODANT calculations with S_4, P_1 approximations. Eight-group cross sections, which were processed from the ANSL-V 99-group master cross section library using modules from the SCALE and AMPX code systems [G-4], were provided by Oak Ridge National Laboratory for each material comprising the reactor. In this eight-group cross section library two radial traces were used to account for the axially offset fuel elements. One trace included the data for the upper fuel elements and the other included for the lower fuel element. For each of these traces, there were two sets of data for a controlled and uncontrolled cases.

As to be expected, modelling of very thin zones (~5 mm) for full sized cores (~2-4 m) requires a large amount of computer memory and computing time. Earlier attempts to use variable mesh spacing for the discrete ordinate calculations have resulted in negative transport fluxes. (It is known that the solution of discrete ordinate equations for situations such that $\Delta R/\Delta Z$ is very small or very large can result in negative fluxes.) Therefore, in order to reduce the memory requirement and also the computer running time, instead of modelling each material zone separately, small regions in the core were homogenized with neighboring zones. In these calculations, a convergence criteria on the eigenvalue of 10^{-6} and on the group-fluxes of 10^{-5} was used. With these convergence criteria and 275x100 mesh spacings, each TWODANT (S_4, P_1) calculation requires 7-8 hours on a SunSPARC Classic workstation.

Node-homogenized two-group cross sections and discontinuity factor ratios were edited from static TWODANT calculations, and transients were run using the interpolation schemes. In these calculations six delayed neutron precursor groups were used. Feedback effects were not modelled. For static calculations, the eigenvalue and group-flux (for fueled nodes) convergence criteria were set to 10^{-6} and 10^{-5} respectively. For transient calculations convergence in the group-flux of 10^{-4} was used. For pseudo-static eigenvalue problems, for both the nodal and the discrete ordinate calculations, static convergence criteria were kept the same as for the static problems.

In the transient calculations, initially core averaged group velocities were used. However comparison of two-group and eight-group transient solutions showed the importance of computing node-dependent values of the two-group neutron velocities from the eight-group, static reference solution. If this is not done, two-group, transient ZAQ calculation power levels and the instantaneous values of the power periods (time derivatives of the logarithms of total powers for the two core models) will differ from the eight-group reference ZAQ solution. If on the other hand, node-dependent, two-group velocities derived from the eight-group reference are employed, the differences reduce significantly. Accordingly node-dependent values were used for the transient solutions.

4.3 Control Rod Removal Transients

The transients analyzed were the complete withdrawal of one of the central control rods from its initial position with the tip at the plane between the upper and the lower reactor halves in 10 seconds (a slow transient) and in 0.1 seconds (a fast transient). Transients were simulated by reducing the control rod Hafnium material density by one third of its original value in the nodes where rod is being removed and adding the same amount to the nodes where rod is being inserted. Figure 4.1 shows the control rod positions at the beginning and at the end of the transient. As shown in the figure, at the end of the transient one control rod is removed 60 cm from the core axial mid plane spanning seven axial nodes.

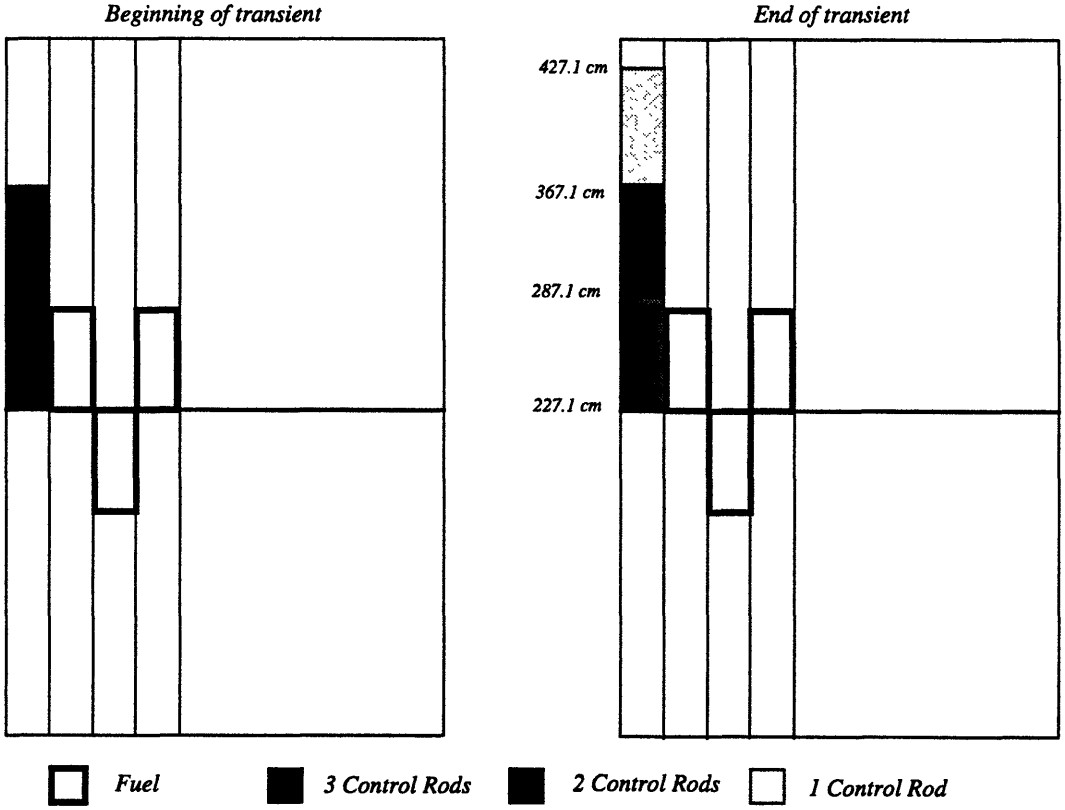

Figure 4.1: Schematic of the rod removal transient

Tables of cross section and discontinuity factor ratios for the 15 control rod positions were constructed from full core, static TWODANT calculations. Of the 15 rod positions, eight correspond to node boundaries and seven correspond to positions half way out of a node. For the adiabatic approximation control rod reactivity curves and tables for flux shape functions were tabulated for these 15 control rod positions, and at any intermediate step during the transient their values were found by linear interpolation.

Various transient models were compared in terms of scram time, reactor power at the time of scram and integrated power till scram. The time when the total flux reading in detector nodes (shown in Figure 3.4) increases 15% over its full power nominal value was taken as the scram-time. Although the scram time predictions by various models have been compared, it was assumed that the control system failed to trip and cause control rod insertion. That assumption allowed us to compare models beyond the scram time.

For all models (the space-time, point kinetics and adiabatic), the initial adjoint flux shape was taken as the weight function for the calculation of the point-kinetics parameters. For the point kinetics model the initial flux shapes were used throughout the transient.

4.3.1 The 10 second control rod removal (Slow Transient)

This slow control rod removal transient begins at 0.0 seconds utilizing a time step size of 0.05 seconds. Figure 4.2 shows a plot of reactivity vs. time for the three models. (The lower portion is an expanded plot for the first second of the transient.) Notice that, with a β_{eff} value of $6.9\text{x}10^{-3}$ the reactor becomes super-prompt critical at around 6.0 seconds and runs away. The effect on the reactor power due to the transient is presented in Figure 4.3. Two power-vs.-time curves are shown for the adiabatic approximation dependent upon whether the power is reconstructed using the initial flux shape or those obtained from the criticality calculations used to construct the table of reactivity vs. control rod position. The two curves are indistinguishable in the upper portion of Figure 4.3 and barely distinguishable in its lower portion. Figures 4.2, and 4.3 show that, for this transient, predictions of the adiabatic model are very close to those of the (theoretically more accurate) ZAQ space-time model. The expanded portion of Figure 4.2 (as well as Figure 4.3) suggests that a smoother fit of reactivity vs. rod position might improve accuracy even further. Except for very early time into the transient, the point kinetics approximation is (as expected) very inaccurate.

Table 4.1 shows the values of various quantities of interest for the four different simulations. For the slow transient, in terms of scram time, reactor power etc., all approximations are very close to the reference space-time solution. Since the scram occurs very early in the transient the flux shape is close to the initial flux shape, the point kinetics and

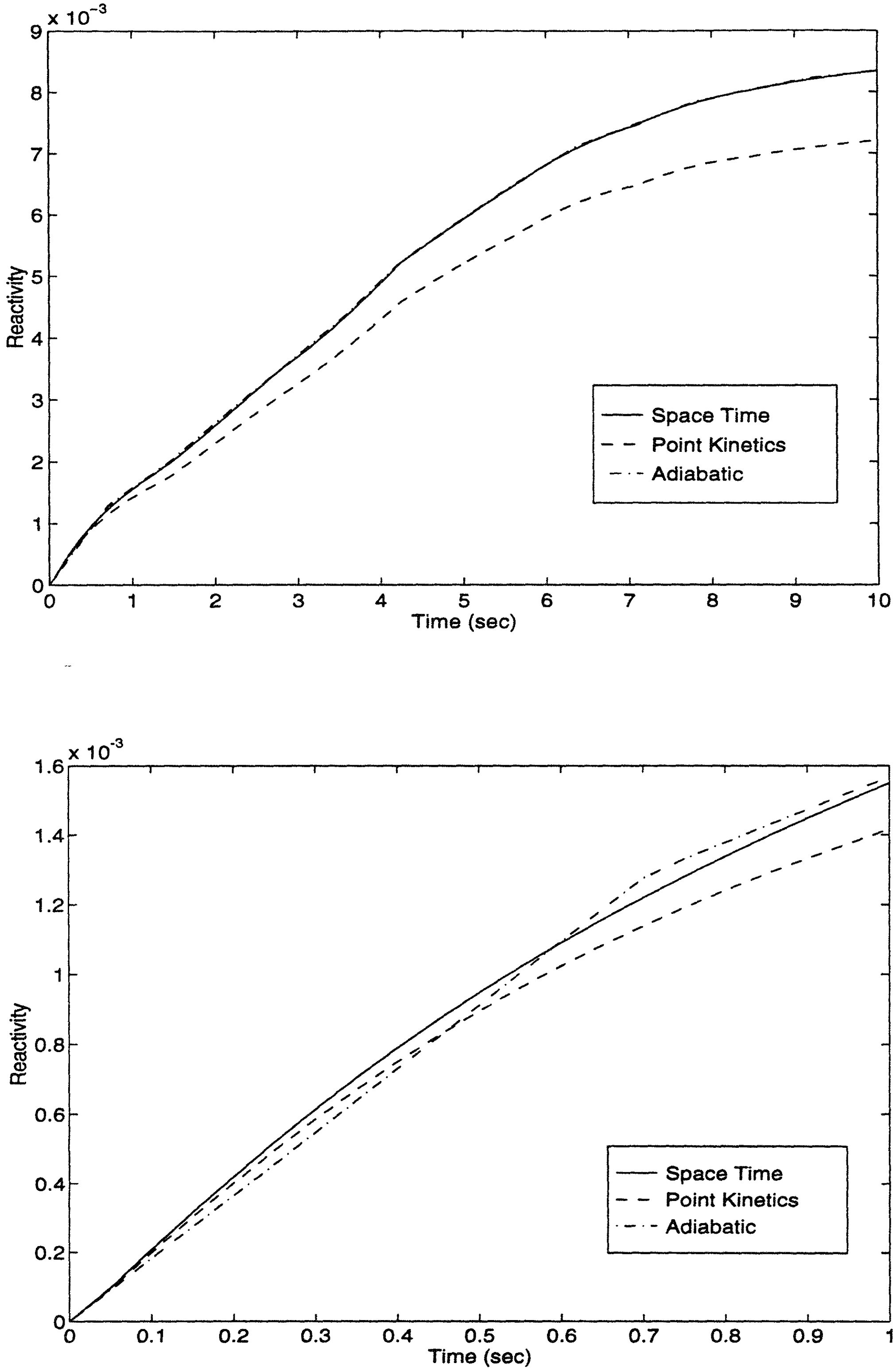

Figure 4.2: Reactivity vs. time for the 10 second rod withdrawal transient for the three-element ANS core without feedback (β_{eff}=6.9x10^{-3})

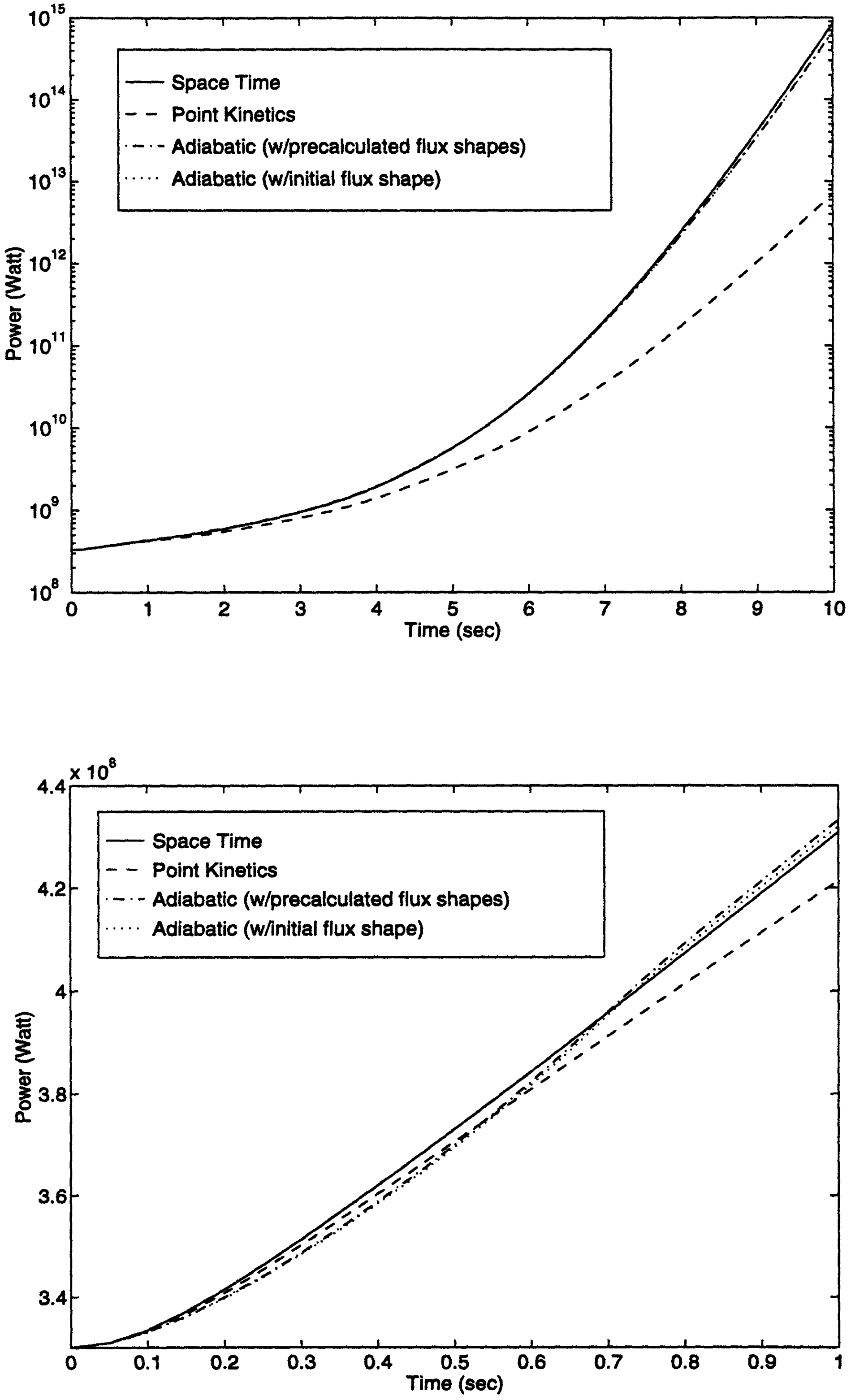

Figure 4.3: Power vs. time for the 10 second rod withdrawal transient for the three-element ANS core without feedback

Table 4.1: Predictions by various models of parameters of interest at the time of 15% overpower scrams for the 10 second rod withdrawal transient without feedback

Method	Scram Time (sec)	Reactor Power at the time of scram (MW)	Integrated Power at the time of scram (MJ)	Highest Powered Node Energy Accumulation (MJ)
Few-Group Nodal (Space-Time)	0.60	384.35	213.13	19.86
Point Kinetics	0.60	380.93	212.26	19.78
Adiabatic with Changing Flux Shape	0.60	382.33	211.88	19.75
Adiabatic with Initial Flux Shape	0.60	381.74	211.70	19.73

adiabatic approximations are acceptable.

In order to perform the pseudo-static validation test, flux and precursor omegas were edited from time dependent solutions and inserted into the pseudo-static model. Table 4.2 shows the pseudo-static test results using the static mode of the nodal code ZAQ. The first columns of the ZAQ results in this table are a measure of the sensitivity of the scheme. Since the ω's from the ZAQ solution at the times listed are inserted into the ZAQ equations, the pseudo-static eigenvalue should all have a value of unity. The deviation from unity is in the fifth decimal digit. We conclude that non-zero values for the fifth decimal digit in the λ_{ps}'s are due to round-off and convergence effects.

The required eight-group ω's for the TWODANT pseudo-static problems were expanded from the two-group values as was described in Chapter 3. The results are presented in Table 4.3. The first column of the TWODANT results is very close to unity which suggests that, if a time dependent, eight-group TWODANT problem could be run, results for reactor power level and distribution would be close to those predicted by the time dependent, two-group ZAQ solution.

We believe that the relatively large differences between ZAQ and TWODANT pseudo-static eigenvalues at 1.25 and 2.5 seconds (at t=1.25 λ_{ps}(TWODANT)-λ_{ps}(ZAQ)=10 pcm and

Table 4.2: The two-group ZAQ solution pseudo-static eigenvalues for the 10 seconds rod withdrawal transient

Time (sec)	Space Time			Point Kinetics	Adiabatic Ch. Flux[1]	Adiabatic Ini. Flux[2]
	Reference	$\omega_d=0$	$\omega_d=\omega_g=0$			
0.50	1.00004	1.00075	1.00097	1.00009	1.00011	1.00011
1.25	1.00002	1.00162	1.00182	1.00020	1.00004	1.00004
2.50	1.00002	1.00284	1.00319	1.00038	1.00004	1.00004
5.00	1.00002	1.00508	1.00598	1.00072	1.00006	1.00006
7.50	1.00001	1.00591	1.00775	1.00100	1.00010	1.00010
10.00	1.00000	1.00610	1.00841	1.00113	1.00011	1.00011

(1) Adiabatic approximation with changing flux shapes
(2) Adiabatic approximation with initial flux shape

Table 4.3: The eight-group TWODANT solution pseudo-static eigenvalues for the 10 seconds rod withdrawal transient

Time (sec)	Space-Time		Point Kinetics	Adiabatic Ch. Flux[1]
	Reference	$\omega_d=0$		
0.50	1.00008	1.00079	1.00013	1.00015
1.25	1.00012	1.00173	1.00032	1.00016
2.50	1.00016	1.00299	1.00056	1.00022
5.00	0.99998	1.00508	1.00072	1.00010
7.50	1.00001	1.00590	1.00099	1.00010
10.00	1.00001	1.00610	1.00114	1.00010

(1) Adiabatic approximation with changing flux shapes

at t=2.5 λ_{ps}(TWODANT)-λ_{ps}(ZAQ)=14 pcm) come from interpolation errors. The similar differences in the pseudo-static eigenvalue prediction by the adiabatic and point kinetics models for the corresponding time steps (e.g. for the point kinetics approximation, differences are 12 and 18 pcm respectively) support this conjecture. Other than these two time steps, both ZAQ and TWODANT eigenvalues for all models agreed within roundoff. Recall from Chapter 3 that, in the point kinetics models, the value of flux omegas are the same for all energy groups and all nodes comprising the reactor. Therefore no extrapolation error takes place while two-group omegas were expanded to eight-group. That implies that the difference comes from errors in the interpolated nodal parameters used by the transient and pseudo-static ZAQ models.

For both tables, the columns with ω_g's and/or ω_d's set to zero provide an example of λ_{ps} values when incorrect values of the instantaneous periods are used for the pseudo-static computations. Here the λ_{ps} values generally differ from unity in the third (rather than the fifth) decimal place. The close agreement in the eigenvalue difference (i.e. $\lambda_{ps}(\omega_d=0)$-λ_{ps}(reference)) between ZAQ and TWODANT calculation also indicates the accuracy of the extrapolation scheme used for delayed neutron precursors.

When the point kinetics or adiabatic approximations are used, the solution of the point kinetics equations combined with the appropriate shape functions provides the ω_g and ω_d values. The results in Tables 4.2 and 4.3 suggest that the point kinetics approximations provide an inaccurate simulation for this transient, whereas the adiabatic approximation should be quite accurate.

Another way to test the accuracy of the adiabatic approximation is to compare its predictions of flux shape with reference values. The two-group ZAQ results provide an opportunity for this comparison. The comparisons of the pseudo-static flux shapes computed with reference ω_g's and ω_d's (using both ZAQ and two-group fluxes reduced from eight-group TWODANT) match the reference space-time flux shapes to better than 1%.

For this slow transient, the flux shapes computed by the adiabatic model are also very close to reference values except in regions where the flux is very low.

It should be noted that these and the other results presented in this chapter were obtained primarily to show differences in the three models and to apply the pseudo-static test. Even if the reactor failed to scram at 15% over full power, thermal feedback effects (neglected in these calculations) would drastically alter the transients. (This will be discussed in the next chapter.) In fact, if the 15% overpower scram is operated, the point kinetics approximation may be acceptably accurate. Our primary purpose here is to provide a theoretical means of assuring that accuracy.

4.3.2 The 0.1 second control rod removal (Fast Transient)

The control rod removal transient described in the previous section were rerun on the time scale two orders of magnitude faster than the previous one in order to investigate the effect of the rate of introduction of reactivity on various transient models. This fast control rod withdrawal transient was run using a time-step size of 5×10^{-4} seconds. The simulation time was extended to 0.2 seconds.

Figure 4.4 shows the reactivity associated with the transient. Note that the reactivity curve for the adiabatic model is the same for both fast and slow transients. (Reactivity stays constant after t=0.1 seconds for the fast transient.) The figure indicates that the space-time model reactivity is slightly higher than the adiabatic model prediction at time 0.1 seconds and then decreases to its asymptotic value. The difference results from the changing shape function, even though the control rod doesn't move. The shape function and consequently reactivity reach asymptotic values only after the transient associated with the decay of the delayed-neutron precursors ends. Specifically, the shape function decreases in the central core, where the neutron importance is higher, and increases in the heavy-water reflector tank as neutrons are redistributed. The effect on the reactor power is presented in Figure 4.5. Although, the adiabatic approximation is not as accurate for the prediction of the reactor power as in the slow transient (~5% error in the power at t=0.2 seconds) it is superior to the point-kinetics approximation which underestimates the reference power at that time by approximately 20%. The use of precalculated flux shapes makes a slightly better job compared to the use of initial flux shape for the adiabatic model.

Table 4.4 shows the various quantities of interest under the assumption that the reactor scrams when the flux level at a counter in the reflector increases by 15% of its nominal full power value. For this fast transient, the adiabatic and point kinetics approximations fail to predict scram time accurately. Because of the earlier scram time for these models, in which shape function is approximated, reactor power and accumulated power are underestimated.

As was done for the 10 second rod withdrawal transient, flux and delayed precursor omegas were edited from the transient solutions. First, these omegas were directly inserted into the ZAQ pseudo-static nodal model and then values of the multigroup omegas required by the discrete ordinate problem were inferred from the two-group results. The results of the

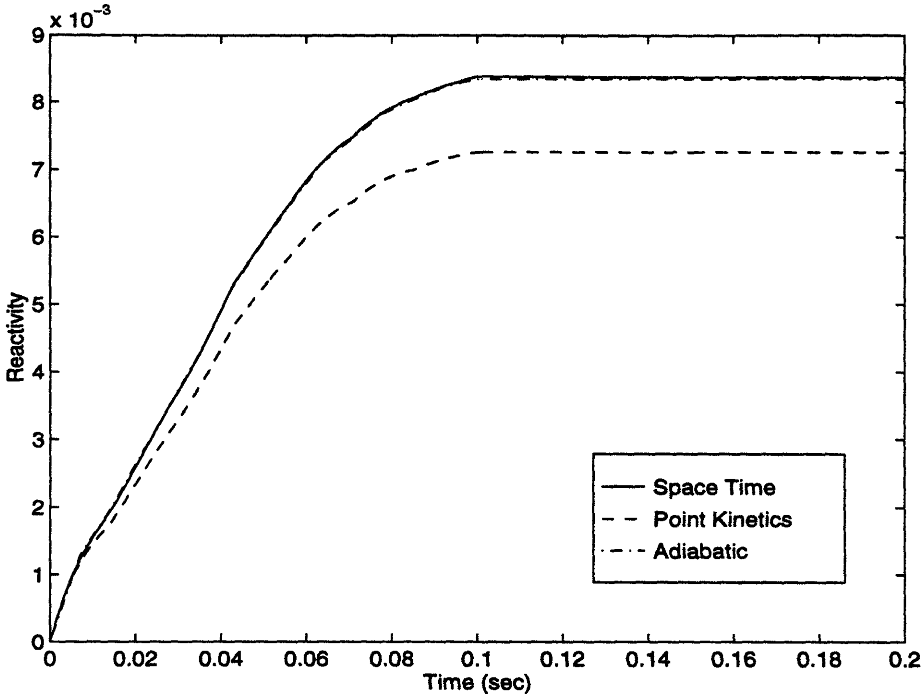

Figure 4.4: Reactivity vs. time for the 0.1 second rod withdrawal transient for the three-element ANS core without feedback (β_{eff}=6.9x10^{-3})

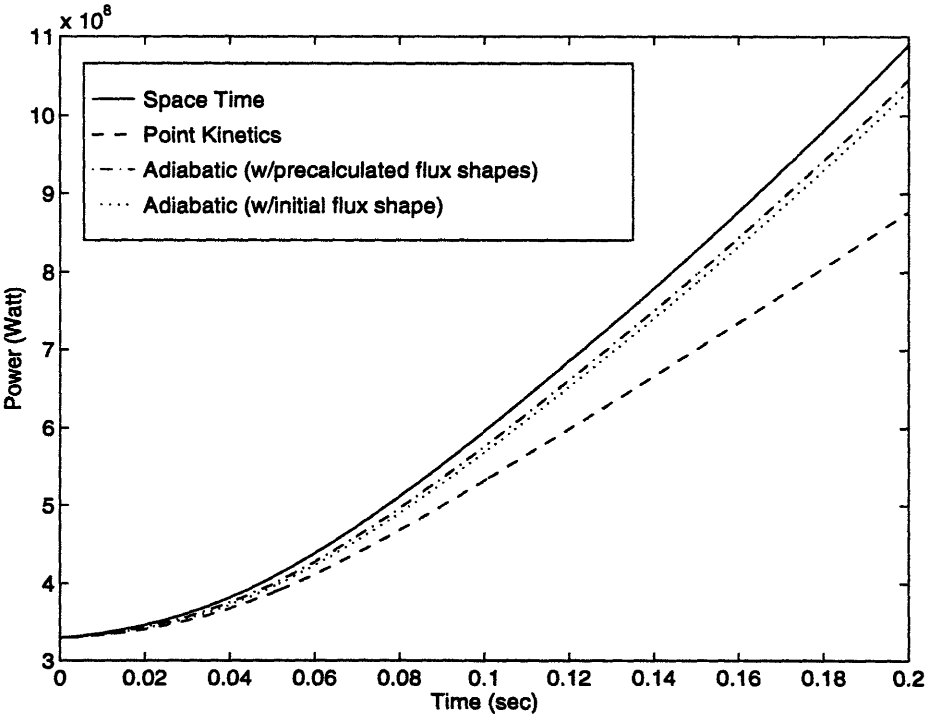

Figure 4.5: Power vs. time for the 0.1 second rod withdrawal transient for the three-element ANS core without feedback

Table 4.4: Predictions by various models of parameters of interest at the time of 15% overpower scrams for the 0.1 second rod withdrawal transient without feedback

Method	Scram Time (sec)	Reactor Power at the time of scram (MW)	Integrated Power at the time of scram (MJ)	Highest Powered Node Energy Accumulation (MJ)
Few-Group Nodal (Space-Time)	0.0505	409.92	18.16	1.69
Point Kinetics	0.0460	379.67	16.00	1.49
Adiabatic with Changing Flux Shape	0.0420	380.12	14.64	1.36
Adiabatic with Initial Flux Shape	0.0435	380.33	15.14	1.41

pseudo-static eigenvalue tests are given in Tables 4.5 and 4.6. As in the slow rod withdrawal transient, both ZAQ and TWODANT pseudo-critical eigenvalues with reference ω_g and ω_d's are very close to unity indicating the accuracy of the space-time solution. It should be remembered that as the transient proceeds, since the interpolated ZAQ parameters are based on *static* TWODANT eigenvalue calculations, an exact match is not expected. However, if the eight-group expanded ZAQ ω-values inserted into pseudo-critical TWODANT calculation yield an eigenvalue close to unity (as has been observed here), we expect that the ZAQ transient results would be close to those from a transient TWODANT calculation if such a calculation were available.

For this fast transient sensitivity of the λ_{ps} was tested setting ω_g to zero in both ZAQ and TWODANT models. The agreement in the flux omega worths is within round-off and convergence limits. Table 4.5 and 4.6 show that after the control rod reached its fully withdrawn position at time 0.1 seconds, flux omegas start to die and the pseudo-static eigenvalue is determined mostly by the delayed precursor omegas.

The deviation in the pseudo-static eigenvalue for the point kinetics model is again in the fourth and third decimal digits. The pseudo-static eigenvalues for the adiabatic model differ only slightly (20-50 pcm) from unity. Although this deviation is larger than the one observed for the slow transient, it is not large enough to justify concluding that the adiabatic model is

Table 4.5: The two-group ZAQ solution pseudo-static eigenvalues for the 0.1 seconds rod withdrawal transient

	Space Time			Point	Adiabatic	Adiabatic Ini.
Time (sec)	Reference	ω_g=0	ω_d=0	Kinetics	Ch. Flux[1]	Flux[2]
0.005	1.00008	1.00097	1.00009	1.00012	1.00010	1.00024
0.0125	1.00003	1.00166	1.00020	1.00017	1.00030	1.00043
0.025	1.00009	1.00278	1.00049	1.00051	1.00039	1.00041
0.050	1.00008	1.00473	1.00133	1.00095	1.00041	1.00043
0.075	1.00003	1.00553	1.00226	1.00122	1.00046	1.00047
0.100	1.00002	1.00538	1.00304	1.00130	1.00045	1.00045
0.200	1.00002	1.00373	1.00466	1.00120	1.00023	1.00023

(1) Adiabatic approximation with changing flux shape
(2) Adiabatic approximation with initial flux shape

Table 4.6: The eight-group TWODANT solution pseudo-static eigenvalues for the 0.1 second rod withdrawal transient

	Space -Time		Point	Adiabatic
Time (sec)	Reference	ω_g=0	Kinetics	Ch. Flux[1]
0.005	1.00010	1.00103	1.00017	1.00012
0.0125	1.00006	1.00176	1.00029	1.00043
0.025	1.00006	1.00289	1.00060	1.00045
0.050	0.99999	1.00477	1.00093	1.00039
0.075	1.00000	1.00553	1.00120	1.00052
0.100	1.00001	1.00537	1.00128	1.00050
0.200	0.99998	1.00372	1.00118	1.00022

(1) Adiabatic approximation with changing flux shapes

deficient.

Examination of the pseudo-static flux shapes, however, does permit this conclusion. The adiabatic flux shapes in the reflector differ significantly from the ZAQ reference values. Figure 4.6 shows the flux shape differences between the adiabatic and reference pseudo-static solution at 0.025 seconds and 0.1 seconds after the rod ejection. The errors indicated are for *normalized* flux shapes and thus do not reflect the error in the *power level.* The differences in the range of 4% to 8% for the thermal group are rather uniform throughout the reflector. They are probably due to the fact that the (ω_g/υ_g) terms (see Equation 3.5), present in the pseudo-static shapes but not in the adiabatic shapes, add to the absorption cross section and are significant compared to the very small absorption cross section for D_2O in the reflector. Because of the low flux level in the outer reflector tank, the values of ω's in this region have very little effect on the λ_{ps} of the pseudo-static problem. (For that reason pseudo-static eigenvalues differ from unity by at most 50 pcm.) On the other hand, these errors in flux shapes have small but measurable effects on the time-til-scram, since flux detectors are located in this region. Figure 4.7 also shows that the flux shapes differ by up to 4% (mostly around 2%) in the central core region because of the difference in the prompt and delayed neutron source shapes.

The corresponding error bounds when the space-time flux shapes are compared with the reference pseudo-static flux shapes found from the two-group ZAQ solutions are less than 0.3% at all points and all times throughout the transient. When two-group fluxes reduced from the eight-group TWODANT calculations were used for the comparisons, differences were found to be less than 1% in the central core region and around 2% in the outer core region (specifically in the lower and upper plenum) where the flux level is very low.

As expected, similar comparisons performed for the point-kinetics model yield differences in the flux shapes as much as 40% in the central core and even larger for the outer reflector nodes.

4.4 The Light Water Ingress Event

One of the possible ANS light water ingress scenarios was simulated in accord with information received from Oak Ridge [G-4]. In that transient, H_2O enters the cleanup system (the only part of the ANS at low pressure) and then is pumped into the primary by the makeup pump (approximately 100kg/sec). This dilutes the primary flow (approximately 2000kg/sec) to give a 5% light water front which enters the core pressure boundary tube (CPBT) and flows into the central hole and the three fuel elements with the velocities 2 m/sec in the central hole, 10 m/sec in the lower and upper plenum and 20 m/sec inside the fuel element.

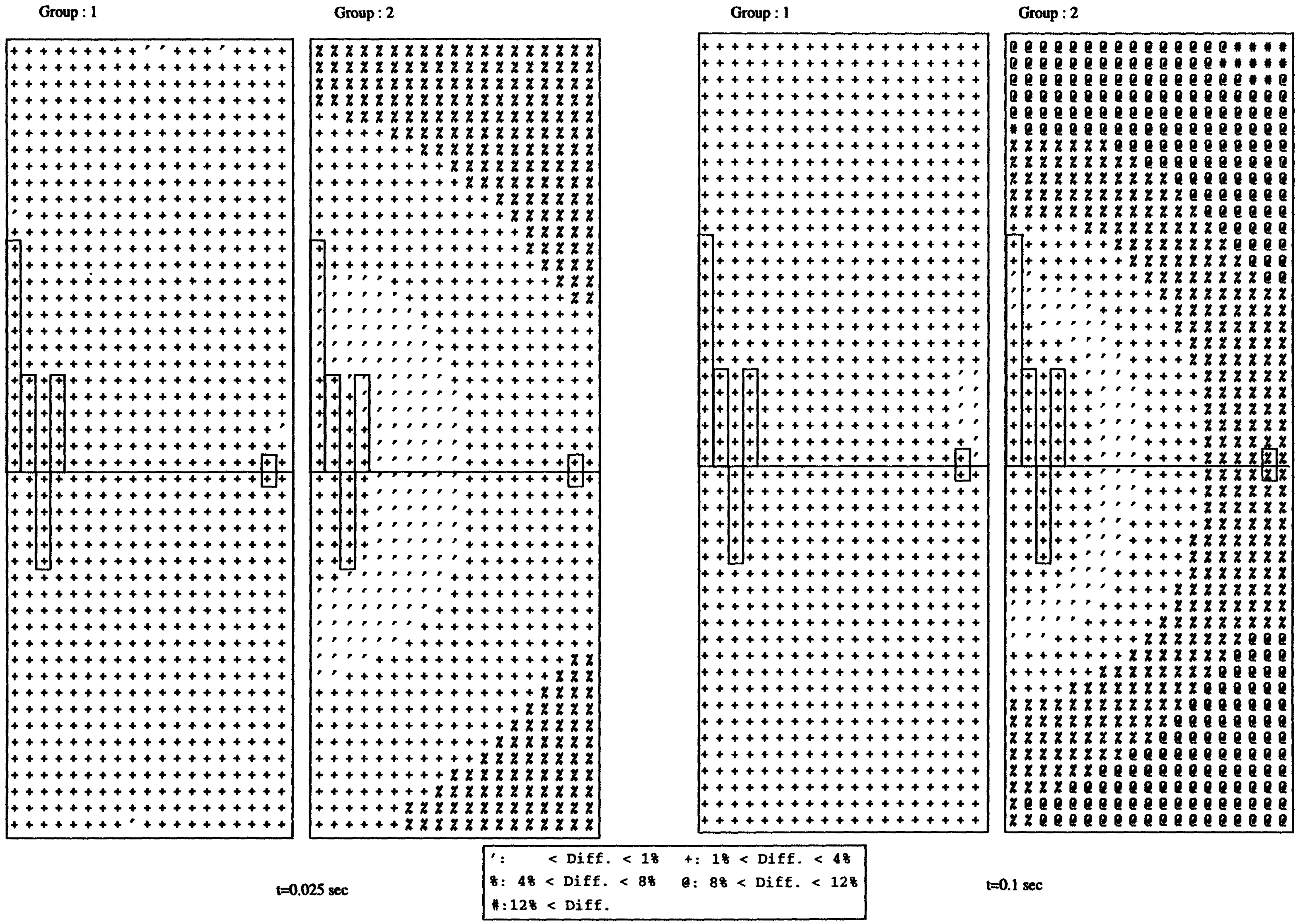

Figure 4.6: Differences at 0.025 and 0.1 seconds between the reference and adiabatic flux shapes for the 0.1 second rod withdrawal transient

Most of the changes in reactor properties take place when the heavy water-light water mixture is rising in the central core region. In order to reduce the computational expense for nodal parameter generation, static TWODANT calculations for various heavy water-light water mixture front positions were performed in detail for the central region of the reactor core. Thus, cross section sets were generated for the mixture front at the upper and lower boundary of each fueled node and the mixture front halfway into a node. To simulate the mixture front in the lower and upper plenum, two sets for each case were generated, the mixture front at the entrance of a plenum and at the exit of a plenum. For the water front position between the plenum inlet and exit, all nodal parameters were interpolated linearly. For all other water front positions, the interpolation schemes discussed in section 3.3.1 were employed. Even with that simplification, 23 full core TWODANT calculations had to be performed. As for the control rod removal transients, tables of reactivity and shape functions as a function of the heavy water-light water mixture position in the core were precalculated for these state points.

The transient began at time 0.0 second and ended at 0.408 seconds with the following time steps:

Time Interval	Δt
0.00 - 0.140	0.000500 sec
0.14 - 0.230	0.000425 sec
0.23 - 0.408	0.000500 sec

A front of heavy water-light water mixture was modelled as progressing from the bottom of the reactor core through the core and central zones at different speeds. At the end of the transient the mixture reached a position in the region between the inner Al-6061 pipe (see Figure B.2) and the core pressure boundary tube corresponding to the top of the reactor vessel. Figure 4.7 shows the position of the front of the mixture at various times during the transient. Notice that for this transient the tips of the central control rods were located at the core mid plane. As for the rod ejection transients, thermal-hydraulics feedback effects were neglected.

Figure 4.8 and 4.9 show the effect on the reactor power and the change in the reactivity associated with this transient. When the mixture starts rising through the lower plenum, increased absorption in the coolant causes negative reactivity insertion. At time=0.15 seconds the water mixture front reaches the bottom of the lower fuel element. Reactivity is still

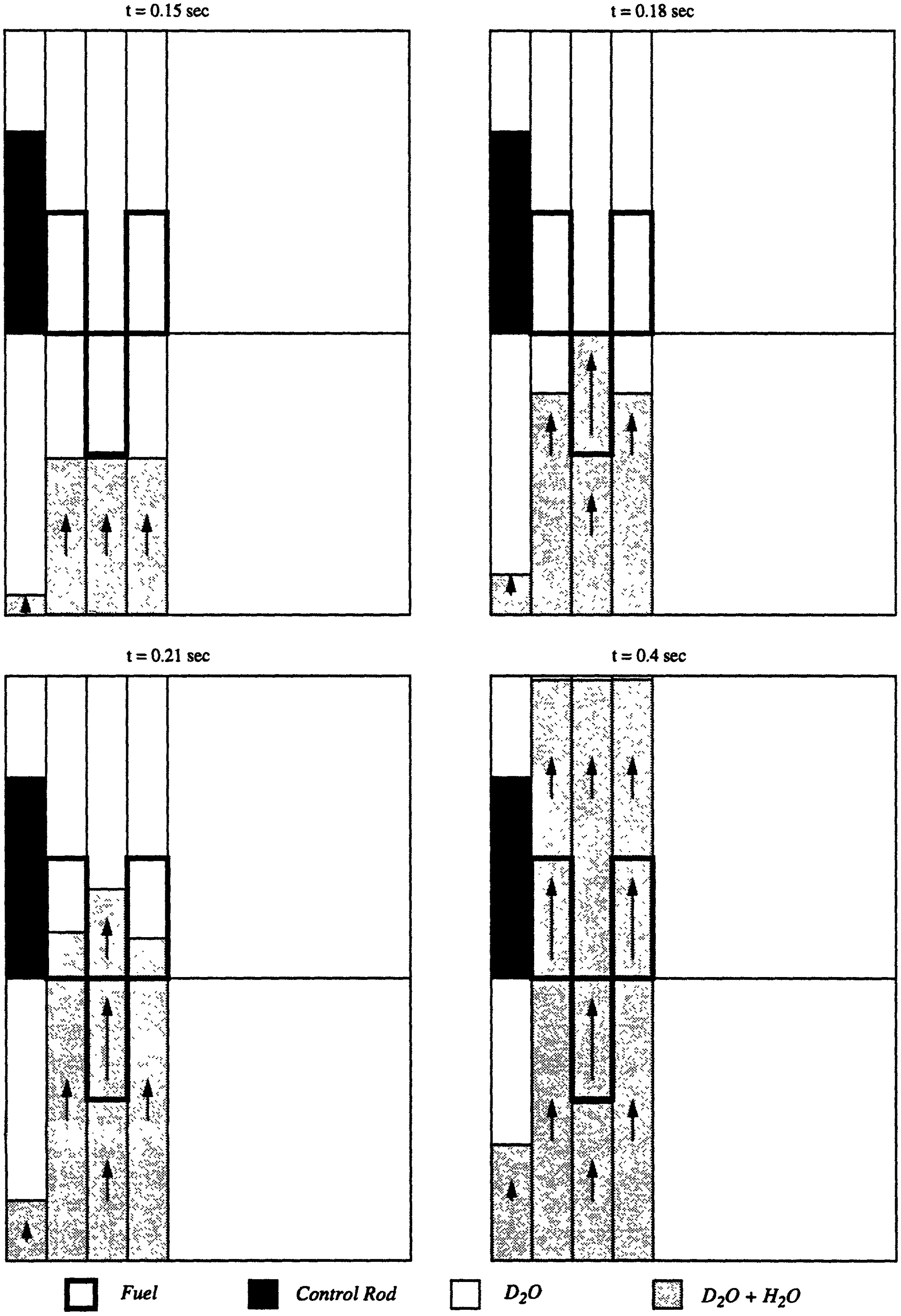

Figure 4.7: Schematic development of light water ingress event

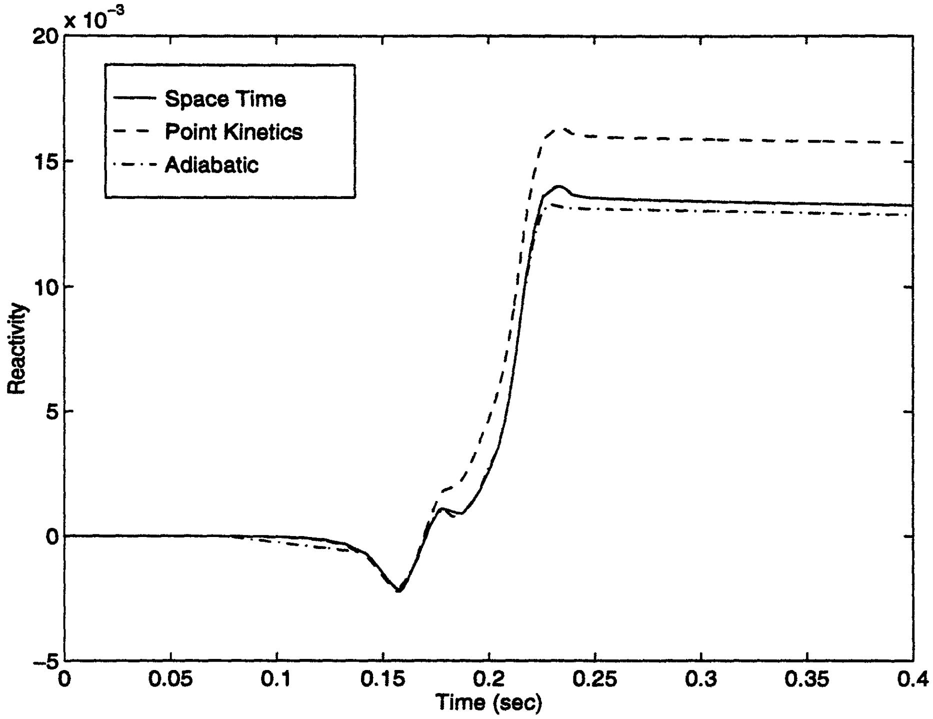

Figure 4.8: Reactivity vs. time for the light water ingress event for the three-element ANS core without feedback (β_{eff}=6.9x10^{-3})

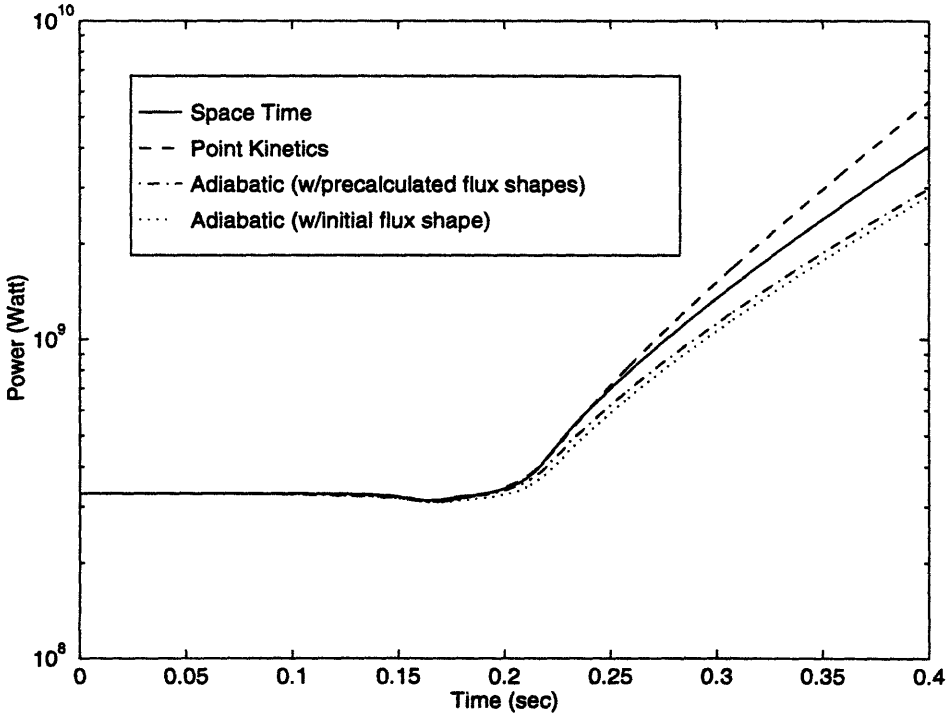

Figure 4.9: Power vs. time for the light water ingress event for the three-element ANS core without feedback

negative at that time. But later, because of the better moderating capabilities of light water, increased thermalization dominates over increased absorption in the coolant and fuel zones, and therefore causes positive reactivity insertion. When the mixture rises in the zone containing the lower fuel element upper boron endcap and upper fuel elements lower boron endcaps, there is a small amount of negative reactivity inserted into core. At time 0.20 seconds the mixture front starts to rise between the upper fuel elements and eventually within the fuel elements. At that time a large amount of positive reactivity insertion makes the reactor super prompt critical. At time 0.225 seconds the mixture front reaches the top of the upper fuel element and starts to progress through the upper plenum. As happens for the initial phase of the transient, the light water in the moderator acts as an absorber, and reactivity starts to decrease. However that negative reactivity insertion is not sufficient to slow down the transient.

As can be seen in Figure 4.7, at time=0.4 second the mixture front rises only 80 cm from the bottom of the reactor vessel in the central zone. When it rises further, additional negative reactivity insertion results. In order to evaluate that effect, an additional static calculation for the case with the central hole fully occupied by mixture was performed; the static eigenvalue was found to be 1.00931. This indicates that from time 0.4 to 2.25 seconds (when the water mixture reaches the top of the vessel in the central hole) there would be approximately -350 pcm reactivity insertion into core.

Table 4.7 shows the values of various quantities of interest for the different calculation schemes. The point-kinetics approximation is not capable of handling the transient accurately. As can be seen from Figures 4.8 and 4.9 reactivity is overestimated resulting in an early scram time and lower predicted energy accumulations. The adiabatic model with precalculated flux shapes is much better than the point kinetics model. Especially for the first half of the transient, the reactivity predicted by the adiabatic model is in good agreement with that predicted by the reference space-time model. The initial portion of Figure 4.8 also indicates that the use of more state points for the precalculated reactivity curve (as well as flux shape functions) may increase the accuracy of the adiabatic model for that part of the transient. For the second half of the transient, the super prompt critical part, differences between the reference and precalculated adiabatic flux shapes affect the scram time and integrated power. As a result of the earlier scram time, the reactor power is 17% underestimated and the

Table 4.7: Predictions by various models of parameters of interest at the time of 15% overpower scram for the light water ingress of three-element ANS core

Method	Scram-Time (sec)	Reactor Power at the time of scram (MW)	Integrated Power at the time of scram (MJ)	Highest Powered Node Energy Accumulation (MJ)
Few-Group Nodal (Space-Time)	0.227	489.30	76.38	7.14
Point Kinetics	0.212	382.03	70.10	6.54
Adiabatic with Changing Flux Shape	0.220	402.73	72.65	6.80
Adiabatic with Initial Flux Shape	0.220	380.22	72.02	6.72

integrated power is 5% underestimated.

Tables 4.8 and 4.9 show the pseudo-static eigenvalues found from ZAQ and TWODANT throughout the transient for the various calculational procedures. The first columns display the pseudo-critical eigenvalue for the reference space-time solution. With only few exceptions, the λ_{ps} differ from unity in the fifth decimal digit for both solutions. The up to 23 pcm deviations from unity at times between 0.182 and 0.225 seconds come, we believe, from nodal parameter interpolation errors. Notice that these are the time steps where the slope of the reactivity curve is large, and small errors in the cross sections and discontinuity factors can result in relatively large errors in reactivity and eigenvalue. Errors in nodal parameter interpolations can be avoided by using smaller time steps. However the transient develops very quickly, while the delayed precursor concentrations change very slowly. Because of the single precision accuracy used in the nodal code ZAQ, further reduction in time-step size causes round off error accumulation on the delayed precursor concentrations. As a result, in terms of accuracy there is no advantage in using smaller time steps.

The second and third columns with ω_g's or ω_d's set to zero show the sensitivity of the pseudo-critical eigenvalue to these instantaneous periods. For that portion of the transient during which the water mixture is rising in the central region, the flux omegas dominate, whereas for the second half of the transient delayed precursor omegas are as important in the

Table 4.8: The two-group ZAQ solution pseudo-static eigenvalues for the light water ingress event

Time (sec)	Space Time			Point Kinetics	Adiabatic Ch. Flux[1]	Adiabatic Ini. Flux[2]
	Reference	$\omega_g=0$	$\omega_d=0$			
0.100	0.99995	0.99992	0.99999	0.99999	1.00033	1.00031
0.167	0.99996	0.99961	0.99971	0.99987	1.00023	1.00027
0.182	0.99998	1.00108	0.99988	0.99916	0.99988	1.00025
0.197	1.00003	1.00192	1.00021	0.99837	1.00035	1.00033
0.215	1.00017	1.00770	1.00127	0.99889	1.00116	1.00127
0.225	1.00013	1.01098	1.00212	0.99953	1.00220	1.00217
0.400	1.00002	1.00681	1.00619	0.99870	1.00111	1.00110

(1) Adiabatic approximation with changing flux shape
(2) Adiabatic approximation with initial flux shape

Table 4.9: The eight-group TWODANT solution pseudo-static eigenvalues for the light water ingress event

Time (sec)	Space -Time			Point Kinetics	Adiabatic Ch. Flux[1]
	Reference	$\omega_g=0$	$\omega_d=0$		
0.100	0.99998	0.99993	1.00002	0.99999	1.00032
0.167	0.99992	0.99958	0.99960	0.99984	1.00028
0.182	0.99979	1.00089	0.99970	0.99897	0.99970
0.197	1.00014	1.00203	1.00027	0.99843	1.00040
0.215	1.00015	1.00767	1.00129	0.99890	1.00115
0.225	1.00023	1.01105	1.00222	0.99963	1.00225
0.400	0.99999	1.00670	1.00616	0.99868	1.00107

(1) Adiabatic approximation with changing flux shapes

determination of the λ_{ps} as their flux counterparts.

When the point kinetics or adiabatic approximations are used, the resultant λ_{ps} differ from unity in the forth decimal place at the beginning of the transient, and in the third decimal place for later phases. These suggest that the point kinetics model is not capable of modelling the transient accurately. The adiabatic approximation appears to be more accurate, at least for the portion of the transient that is not super-prompt critical.

As a final test, transient flux shapes were compared to the flux shapes found from the TWODANT pseudo-static solution using the reference ω_g and ω_d values. Table 4.10 gives the maximum relative differences in *normalized* nodal flux shapes (normalized to unity) in the central core region for the three different models. The pointwise error bounds for the space-time and adiabatic models at 0.215 seconds are presented in Figure 4.10. For the space-time model, as observed with the fast rod removal transient, flux shapes differ slightly in the outer reflector region, especially for the fast group. (Figure 3.5 shows that the fast group flux is very low in the outer reflector region.) However, the error in the flux shapes for the adiabatic approximation is much larger in the reflector. In addition to that, there are some other differences in the central core region.

Table 4.10: Maximum relative differences in the flux shapes between the reference pseudo-static (TWODANT) and various transient models for the light water ingress event for the central core (fuel elements and their nearest neighbors)

Maximum Error in the flux shape (%)*						
	Space -Time		Adiabatic		Point Kinetics	
Time (sec)	Fast Group	Thermal Group	Fast Group	Thermal Group	Fast Group	Thermal Group
0.100	0.3	0.3	0.9	0.8	0.1	0.4
0.167	0.3	0.4	0.3	1.1	8.1	10.5
0.182	0.2	0.6	1.1	2.1	9.2	17.7
0.197	0.2	0.5	1.0	1.4	10.9	21.2
0.215	0.1	0.6	4.3	4.0	11.5	29.7
0.225	0.2	0.6	6.3	5.9	13.8	34.5
0.400	0.3	0.3	4.3	4.0	14.5	33.8

(*) Error(%)=(Shape(Model)-Shape(Reference))/Shape(Reference)x100

4.5 Discussion and Summary

In this chapter the pseudo-static eigenvalue and flux shape tests were applied to several reactivity transients of the three-element ANS core. Results of the control rod withdrawal

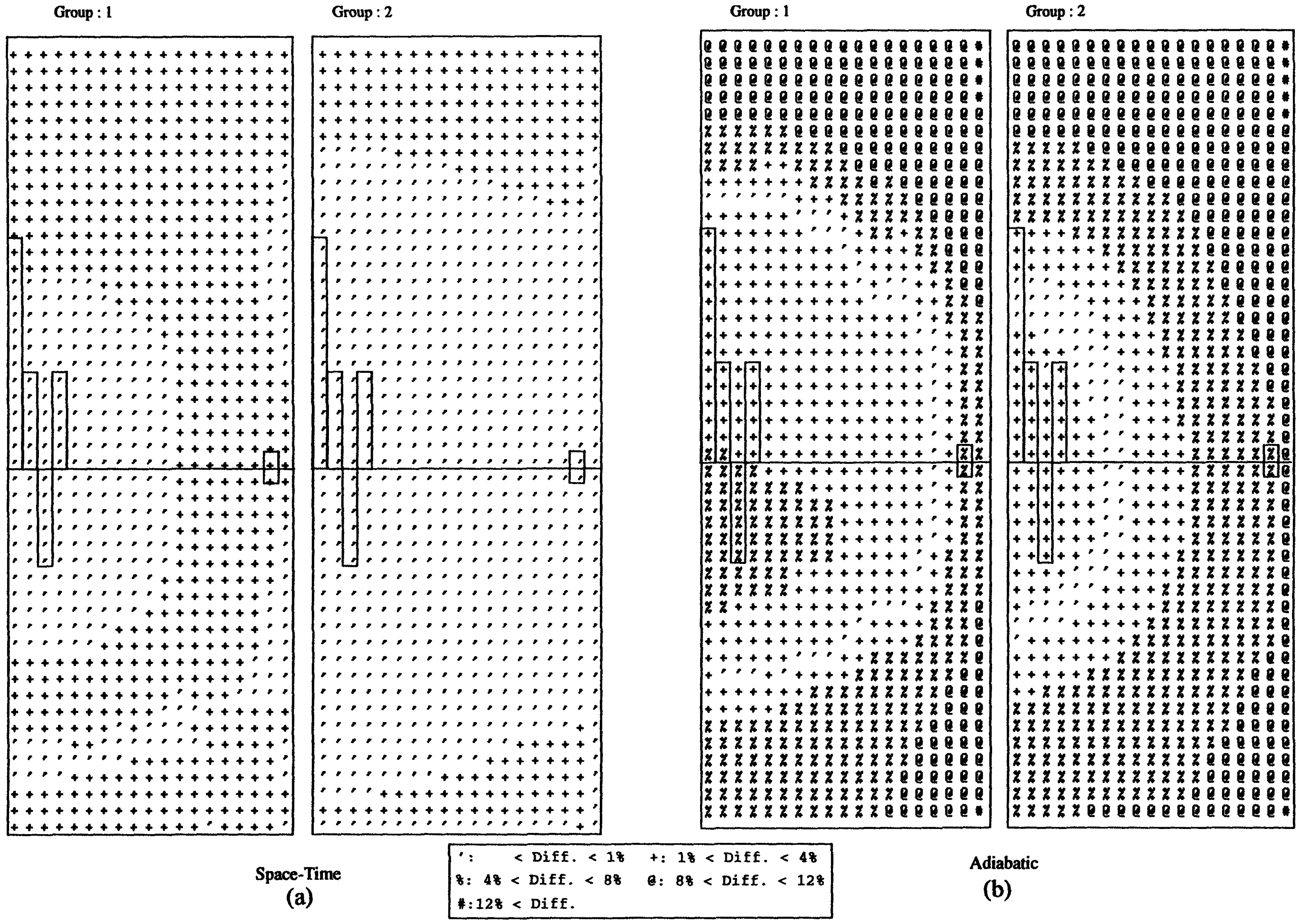

Figure 4.10: Differences at 0.215 seconds between the TWODANT pseudo-static (using reference ω_g and ω_d's) and (a) the space-time and (b) the adiabatic flux shapes for the light water ingress event

transients for the two-element core are given in Appendix A-2. Several conclusions were drawn from these results.

It was found that, for all transients, regardless of the magnitude and the speed of introduction of reactivity, the pseudo-static eigenvalues for the few-group nodal model have a unity value within roundoff. It was also found that the space-time transient flux shapes match both the diffusion and transport theory pseudo-static flux shapes very closely. We conclude that, if a time dependent, multigroup transport problem could be run, results for the prediction of kinetic behavior of the reactor would be close to those predicted by the transient, few-group nodal model.

Comparisons of reactivity and power level predictions by the point reactor model with those found from the space-time solution, as well as the results of pseudo-static test, indicated that the point kinetics model is a poor approximation for all transients analyzed other than the very early time in transients where the flux shape doesn't change much.

On the other hand, an adiabatic model was found to be superior to the point kinetics model especially for slow transients. For the fast control rod removal transient, although the pseudo-static eigenvalue test results were not sufficient to reach any conclusion, the pseudo-static flux shape tests showed that the adiabatic approximation may not be accurate enough. Finally, examination of a light water ingress event, which is a super-prompt critical transient, indicated that the adiabatic model becomes poorer as the transient becomes faster. In this transient, the pseudo-static test indicated significant differences in both eigenvalue and flux shapes.

Since the results presented in this chapter was obtained without any feedback effects, they are unrealistic from a physical point of view. However, this lack of feedback permits applying the indirect validation procedure and, therefore, distinguishing between situations where the space-time model description is intrinsically accurate and where the approximate methods are poor.

In the next chapter, for more realistic simulations, we shall incorporate a simple feedback model for the ANS transients and then reevaluate the transients with feedback.

Chapter 5

Transients with Temperature Feedback

5.1 Introduction

In the previous chapter, various reactivity transients for the three-element ANS core were analyzed and indirect pseudo-static tests were applied to test the accuracy of different transient models. Since no temperature feedback was included in these analyses, the results obtained for the behavior of the ANS were not realistic. In this chapter, a simple thermal feedback model will be introduced for transient analysis. It should be noted that, as with its neutronic characteristics, thermal-hydraulic characteristics of the ANS differ from those of other operating reactors. Accurate analysis requires thermal-hydraulic and feedback models with different emphases. On the other hand, since our primary purpose is to compare various transient models rather than to perform design or safety studies of the ANS reactor, no further feedback model development was undertaken.

One other issue related to feedback is the extension of the pseudo-static test to the multigroup transport solution. Although, theoretically this extension is possible, in practice it is impractical. If a thermal feedback model was incorporated into the analysis, temperature distributions in the core would not be uniform. Almost every fuel and coolant node would have different temperatures. For the pseudo-static transport problems, microscopic cross sections for a given temperature would have to be supplied. Generation of these microscopic cross sections at different temperatures is not possible practically. For this reason pseudo-static tests were applied using only the pseudo-static diffusion model. The fact that, the values of pseudo-static eigenvalues presented in the previous chapter for both the nodal and transport models agreed with each other justifies testing the validity of the point and adiabatic models using the nodal code alone.

In the subsequent sections, first, the thermal-hydraulic features of the ANS reactor will be summarized, then, the feedback model used in the analysis will be outlined. Finally, transients discussed in the previous chapter will be reevaluated in the presence of the temperature feedback.

5.2 Thermal-Hydraulic Features of the ANS Reactor

In this section, we summarize the very basic features of the ANS thermal-hydraulics. For design details, the reader is advised to consult references [R-1, Y-2].

As mentioned before, the ANS reactor is designed to provide experimental capability over in a wide range of conditions. To achieve that objective, the reactor design uses highly subcooled heavy water as both coolant and moderator. The three-split core of 79.3 L total volume operates at an average power density of ~4.0 MW/L. This power density is well above that of typical LWR reactors. (For PWRs, the power density is around 100 kW/L.) The coolant flows upward through the core at 20 m/sec. Operating pressure is 2.7 MPa at the core inlet with a 0.9 MPa pressure drop through the core region. The coolant core inlet temperature is 45°C. The bulk outlet coolant temperature of 80°C is maintained below 100°C to avoid steam flashing in the event of rapid core depressurization. The ANS reactor core is constructed with a series of involute fuel plates. A fuel plate is illustrated in Figure 5.1 along with the simple model used in our calculations. The thin fuel is 1.27 mm thick and consists of 0.254 mm thick Aluminum 6061 cladding material sandwiching a 0.762 mm mixture of uranium silicide fuel (U_3Si_2) and aluminum. Each coolant gap is 1.27 mm in thickness and 77.65, 63.95 and 55.41 mm (the inner, middle and outer fuel elements respectively) in width. In spite of the high

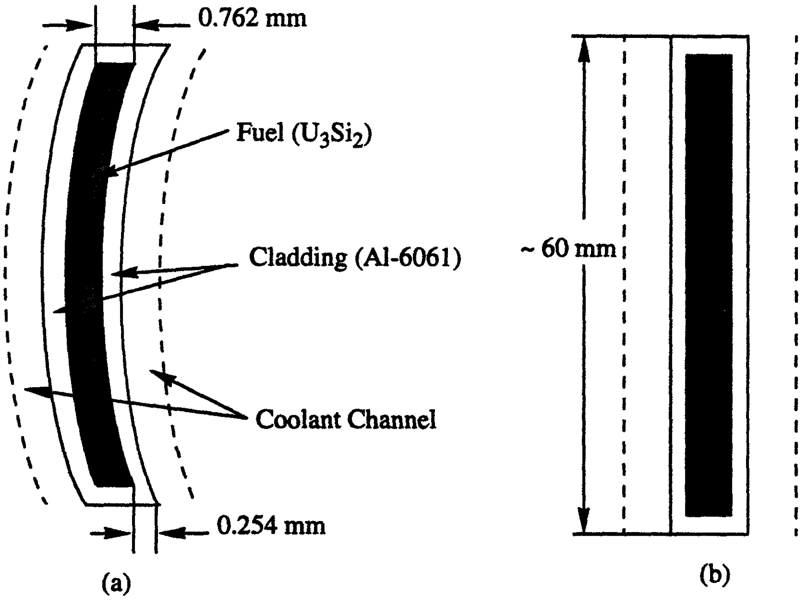

Figure 5.1: Involute fuel plate of the ANS

power density, the use of thin fuel plates and fuel and cladding materials having high thermal conductivities allows safe operation below the fuel temperature limit (400°C).

5.3 The Thermal Feedback Model

In this section, we describe the thermal feedback model and then summarize the assumptions made in calculations.

5.3.1 The WIGL Model

The thermal feedback model of the nodal code ZAQ was developed primarily for gas cooled, graphite moderated reactors [B-2]. The heat transfer mechanism of the ANS, being close to that of a water moderated and cooled system, differs significantly from that of gas cooled reactors. For that reason, a different, simple model was incorporated for the ANS transient analysis. A lumped heat capacity model, the WIGL model [V-1], has been used in many codes to simulate the thermal feedback effects [G-2, S-1]. Accordingly, in this study, it was implemented in ZAQ. In this model, the material properties are assumed to be constant. The primary quantities of interest in the WIGL model are the average fuel temperature, the average coolant temperature, and the average coolant density in a node. The following equations are obtained by performing a time dependent energy balance on the fuel and the coolant in node *(i,k)* with the assumption that *no boiling* occurs and mass flow rate is constant

$$\rho_f V_f^{ik} C_f \frac{dT_f^{ik}}{dt} = (1-r)\,(q''')^{ik} V_f^{ik} + V_c^{ik}\left[\frac{1}{A_H U} + \frac{1}{A_H h_0}\right]^{-1}\left(T_f^{ik} - T_c^{ik}\right) \tag{5.1}$$

$$\begin{aligned} V_c^{ik}\left(\frac{\partial \rho_c H}{\partial T_c}\right)\frac{dT_c^{ik}}{dt} &= V_c^{ik}\left[\frac{1}{A_H U} + \frac{1}{A_H h_0}\right]^{-1}\left(T_f^{ik} - T_c^{ik}\right) \\ &\quad + 2W_r^{ik} C_c\left(T_b^{ik} - T_c^{ik}\right) + r(q''')^{ik} V_f^{ik} \end{aligned} \tag{5.2}$$

$$T_b^{ik} = 2T_c^{ik} - T_b^{i,k-1} \tag{5.3}$$

where, subscripts *f*, *c* and *b* indexing the fuel, coolant and coolant inlet respectively, and

T^{ik} = average temperature in node *(i,k)*,

ρ = density,

C = specific heat,

r = fraction of fission power deposited directly into the coolant,

$(q''')^{ik}$ = volumetric energy generation rate in node *(i,k)*,

V = volume,

A_h = total heat transfer area/coolant volume within a node,

h_0 = convective heat transfer coefficient at initial flow rate,

W_{ik} = coolant mass flow rate in node *(i,k)*,

U = fuel element heat transfer coefficient,

$\left(\frac{\partial \rho_c H}{\partial T_c}\right)$=energy required to raise the temperature of a unit volume of coolant one temperature unit.

For the ANS applications, the equations given above are solved only for the central core region (fuel elements and coolant channels between the fuel elements) using a fully implicit time integration method with the same time step that is used for the neutronic calculations. Following the calculation of the average fuel and coolant temperatures, the coolant density is found using steam tables.

As shown in Figure 5.1, the fuel plate consists of two regions, a fuel meat and clad. It was lumped into one element using the steady-state temperature distributions to determine the average plate temperature at the advanced time [M-3]. Details of this model and other correlations used for the heat transfer coefficients are given in Appendix-C.

5.3.2 Cross Section Feedback Model

Two feedback mechanisms due to fuel temperature (Doppler) and coolant density changes have been considered for the ANS transient analysis.

The fuel temperature coefficient, α_T^F, and cross section derivatives with respect to fuel temperature $(\partial\Sigma_\alpha/\partial T_f)$ for each fueled node were found by running full core TWODANT cases using cross section libraries at fuel temperatures of 350 and 550K (k_{eff}=1.08288 at T_{fuel}=350K and k_{eff}=1.08024 at T_{fuel}=550K yield α_T^F=-1.225 pcm/K).

The coolant density feedback coefficient, α_d^C, and the density derivatives of the cross sections $(\partial\Sigma_\alpha/\partial d_c)$ were found by changing the coolant density in central core region to its 95% nominal value and using the cross section libraries at fuel temperature of 350K for both cases (k_{eff}=1.08288 at *100%* ρ_c and k_{eff}=1.07627 at *95%* ρ_c). For these calculations the tips of the central control rods were located at the core mid plane.

For the space-time and point kinetics models, cross section sets were modified by assuming that all cross sections and inverse diffusion coefficients are linear functions of the node average fuel temperature and coolant density. Thus, for a given fuel temperature, T_f, and coolant density, d_c, cross sections are found from

$$\Sigma_\alpha(T_f, d_c) = \Sigma_\alpha(T_{f0}, d_{c0}) + \frac{\partial\Sigma_\alpha}{\partial T_f}(T_f - T_{f0}) + \frac{\partial\Sigma_\alpha}{\partial d_c}(d_c - d_{c0}) \qquad (5.4)$$

where T_{f0} and d_{c0} are the reference fuel temperature and coolant density.

For the adiabatic model, feedback reactivity was calculated using the flux-weighted core-average temperatures, coolant density and the reactivity temperature coefficients. Thus, the feedback reactivity, $\Delta\rho$, is,

$$\Delta\rho = \alpha_T^F(T_f - T_{f0}) + \alpha_d^C\left(\bar{d}_c - \bar{d}_{c0}\right). \qquad (5.5)$$

5.3.3 Assumptions

The assumptions made in the feedback model can be summarized as follows:

- Since the feedback effects from coolant temperature changes at constant density are smaller than the density effects at constant temperature, only density feedback effects were modelled.

- It has been assumed that, throughout all transients, no boiling takes place in the coolant. As has been noted, the reactor is designed to operate in a highly subcooled region. However during transients, the cladding wall temperature may exceed the coolant saturation temperature and subcooled boiling may take place. Notice that, there is also a large pressure drop in the core that should be taken into account. The heat transfer mechanisms at high heat flux conditions are being investigated by various research groups including the ANS design team. For actual design calculations more accurate models that include those features should be used.

- Although it may be important for the super-prompt critical cases, core expansions were neglected.
- The gamma heating and energy transfer to the D_2O reflector tank was neglected. During the normal operation 5% of the heat generated in the core is transferred in to the reflector tank. Because of the large heat capacity of the reflector tank, for fast transients, temperature changes are negligible.
- It was assumed that 3% of the fission power is liberated in the central core coolant region.
- For all transients, fresh core and normal (nonsegregated) fuel properties were used. (Most of the fuel and cladding thermal properties change with burnup significantly.)
- For the adiabatic model, flux shapes were calculated without feedback, and transients were run by using these precalculated flux shapes assuming that those shapes are not affected by the temperature profile.

5.4 Reactivity Transients with Thermal Feedback

In this section, results of the previously described three transients, slow and fast rod removals and a light water ingress event, are presented.

5.4.1 The 10 second control rod withdrawal transient

In this slow transient, one of the three central control rods is withdrawn in 10.0 seconds. The same time step size of 0.05 seconds has been used. Figures 5.2 and 5.3 show the resultant power level and reactivity behavior. Since the transient is slow, with the temperature feedback power increment is limited significantly (see Figure 4.3 for the case without feedback). As can be seen from the reactivity plot, after 5 seconds, reactivity starts to decrease before reaching its super-prompt critical value. The power and reactivity predictions by the adiabatic model are again very close to those of the space-time model. The use of core average (flux-weighted) temperatures with reactivity coefficients to calculate the feedback reactivity seems to work well for the adiabatic model. (The use of other weighted temperatures, such as volume-weighted or power-weighted, may increase the accuracy further.)

The results of the pseudo-static test presented in Table 5.1 are very similar to those

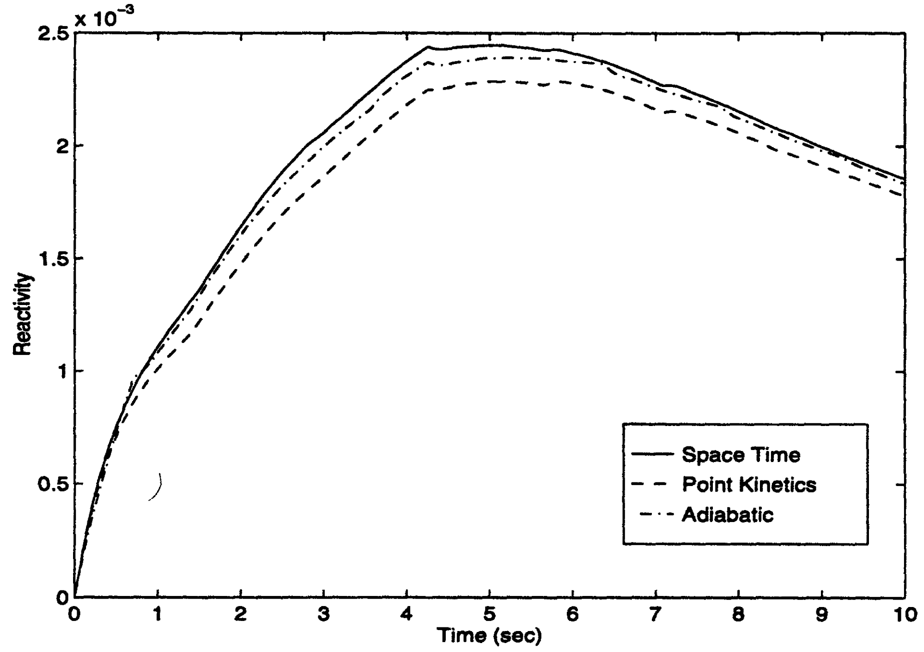

Figure 5.2: Reactivity vs. time for the 10 second rod withdrawal transient with thermal feedback

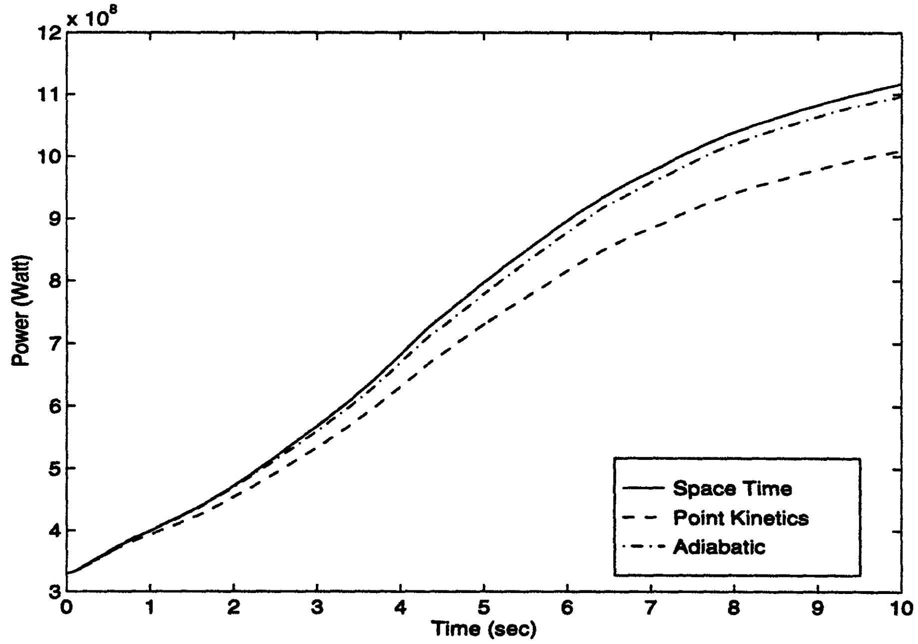

Figure 5.3: Power vs. time for the 10 second rod withdrawal transient with thermal feedback

obtained for the non-feedback case. For both the space-time and adiabatic models the pseudo-static eigenvalues deviate from unity in the fifth decimal digit whereas for the point kinetics model deviations are as much as 100 pcm.

Table 5.1: The two-group ZAQ solution pseudo-static eigenvalues for the 10 seconds rod withdrawal transient with thermal feedback

Time (sec)	Space Time	Point Kinetics	Adiabatic Approximation[1]
0.50	1.00002	1.00008	1.00006
1.25	1.00001	1.00020	1.00003
2.50	1.00001	1.00038	1.00005
5.00	1.00000	1.00070	1.00001
7.50	1.00000	1.00094	0.99998
10.00	1.00000	1.00106	0.99998

(1) Adiabatic approximation with changing flux shapes

5.4.2 The 0.1 second control rod withdrawal transient

Figures 5.4 and 5.5 are analogous to 5.2 and 5.3 respectively. For this 0.1 second rod withdrawal transient, in order to see the effect of thermal feedback, simulation time was extended to 10 seconds. To reduce the running time, after 1.0 second into the transient, 0.05 second time steps were employed. In terms of reactivity prediction the adiabatic model gives excellent results. The prediction of the core (volume) average fuel and coolant temperatures by the three different models are given in Figure 5.6. Notice that as a result of large heat transfer coefficient and high thermal conductivities of both the fuel and cladding (resulting in a time constant of ~0.02 sec. for the fuel plate) there is a significant amount of energy transferred to the coolant within a short time. Hence in addition to the Doppler feedback, the coolant density changes also slows down the transient. In terms of core average temperatures, the adiabatic approximation is much better than the point kinetics model.

Table 5.2 gives the results of the pseudo-static test. It is interesting to note that with the thermal feedback adiabatic approximation results seem to be improved, especially for the later

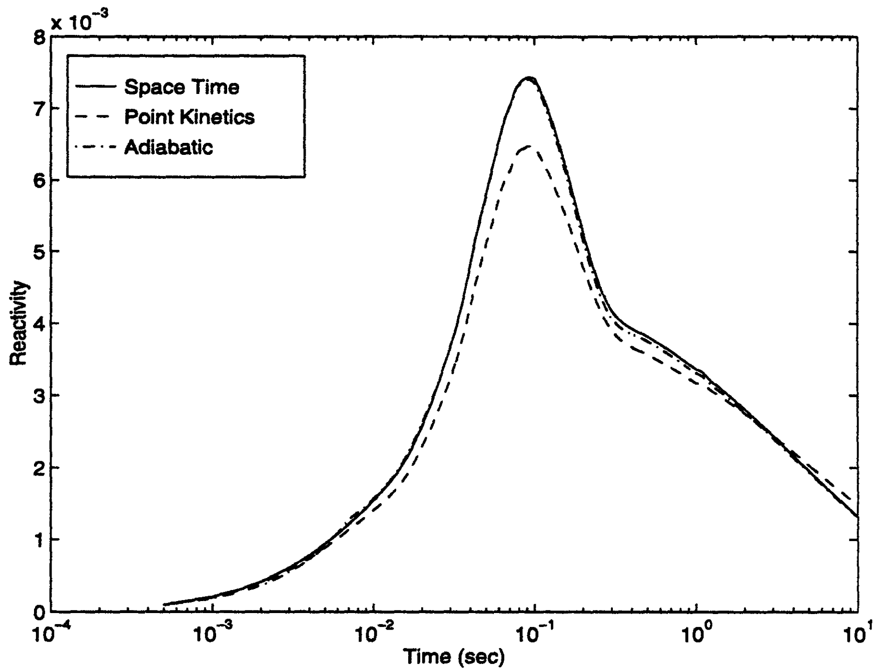

Figure 5.4: Reactivity vs. time for the 0.1 second rod withdrawal transient with thermal feedback

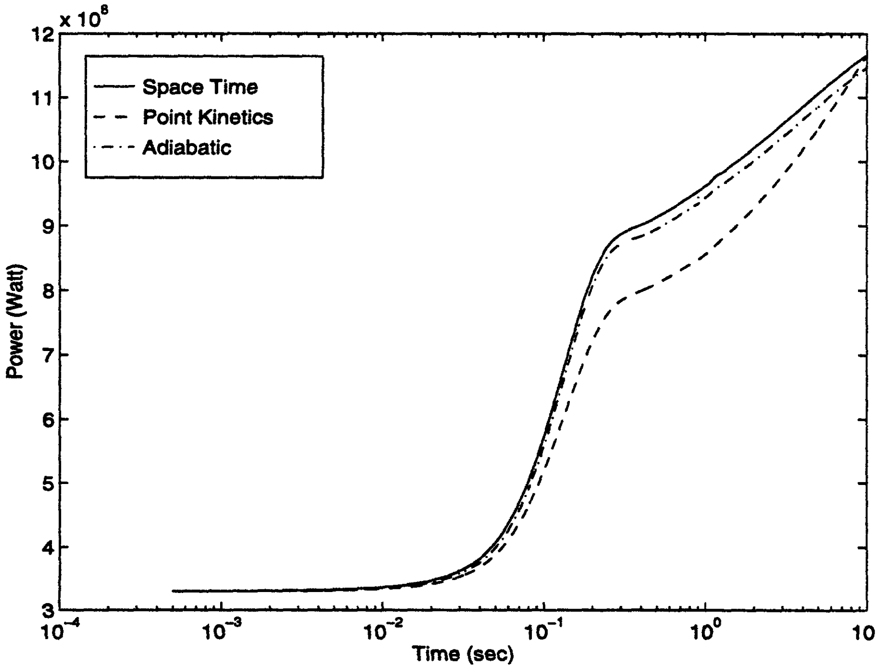

Figure 5.5: Power vs. time for the 0.1 second rod withdrawal transient with thermal feedback

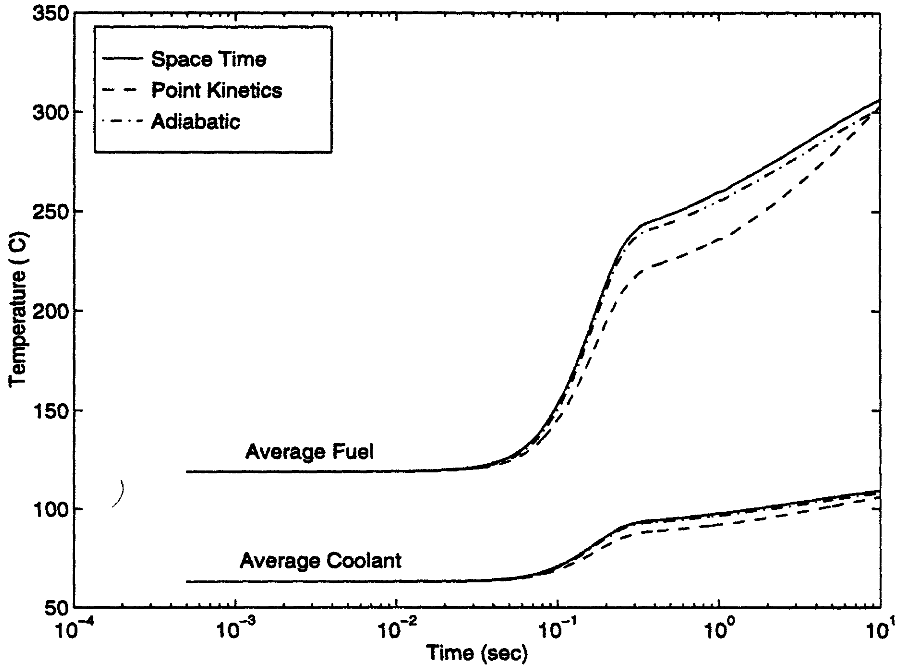

Figure 5.6: Core average fuel and coolant temperatures vs. time for the 0.1 seconds rod withdrawal transient

Table 5.2: The two-group ZAQ solution pseudo-static eigenvalues for the 0. 1 seconds rod withdrawal transient with thermal feedback

Time (sec)	Space Time	Point Kinetics	Adiabatic Approximation[1]
0.0050	1.00009	1.00011	1.00011
0.0125	1.00001	1.00020	1.00011
0.0250	1.00002	1.00050	1.00037
0.0500	1.00014	1.00088	1.00041
0.0750	1.00002	1.00115	1.00036
0.1000	1.00001	1.00128	1.00032
0.2000	0.99999	1.00115	1.00018
7.0000	1.00000	0.99985	1.00002

(1) Adiabatic approximation with changing flux shapes

phases of the transient. As has already been stated, for the adiabatic model both simulations with and without feedback use the same shape functions to reconstruct the time dependent fluxes. In Figure 5.7, the adiabatic flux shape at time 0.2 second is compared with those found from the space-time solution with and without feedback. (Although control rod reached its fully withdrawn position at 0.1 seconds, the space-time flux shape has not yet reached its asymptotic shape.) An examination of these results reveals that the adiabatic flux shape matches the space-time flux shape with feedback closely. As the core heats up, because of reduced thermalization in the coolant/moderator and increased resonance capture in the fuel, the flux level in the central core decreases relative to that in the D_2O reflector tank. As a result of this new flux shape, the adiabatic approximation accuracy improves and the pseudo-static test yields eigenvalues close to unity.

5.4.3 The light water ingress event

Figures 5.8 and 5.9 show the effect of the reactor power and change in reactivity for the light water ingress event. During that phase of the transient when the heavy water-light water mixture is rising between the upper fuel elements, positive reactivity insertion takes place in a step fashion so that the reactor first becomes super-prompt critical. Then the Doppler and the coolant density feedbacks slow down the reactor runaway. In the point kinetics models initial reactivity is overestimated. The power then increases rapidly resulting a large increase in the temperatures which, in turn, gives a low value for the reactivity for later phases. The underpredicted reactivity by the adiabatic model at around 0.2 seconds approaches the space-time model prediction as the transients progresses. Figure 5.9 indicates that the adiabatic model is not as good in the prediction of power as in the previous cases. But the comparison of nonfeedback (see Figure 4.9) and feedback cases shows that the error (~25% adiabatic vs. space-time) in the reactor power at 0.4 seconds reduces to ~7%.

Table 5.3 summarizes the results from the pseudo-static tests. Again, the use of omega values found from the reference space-time solution yields pseudo-static eigenvalues close to unity within uncertainty. The results for the point kinetics and adiabatic models show trends similar to the non-feedback cases except that as the core temperature increases, the pseudo-static eigenvalue of the adiabatic approximation gets closer to unity, as was observed in the fast rod removal transient.

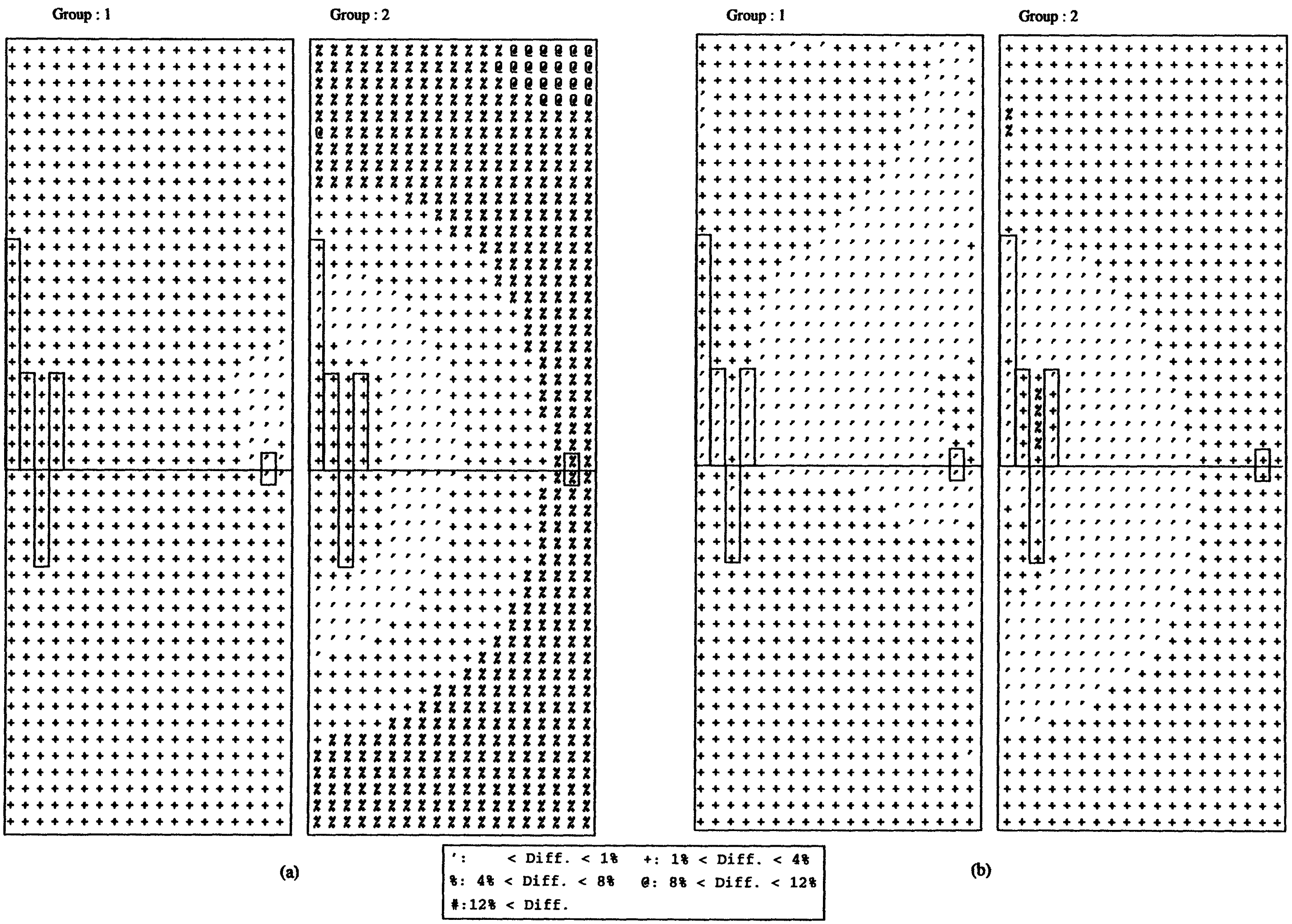

Figure 5.7: Differences in the flux shapes at 0.2 seconds between the asymptotic and (a) the space-time without feedback and (b) the space-time with feedback for the 0.1 second rod removal transient

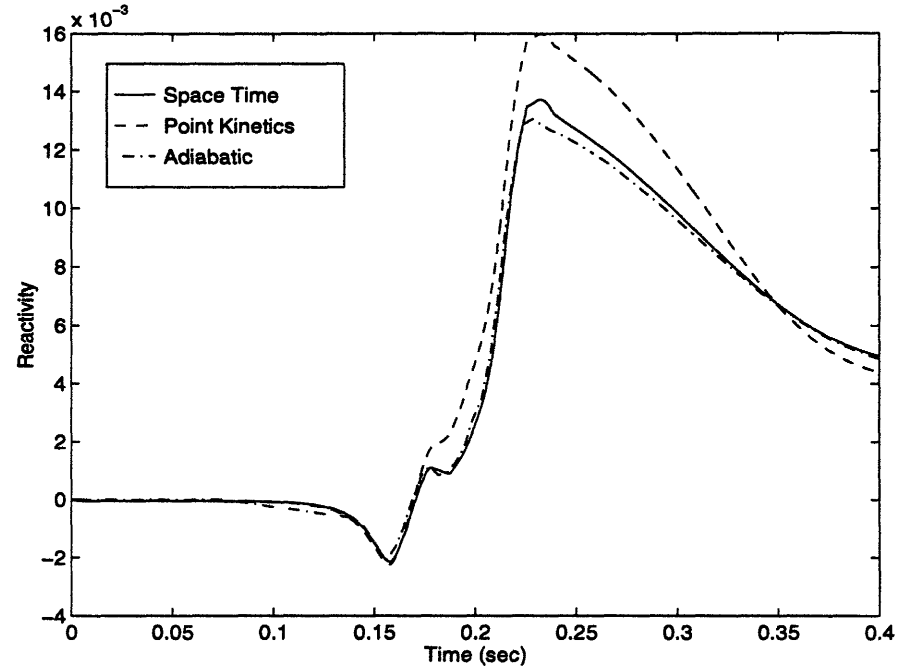

Figure 5.8: Reactivity vs. time for the light water ingress event with thermal feedback

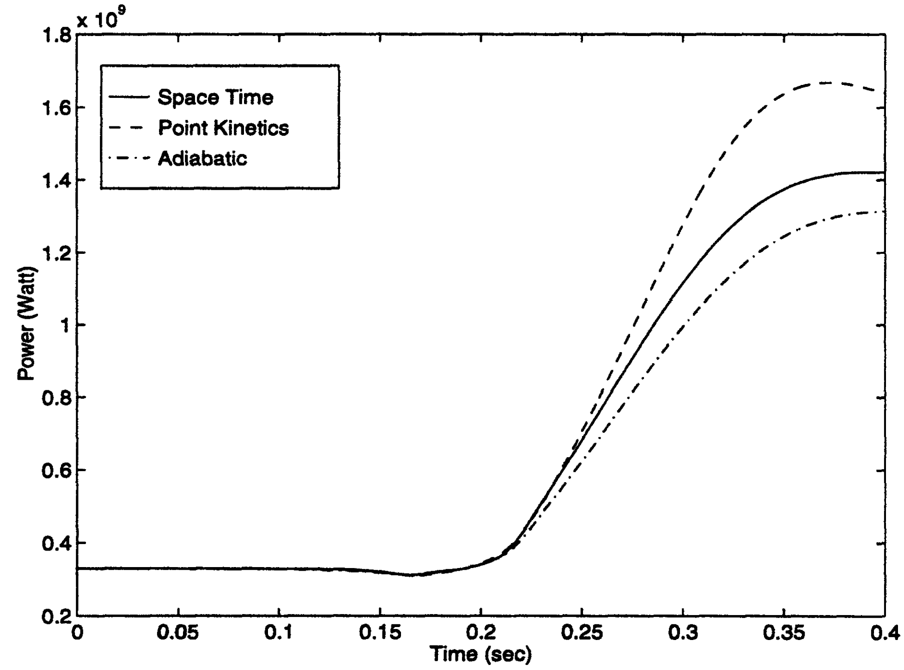

Figure 5.9: Power vs. time for the light water ingress event with thermal feedback

Table 5.3: The two-group ZAQ solution pseudo-static eigenvalues for the light water ingress event with thermal feedback

Time (sec)	Space Time	Point Kinetics	Adiabatic Approximation[1]
0.100	1.00000	1.00001	1.00014
0.167	1.00005	0.99986	0.99994
0.182	0.99995	0.99908	1.00023
0.197	1.00002	0.99822	1.00022
0.215	1.00020	0.99875	1.00062
0.225	1.00012	0.99949	1.00229
0.400	1.00000	0.99786	1.00011

(1) Adiabatic approximation with changing flux shapes

5.5 Summary

In this chapter, we introduced a simple feedback model for the transient analysis of the ANS reactor. Using that model, previously described reactivity transients were analyzed. Generally, the same trends were observed. In all transients the point-kinetics model seems to be a poor approximation. When feedback effects are included in a model, they make the transients less severe since the amount and the speed of reactivity insertion is limited. Results show that the flux shapes found from the static λ-modes represent the true space-time shape much better. This does not imply that for every transient the accuracy of the adiabatic approximation improves. However, pseudo-static test methods can be applied to measure that accuracy. It is also apparent that as the time scale of the transient gets smaller a space-time model may be needed for accurate simulations.

Although, the results presented in this chapter are more realistic than those given in the previous chapter (non-feedback cases), actual safety and design calculations may require the use of more elaborate models. In addition to improvements in the heat transfer model (resolution of spatial temperature profile in a fuel element, two-phase heat transfer etc.), a hydraulic model should be included in simulations. Also instead of using one or two cross section modification sets for temperature feedback, a table look-up or polynomial fitting procedures should be used to obtain a more accurate cross section representation.

Chapter 6

Conclusions and Recommendations

6.1 Overview of the Investigation and Conclusions

The objective of this study was the development of a procedure which can be used to validate a space-time nodal model as well as any other approximate method for the transient analysis of tightly coupled reactors.

In Chapter 2, the nodal diffusion theory model taking into account transport corrections was reviewed. The components of that model were presented: First the steady-state finite difference equations were derived; then the use of the Monte Carlo and discrete ordinate procedures to obtain the nodal parameters appearing in the nodal equations was discussed. Finally three different transient models (point-kinetics, adiabatic and space-time) used in the remaining portion of the dissertation were outlined.

In Chapter 3, an indirect test for the validation of a few-group, time-dependent nodal model for transient analysis of tightly coupled reactors was developed. First, pseudo-static equations were derived starting from the time-dependent diffusion and time-dependent transport equations. Next calculational steps were presented. The validation is based on the fact that at any stage during a transient calculation, the transient equations can be converted to a static eigenvalue problem by introducing group-flux and delayed precursor "frequencies". These time constants can be edited at any time-step from the transient analyzed. A test of whether the nodal transient calculation would agree with a transient transport calculation is then to see if the dynamic frequencies when inserted into the time-dependent equation will yield an eigenvalue of unity. The crucial part of the validation procedure is the expansion of the few-group omegas to multigroup omegas. Since there is no theoretical basis for that expansion, numerical studies were conducted to examine the nature of the flux and delayed precursor omegas. It was found that for all transients analyzed, few-group values of the delayed precursor omegas can be used for multigroup values. It was also shown that by choosing properly the thermal cut off of the two-group scheme, two-group values can be expanded to multigroup quite accurately. In addition to the energy-group expansion, we investigated the angular dependency of the flux omegas, and argued that they do not play a significant role in the determination of the pseudo-static eigenvalue. Finally, for each case analyzed, the sensitivity of the pseudo-static eigenvalue to flux and delayed precursor omegas was examined.

Applications of the indirect validation test were presented in Chapter 4. Various reactivity transients for the three-element ANS core were analyzed by the three different transient models without feedback. (Similar tests were also performed for the two-element core control rod withdrawal transients.) The lack of feedback in the model permitted applying the indirect validation procedure and distinguishing between situations where the space-time model is accurate and where the approximate methods are poor. For all transients analyzed, regardless of the magnitude and the rate of introduction of reactivity, it was found that the pseudo-static eigenvalue of the space-time model had a value of unity within roundoff and that the space-time flux shapes matched both the diffusion and transport model pseudo-static flux shapes very closely. We concluded that, if a time-dependent, multigroup transport problem could be run, results for the prediction of the kinetic behavior of the reactor would be close to those predicted by the transient, few-group nodal model.

When the pseudo-static problems were run using the group-flux and delayed precursor omegas found from the point-kinetics solution, the pseudo-static eigenvalue deviated from unity (depending on the rate and magnitude of the reactivity) by up to the third decimal digit, and transient flux shapes differed from the pseudo-static flux shapes significantly. When similar tests were applied to the adiabatic approximation, for some cases the pseudo-static eigenvalue test itself was not sufficient to reach any definite conclusion (resulting in a deviation from unity of only 40-50 pcm). However pseudo-flux shape tests enabled us to evaluate the accuracy of the model. These results without feedback showed that the point kinetics approximation is poor except at very early times into transients whereas the adiabatic model is quite accurate, especially for the transients which are slow (rate of reactivity insertion is small) and the amount of reactivity insertion is limited (below super prompt critical).

Tests also indicated that for accurate prediction of the kinetic behavior of the ANS reactor by a few-group model, space-dependent group velocities, reduced from multigroup values using the associated spectrum, rather than the core-averaged ones should be used. That conclusion is expected for all reactors in which energy spectrums changes dramatically with position.

In Chapter 5, to provide more realistic simulations, a simple thermal feedback model was introduced for the ANS reactor. The transients examined in Chapter 4 were reevaluated in the presence of temperature feedback. The pseudo-static eigenvalue and flux shapes were also applied to the transients to measure the accuracy of the various models. Results showed that, since the feedback reactivity slows the transient (true if the reactor has negative reactivity coefficients), the accuracy of the adiabatic approximation improves.

By using the validation procedure introduced in this study, the accuracy of any neutronic model for which time-dependent detailed group-flux and delayed precursor distribution information is available, can be tested. Its application is not limited to tightly coupled reactors. However, a conclusion about the absolute accuracy of the transient model of interest can be drawn only if errors due to input data are known. If a certain level of accuracy due to these errors is acceptable, a comparable error due to use of an approximate method may also be acceptable.

6.2 Recommendations for Future Work

It is recommended, for future research, that the following areas be investigated.

6.2.1 Effect of Higher Order Omega Modes in Transients

In Chapter 3, while we were investigating the angular dependency of the flux omegas, it was assumed that there is no directional dependency in the time behavior of the angular fluxes. Our assumption was based on the fact that the higher order energy and angular effects die out very quickly. Intuitively, this is a very reasonable approximation for most transients. However for extremely rapid transients, these neglected higher order terms may start to affect the time behavior.

In the diffusion theory model, the angular distribution of the neutrons is assumed to be, at most, linearly anisotropic. For time-dependent problems except for the P_0 term, time derivatives are neglected ($\partial J/\partial t = 0$). A transient model, in which time derivatives of these higher order terms were not neglected might allow evaluation of the effect of the higher order omega modes. Because of the complexity of developing a time-dependent transport code, a simple one dimensional P_n model (easier to develop than a transient S_n model) in which, for example, time derivatives up to the P_2 term were kept could be used to examine the importance of the higher order omega modes for transient problems.

6.2.2 An Improved Reference Transport Solution

It has been mentioned several times that the interpolated nodal parameters (cross sections and discontinuity factors) are based on static transport eigenvalue calculations. The time-dependent flux and current energy spectra differ from the corresponding static spectrum used to generate the few-group nodal parameters. Even if there is no energy-group collapsing, spatial angular flux shapes and hence scalar flux and current shapes change with transients because of the presence of delayed neutrons. Hence the cross section and discontinuity factor sets found from the static solutions are only approximations. The difference between the approximate and actual sets is very small for most transients. However, for severe transients, where these effects may start to be important, a more accurate reference space-time transport solution could be obtained by iterating between the static transport and time dependent-diffusion codes. Figure 6.1 illustrates how to employ the idea. The iterative procedure described below is an extension of the pseudo-static test developed in this thesis.

The iteration starts with the generation of the cross section and discontinuity factor sets for a small portion of the transient of interest from the static transport calculations. (For example, if the transient is a control rod withdrawal, nodal parameter sets are generated for different control positions in the only first node.) That part of the transient for which nodal parameters have been generated is run by the diffusion transient code using smaller time steps and by table interpolation. (For the accuracy the use of higher order interpolation procedures is recommended. The time step size for both the transport and diffusion calculations can be taken as the same; however that procedure would be extremely expensive.) The flux and precursor omegas are edited from transient results. Next, theoretically more accurate, "corrected" nodal parameters are generated from the pseudo-static transport calculations. Then the transient problem is rerun with these "corrected" nodal parameter sets. The iteration is repeated until some convergence criteria is achieved for the transport and/or diffusion fluxes. The same iteration is performed for consecutive portions of the transient (control rod in

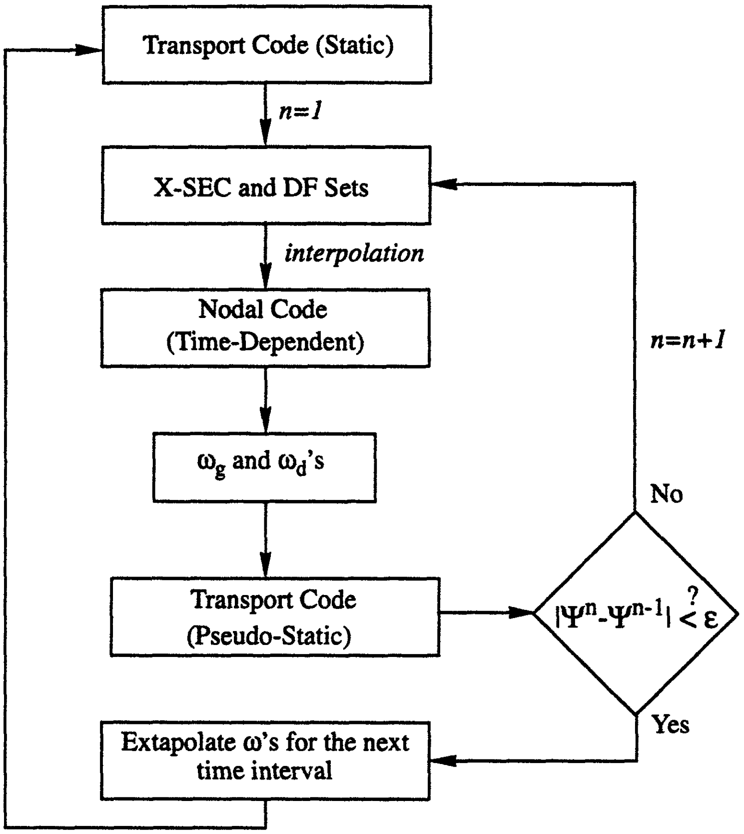

Figure 6.1: Steps for the improved reference transport solution

the second node, and so on). For these portions of the transient, flux and precursor omegas can be expanded from the previous time steps.

Although the procedure described above, should converge to the time-dependent transport solution, because of the nonlinear nature of the iteration, convergence is not guaranteed. Therefore, for such a test problem, a reactor model simpler than the ANS should be chosen. Also the use of same number of energy-groups for both the transport and diffusion problems would prevent uncertainties that might arise from extrapolation of flux omegas if different numbers of energy-groups were used.

To get a preliminary idea for the applicability of iterative procedure, the initial portion of the 0.1 second control rod removal was run using eight energy groups. Table 6.1 shows the transport flux convergence at two different time steps through the transient. Results are promising.

Table 6.1: The Root Mean Square Error in TWODANT transport fluxes between two consecutive iteration steps

Iteration #	RMS Error (%) at t= 0.007 sec	RMS Error (%) at t=0.014 sec
1	0.890%	1.391%
2	0.082%	0.018%
3	0.020%	0.015%

6.2.3 Application to the Other Reactors

The few-group transient nodal model taking into account the transport corrections and the validation procedure developed for tightly coupled reactors were applied only to the ANS reactor. There is a tendency for other tightly coupled reactors to use Monte Carlo methods for the static analysis and the point-kinetics approximation for transient analysis. It would be extremely interesting to test the accuracy of the few-group nodal transient model as well as the other approximate methods which are used for these reactors.

6.2.4 A More Advanced Thermal-Hydraulic Model

For ANS reactor applications, a very simple thermal-hydraulic feedback model was incorporated to test the general feedback response of the transient methods. A more detailed model should be employed for design and safety studies.

References

[A-1] Y. Y. Azmy, F.C. Difilippo, "Comparison of the Diffusion and Transport Calculations for the Advanced Neutron Source Reactor," *Proc. Int. Reactor Physics Conf.*, Vol. II, 183 (1988).

[A-2] Y. Y. Azmy, "Accuracy of Transport Calculations for the Advanced Neutron Source Reactor," *Tran. of Am. Nuc. Soc.*, **57**, 293 (1988).

[A-3] R. E. Alcoufe *et al.*, "User's Guide for TWODANT: A Code Package for Two-Dimensional, Diffusion Accelerated, Neutral-Particle Transport," LA-10049-M, revised (February 1990).

[B-1] J. F. Breismeister (Editor), "MCNP - A General Monte Carlo Code for Neutron and Photon Transport, Version 3A," LA-7396-M, Rev. 2, September 1986, revised (April 1991).

[B-2] M. E. Byers, "A Transient Nodal Method for Reactor Models in R-Z Geometry,", Ph.D. Thesis, Department of Nuclear Engineering, Massachusetts Institute of Technology (September 1992).

[B-3] G. I. Bell and S. Glasstone, "Nuclear Reactor Theory," Robert E. Kriger Publishing Company, NY (1979).

[D-1] F. C. Difilippo, M. Abu-Shehadeh, R. B. Perez, "Two-Point and Two-Energy Group Kinetics Model of the ANS Reactor," *Tran. of Am. Nuc. Soc.*, **59**, 347 (1989).

[G-1] V. T. Gozani, "The Concept of Reactivity and its Application to Kinetics Measurements," *Nukleonik*, **5**, 55 (1963).

[G-2] Jess C. Gehin, "A Quasi-Static Polynomial Nodal Method for Nuclear Reactor Analysis," Ph.D. Thesis, Department of Nuclear Engineering, Massachusetts Institute of Technology (August 1992).

[G-3] J. Gherchanoc, "Supernodal Procedures for Transient Analysis," Report, Department of Nuclear Engineering, Massachusetts Institute of Technology (December 1994).

[G-4] Jess C. Gehin, Oak Ridge National Laboratory, Personal communications (January 1995).

[H-1] A. F. Henry, "Nuclear Reactor Analysis,", MIT Press, Cambridge, MA (1975).

[H-2] A. F. Henry, "Derivation of Nodal Equations Having the Finite-Difference Form," Course Notes, 22.313, Massachusetts Institute of Technology, (Fall 1992).

[H-3] Pavel Hejzlar, "Conceptual Design of a Large, Passive, Pressure Tube Light Water Reactor," Sc.D. Thesis, Department of Nuclear Engineering, Massachusetts Institute of Technology (May 1994).

[H-4] A. F. Henry, "The Application of Reactor Kinetics to the Analysis of Experiments," *Nucl. Sci. Eng.*, **3**, 52 (1958).

[H-5] A. F. Henry, "The Application of Inhour Modes to the Description of Nonseparable Reactor Transients," *Nucl. Sci. Eng.*, **20**, 338 (1964).

[H-6] M. Hayashi *et al.*, "Calculated Energy and Angular Dependence of Particle Fluxes at the Exit of the Advanced Neutron Source Radial and Tangential Beam Tubes," *Nucl. Sci. Eng.*, **109**, 391 (1991).

[L-1] E.E. Lewis, W. F. Miller Jr., "Computational Methods of Neutron Transport," A Wiley-Interscience Publication (1984).

[K-1] M. H. Kim, "The Use of Bilinearly Weighted Cross Sections for Few-Group Transient Analysis," Ph.D. Thesis, Department of Nuclear Engineering, Massachusetts Institute of Technology (June 1988).

[M-1] Amr S. G. Mohamed, "A Transient Nodal Method Accounting for Multigroup Transport Effects," Sc.D. Thesis, Department of Nuclear Engineering, Massachusetts Institute of Technology (February 1994).

[M-2] J. Mika, "The Effect of Delayed Neutrons on the Spectrum of the Transport Operator", *Nukleonik*, **9**, 46 (1967).

[M-3] J.E. Meyer, "Some Physical and Numerical Considerations for the SSC-S Code," BNL-NUREG-50913 (1978).

[O-1] K. O. Ott, D. A. Meneley, "Accuracy of the Quasistatic Treatment of Spatial Reactor Kinetics," *Nucl. Sci. Eng.*, **36**, 402 (1969).

[O-2] K. O. Ott, R. J. Neuhlod, "Nuclear Reactor Dynamics," American Nuclear Society, IL (1985).

[R-1] J. M. Ryskamp *et al.* "Reactor Design of the Advanced Neutron Source," *Nuclear Technology*, **93**, 330 (1991).

[R-2] J. M. Ryskamp, F. C. Difilippo, R. T. Primm III, "Reactor Physiscs Methods for the Preconceptual Design of the Advanced Neutron Source," *Tran. of Am. Nuc. Soc.*, **57**, 290 (1988).

[R-3] E. L. Redmond, "Monte Carlo Methods, Models, and Application for the Advanced Neutron Source," M.S. Thesis, Department of Nuclear Engineering, Massachusetts Institute of Technology (June 1990).

[R-4] E. L. Redmond and A. F. Henry, "The Accuracy of Point Kinetics in Transient Analysis of the Advanced Neutron Source," Report, Department of Nuclear Engineering, Massachusetts Institute of Technology (September 1991).

[S-1] K. S. Smith, "An Analytical Nodal Method for Solving the Two-Group, Multidimensional, Static and Transient Neutron Diffusion Equations," M.S. and NE Thesis, Department of Nuclear Engineering, Massachusetts Institute of Technology (March 1979).

[S-2] D. L. Selby, R. M. Hamington, P. B. Thompson, "Advanced Neutron Source (ANS) Project Progress Report FY 1994," ORNL-6821 (January 1995).

[T-1] H. Trosman, "Computer Simulation for Transient Analysis of MITR Loop Components," M.S. Thesis, Department of Nuclear Engineering, Massachusetts Institute of Technology (May 1994).

[V-1] A. V. Vota, N. J. Curlee, Jr. and A. F. Henry, "WIGL3-A Program for the Steady-State and Transient Solution of the One-Dimensional, Two-Group, Space-Time Diffusion Equations Accounting for Temperature, Xenon and Control Feedback," WAPD-TM-788 (February 1969).

[Y-1] J. B. Yasinsky and A. F. Henry, "Some Numerical Experiments Concerning Space-Time Reactor Kinetics Behavior," *Nucl. Sci. Eng.*, **22**, 171 (1965).

[Y-2] G. L. Yoder *et al.*, "Steady-State Thermal Hydraulic Design Analysis of the Advanced Neutron Source Reactor," ORNL/TM-12398 (May 1994).

Appendix A

The Two-Element ANS Core

In this appendix, we give a description of the two-element ANS core and the results of the control-rod removal transients for this core.

A.1 Core Characteristics

The information given here is summarized from reference [R-1].

The Advanced Neutron Source Reactor with a peak unperturbed thermal flux of $\sim 8.5 \times 10^{19}$ $m^{-2}.s^{-1}$ was designed by Oak Ridge National Laboratory for condensed matter physics, material science, isotope production, and fundamental physics research. To meet the requirement of extremely high thermal flux over a large accessible volume, highly enriched fuel in a small core with heavy water moderator in the reflector was chosen. Heavy water was selected because it has the highest moderating to absorption ratio and permits greater flexibility for the orientation of the beam tubes as compared to solid moderators. An extremely high thermal flux cannot be obtained without high power density. To keep the total power as low as possible, small core volumes are desirable. Unfortunately, the required high power density results in high heat fluxes, presenting a major challenge to core cooling. This challenge was met by using thin fuel plates to produce a large heat transfer area per unit volume, a high coolant flow velocity, short heated lengths, and efficient hydraulic geometries. To allow the same low coolant inlet temperature for each fuel element, they were designed to be radially offset. The fuel elements were axially offset to create greater neutron leakage, which increases the reflector volume containing a high thermal neutron flux.

The characteristics of the reference two-element core are presented in Table A.1. Figure A.1 shows the core configuration. Figure A.2 illustrates how this two-element core was modelled by the *r-z* geometry nodal code ZAQ. Steady-state flux profiles found from a ZAQ solution are given in Figure A.3. As with the three element core, the origin *(1,1)* is at the lower central node of the reflector, and the plots are for 19 mesh spacings in the radial direction, and 48 mesh spacings in the axial direction.

Table A.1: Design characteristics of the two-element ANS core model (Taken from reference [R-1])

Quantity and unit/item	Baseline value/material
Heat deposited in fuel, MW	303
Fission power, end of cycle, MW(f)	330
Fission power, 1 day into cycle, MW	332
Peak reflector thermal flux, neutrons/(m^2/sec)	
Beginning-of-cycle	7.95×10^{19}
End-of-cycle	8.57×10^{19}
Core life, days	17
Core active volume, L	67.6
Fuel form	U_3Si_2
Fuel enrichment,%	93
Fuel matrix	Al
Volume % of fuel in fuel meat	11.2
Number of fuel plates in upper element	432
Number of fuel plates in lower element	252
Mass of ^{10}B, gm (beginning of cycle)	13
Fuel plate thickness, mm	1.27
Aluminum clad thickness, mm	0.254
Coolant channel gap, mm	1.27
Fuel span between side plates	
Upper element, mm	78.4
Lower element, mm	87.4
Fuel volume fraction in core	0.3
Coolant volume fraction in core	0.5
Cladding volume fraction in core	0.2
Coolant	D_20
Heated length, mm	507
Coolant velocity in core, m/s	25
Inlet pressure (in plenum), MPa	3.2
Core pressure drop, MPa	1.5
Core inlet temperature, °C	45
Core bulk outlet temperature, °C	83
Average surface heat flux, MW(core)/m^2	6.27
Average power density in fuel meat, MW(core)/L	16.44

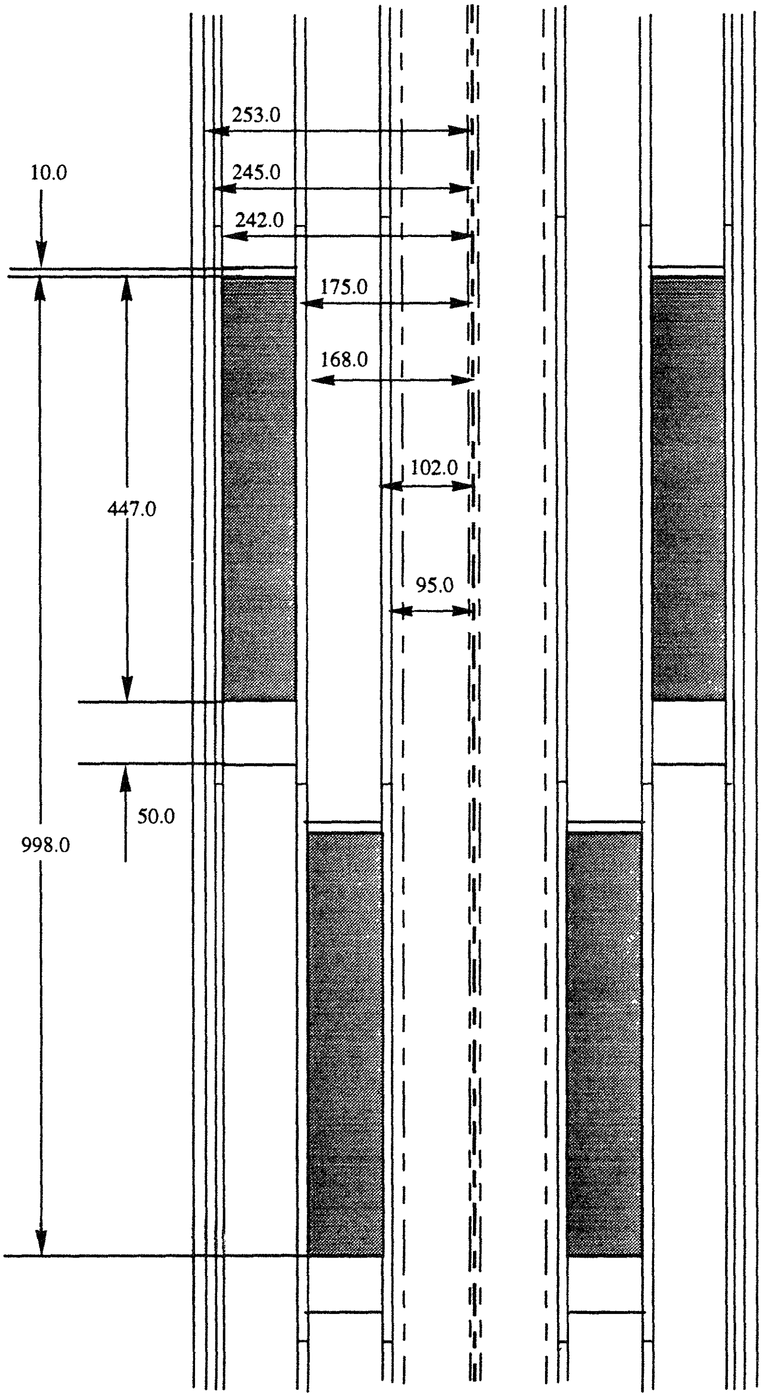

Figure A.1: Two-element ANS core configuration (dimensions are given in mm)

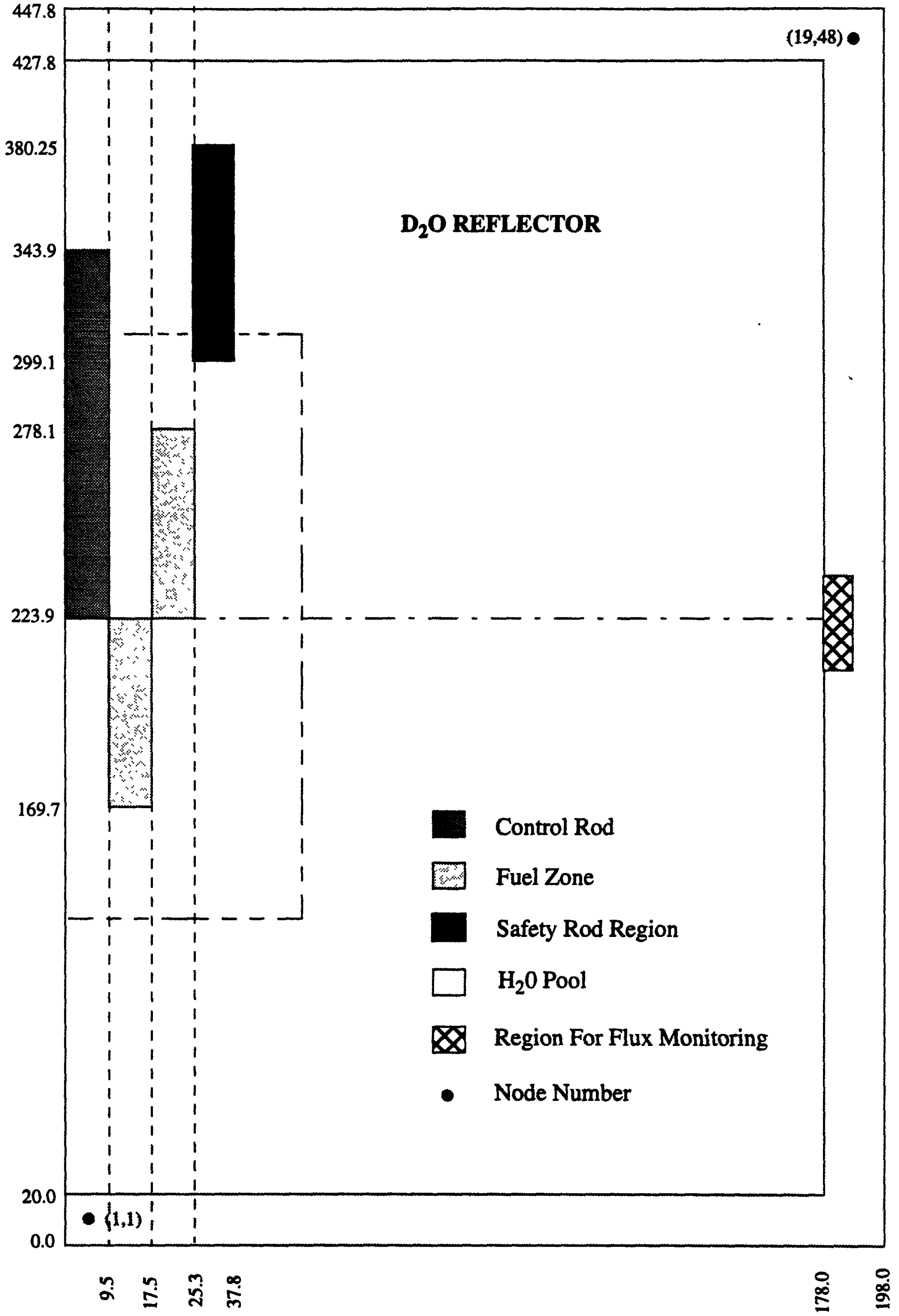

Figure A.2: Simplified R-Z geometry model of the two-element ANS core

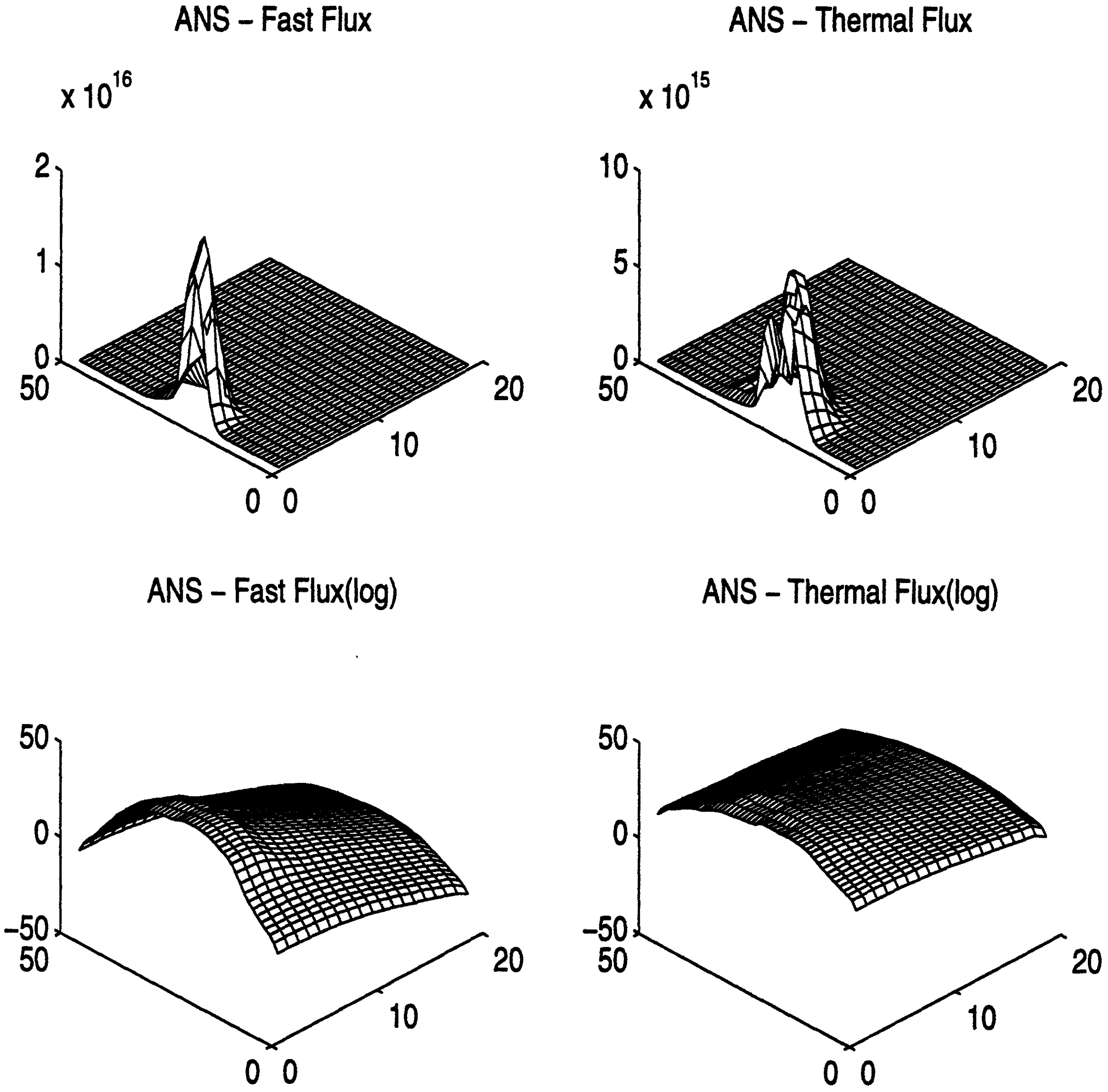
ANS - Fast Flux

ANS - Thermal Flux

ANS - Fast Flux(log)

ANS - Thermal Flux(log)

Figure A.3: Steady-state flux plots for the two-element ANS core

A.2 Results for the Two-Element ANS Core Transient Analysis

In this section results of the 10 second and 0.1 second control rod withdrawal transients are presented for the two-element ANS core. Feedback effects were not modelled.

The cross sections and discontinuity factor ratios required for the two-group ZAQ model were generated for 15 control rod positions from eight-group TWODANT calculations with P_0, S_4 approximations. That time at which the total flux reading in the outer H_2O detector nodes increases 15% over its full power nominal value was taken as the scram time.

A.2.1 Control Rod Removal in 10 seconds

In this slow transient one of the central control rods reaches the fully withdrawn position in 10 seconds. Figures A.4 and A.5 show the reactivity and power associated with this transient. Table A.2 presents the values of various quantities of interest at the time of scram for four different models. The results of the pseudo-static eigenvalue tests from the nodal and transport theory models are given in Tables A.3 and A.4 respectively.

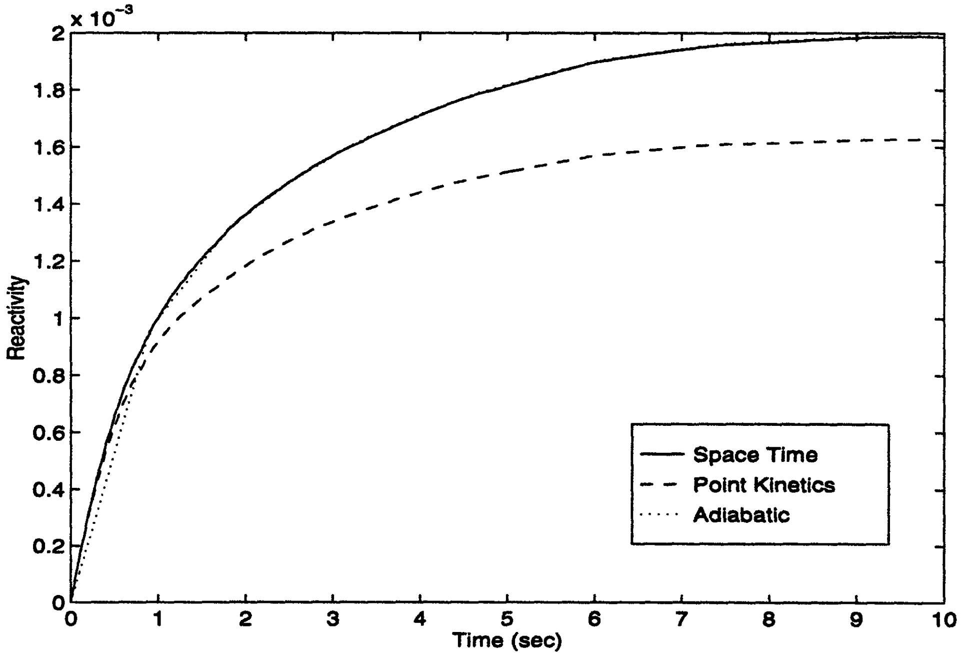

Figure A.4: Reactivity vs. time for the 10 second rod withdrawal transient for the two-element core

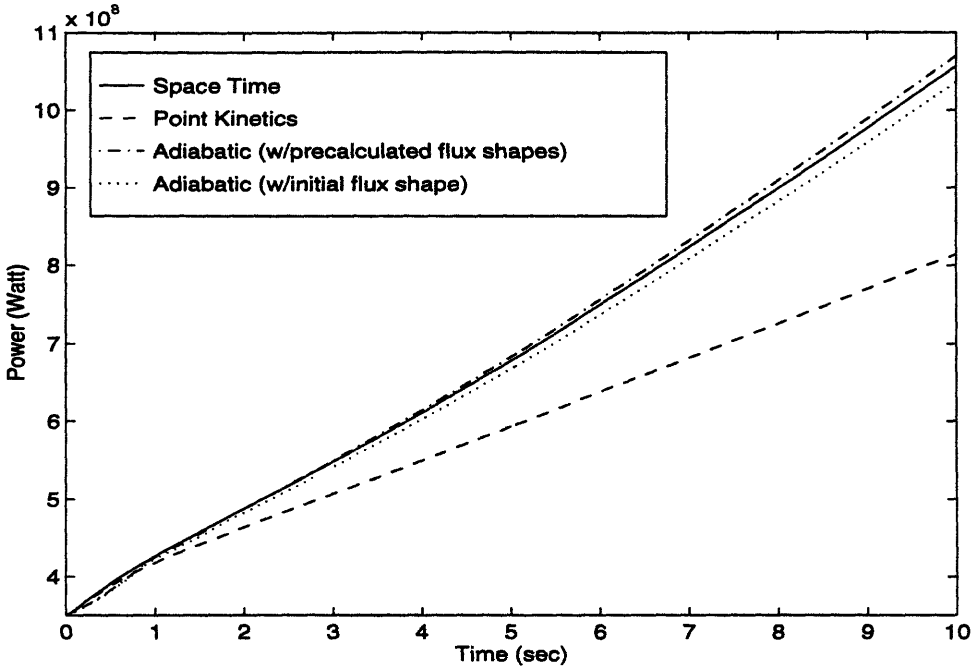

Figure A.5: Power vs. time for the 10 second rod withdrawal transient for the two-element core

Table A.2: Predictions by various models of parameters of interest at the time of 15% overpower scram for the 10 second rod withdrawal transient

Method	Scram Time (sec)	Reactor Power at the time of scram (MW)	Integrated Power at the time of scram (MJ)	Highest Powered Node Energy Accumulation (MJ)
Few-Group Nodal (Space-Time)	0.650	402.17	245.87	14.89
Point Kinetics	0.750	404.11	284.92	17.16
Adiabatic with Changing Flux Shape	0.725	401.61	270.68	16.39
Adiabatic with Initial Flux Shape	0.760	402.77	284.05	17.11

Table A.3: The two-group pseudo-static ZAQ eigenvalues for the 10 second rod withdrawal transient for the two-element ANS core

Time (sec)	Space Time			Point Kinetics	Adiabatic Ch. Flux[1]	Adiabatic Ini. Flux[2]
	Reference	$\omega_d=0$	$\omega_d=\omega_g=0$			
0.60	1.00002	1.00072	1.00075	1.00006	1.00014	1.00014
0.90	1.00002	1.00093	1.00095	1.00009	1.00003	1.00003
1.50	1.00001	1.00119	1.00121	1.00014	1.00003	1.00003
2.50	1.00000	1.00147	1.00147	1.00021	1.00001	1.00001
5.10	1.00000	1.00181	1.00182	1.00030	1.00000	1.00000
7.00	1.00000	1.00193	1.00194	1.00034	1.00000	1.00000
10.00	1.00000	1.00198	1.00199	1.00036	1.00000	1.00000

(1) Adiabatic approximation with changing flux shapes
(2) Adiabatic approximation with initial flux shape

Table A.4: The eight-group pseudo-static TWODANT eigenvalues for the 10 second rod withdrawal transient for the two-element ANS core

Time (sec)	Space Time		Point Kinetics	Adiabatic Ch. Flux[1]
	Reference	$\omega_d=0$		
0.60	1.00005	1.00076	1.00010	1.00017
0.90	1.00003	1.00095	1.00011	1.00005
1.50	1.00002	1.00121	1.00016	1.00006
2.50	1.00001	1.00147	1.00022	1.00002
5.10	1.00002	1.00184	1.00033	1.00003
7.00	1.00002	1.00195	1.00036	1.00002
10.00	1.00003	1.00200	1.00038	1.00002

(1) Adiabatic approximation with changing flux shapes

A.2.2 Control Rod Removal in 0.1 seconds

Figures A.6 and A.7 show the reactivity and power vs. time for a transient during which one of the three central control rods is completely withdrawn in 0.1 seconds. Notice that for both the slow and fast transients of the two-element ANS core, since the magnitude of the positive reactivity inserted is less than β_{eff}, the reactor newer becomes super-prompt critical. The control rod worth seems to be too low. These calculations allow us to examine the model for transients that are mild compared to the three-element core transients. In Table A.5 various parameters of the transients at the time of scram are compared. The pseudo-static test results are presented in Tables A.6 and A.7.

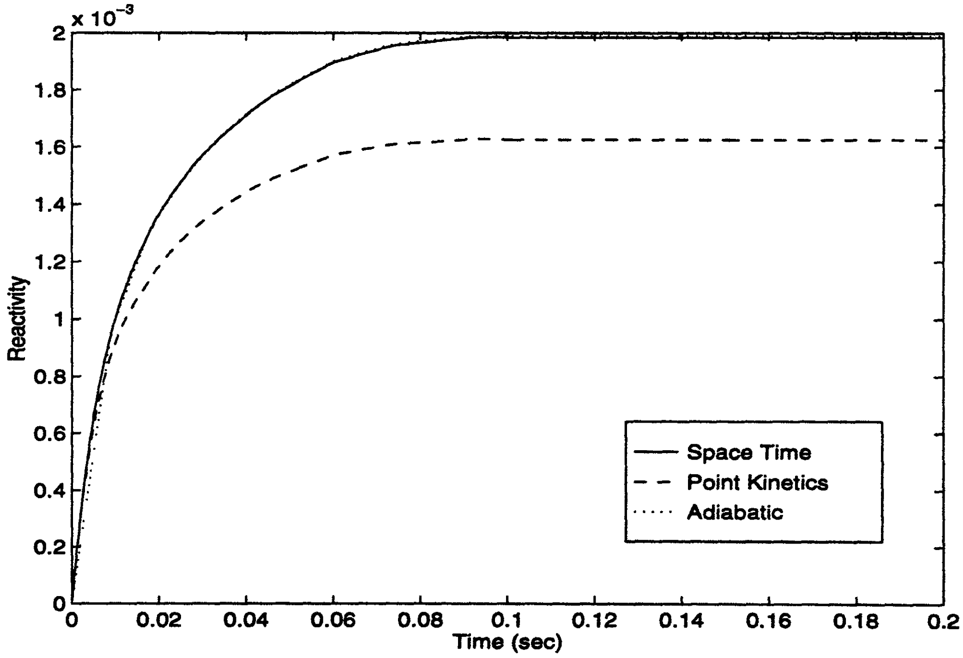

Figure A.6: Reactivity vs. time for the 0.1 second rod withdrawal transient for the two-element core

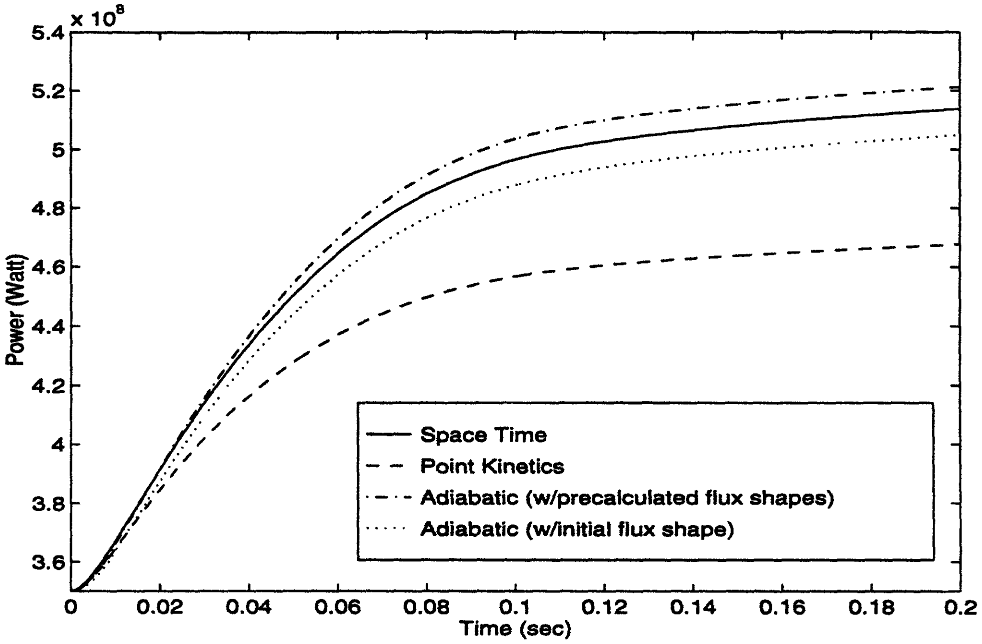

Figure A.7: Power vs. time for the 0.1 second rod withdrawal transient for the two-element core

Table A.5: Predictions by various models of parameters of interest at the time of 15% overpower scram for the 0.1 second rod withdrawal transient

Method	Scram Time (sec)	Reactor Power at the time of scram (MW)	Integrated Power at the time of scram (MJ)	Highest Powered Node Energy Accumulation (MJ)
Few-Group Nodal (Space-Time)	0.0285	410.93	10.78	0.66
Point Kinetics	0.0305	402.87	11.45	0.68
Adiabatic with Changing Flux Shape	0.0240	401.65	8.94	0.54
Adiabatic with Initial Flux Shape	0.0270	403.23	10.08	0.60

Table A.6: The two-group pseudo-static ZAQ eigenvalues for the 0.1 second rod withdrawal transient for the two-element ANS core

Time (sec)	Space Time			Point Kinetics	Adiabatic Ch. Flux[1]	Adiabatic Ini. Flux[2]
	Reference	$\omega_g=0$	$\omega_d=0$			
0.006	1.00002	1.00061	1.00015	1.00002	1.00004	1.00007
0.009	1.00006	1.00075	1.00026	1.00012	0.99996	0.99999
0.015	0.99987	1.00058	1.00050	1.00020	1.00007	1.00008
0.025	1.00005	1.00067	1.00086	1.00027	1.00007	1.00009
0.051	1.00001	1.00037	1.00147	1.00029	1.00004	1.00005
0.070	1.00002	1.00026	1.00171	1.00037	1.00000	1.00002
0.100	1.00005	1.00014	1.00189	1.00035	1.00011	1.00011
0.200	0.99999	1.00002	1.00197	1.00040	1.00008	1.00008

(1) Adiabatic approximation with changing flux shapes
(2) Adiabatic approximation with initial flux shape

Table A.7: The eight-group pseudo-static TWODANT eigenvalues for the 0.1 second rod withdrawal transient for the two-element ANS core

Time (sec)	Space Time		Point Kinetics	Adiabatic Ch. Flux[1]
	Reference	$\omega_g=0$		
0.006	1.00008	1.00065	1.00009	1.00012
0.009	1.00013	1.00078	1.00019	1.00005
0.015	0.99994	1.00060	1.00025	1.00013
0.025	1.00009	1.00067	1.00031	1.00012
0.051	1.00006	1.00039	1.00033	1.00008
0.070	1.00005	1.00027	1.00039	1.00004
0.100	1.00007	1.00016	1.00038	1.00014

(1) Adiabatic approximation with changing flux shapes

Appendix B

The Three-Element ANS Core

In this appendix, we give the description of the three-element ANS core, and present the details of the reactor model used in our calculations.

B.1 Core Characteristics

In the most recent ANS studies, three-element core configurations were considered as a means of increasing the core volume to allow the use of lower enriched fuel. By holding the core power constant and operating at a lower power density, an increase in the core volume allowed the use of lower enriched fuels (enrichment reduced from 93% to 50%) while simultaneously permitting an increase in the cycle length (from 17 days for the two-element core to 30 days for the three-element core) [S-2]. Various arrangements of the three elements onto a single core were examined by the ANS project. The design in which the two upper elements overlapped 100% was selected for further neutronic analysis and design studies since it has the best neutronic performance. However, as a result of increased core volume, the thermal flux in the reflector vessel decreases. So the thermal flux for the three-element core is lower than that for the two-element configuration.

Table B.1 shows the basic core characteristics of this design. The core configuration is given in Figure B.1 and B.2.

Table B.1: Design characteristics of the three-element ANS core model (Taken from [G-4])

Quantity and unit/item	Baseline value/material
Heat deposited in fuel, MW	303
Fission power, end of cycle, MW(f)	~330
Fission power, 1 day into cycle, MW	~330
Peak reflector thermal flux, neutrons/(m^2/sec) Beginning-of-cycle[1]	4.72×10^{19}
Core life, days	31
Core active volume, L	79.6
Fuel form	U_3Si_2
Fuel enrichment,%	50
Fuel matrix	Al
Volume% of fuel in fuel meat	11.2
Number of fuel plates in upper element	571
Number of fuel plates in center element	252
Number of fuel plates in lower element	418
Mass of ^{10}B, gm (beginning of cycle)	13
Fuel plate thickness, mm	1.27
Aluminum clad thickness, mm	0.254
Coolant channel gap, mm	1.27
Fuel span between side plates	
Inner, mm	77.65
Middle, mm	63.95
Outer, mm	55.41
Coolant	D_20
Heated length, mm	418
Coolant velocity in core, m/s	20
Inlet pressure (in plenum), MPa	2.7
Core pressure drop, MPa	0.9
Core inlet temperature, °C	45

(1) From the two-group ZAQ calculation

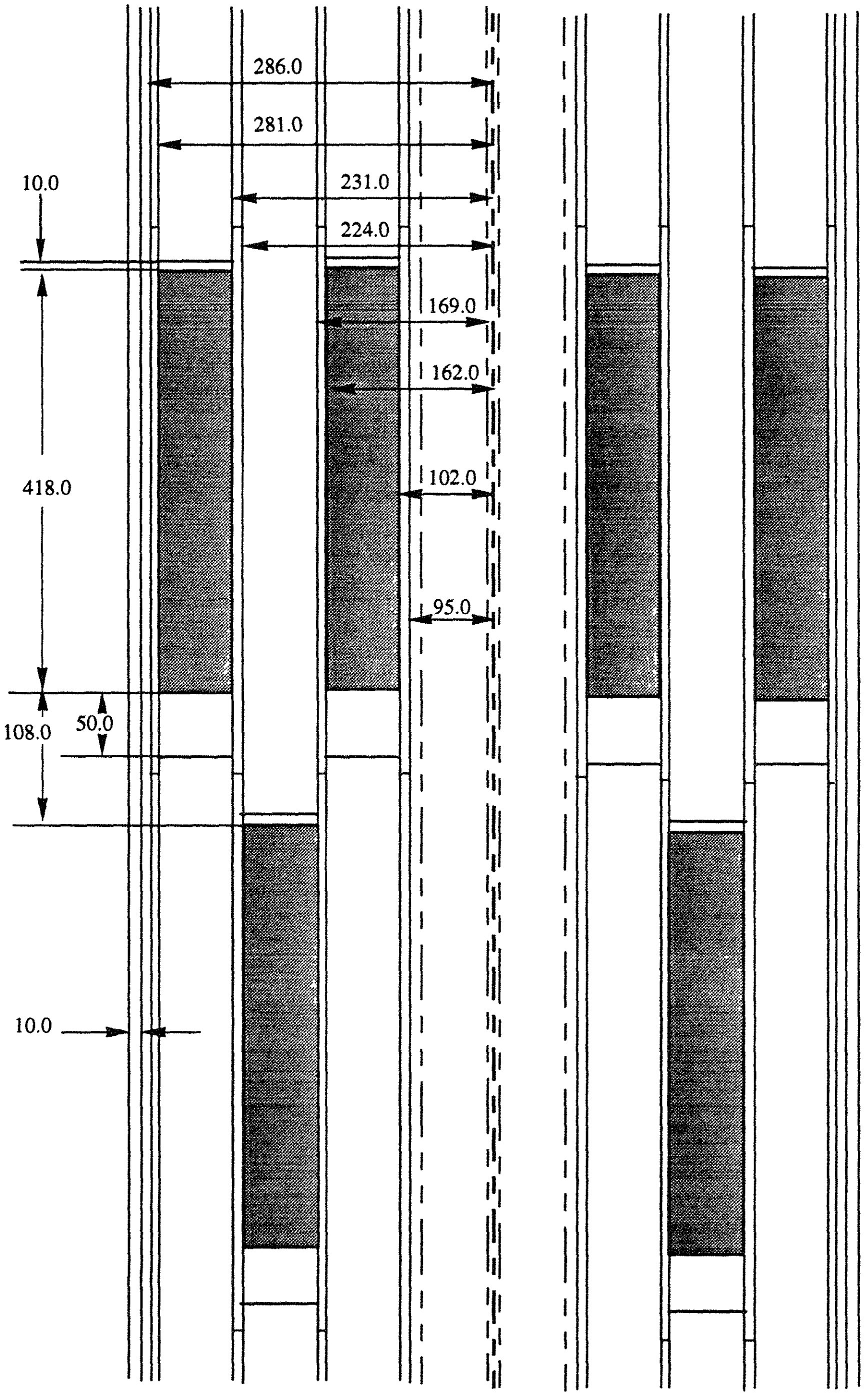

Figure B.1: The three-element ANS core configuration (dimensions are given in mm)

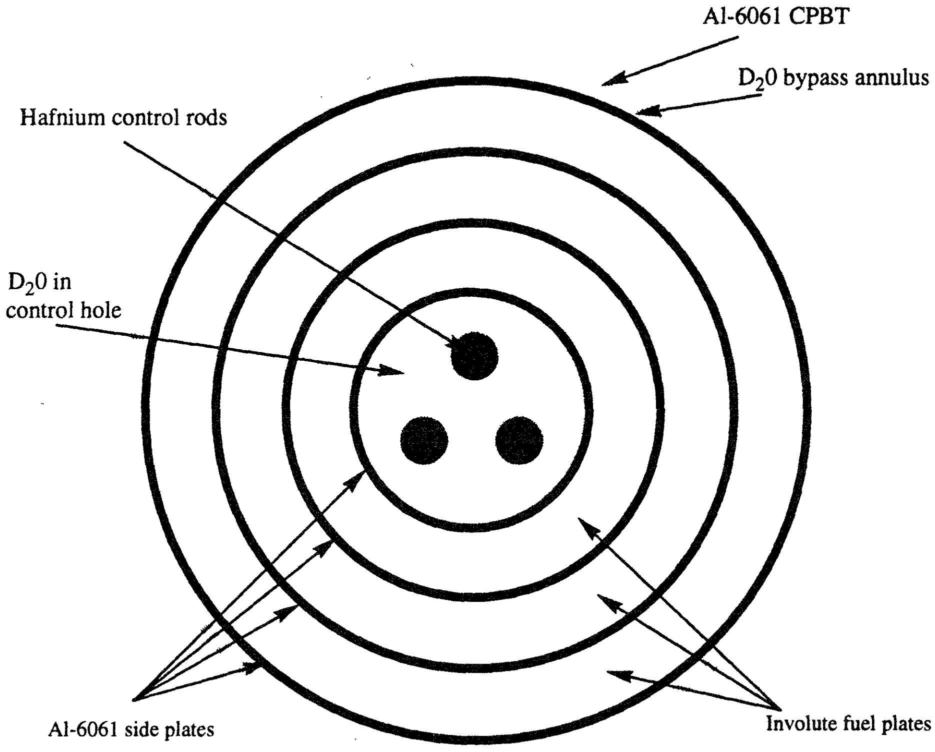

Figure B.2: Cross section of the three-element ANS core

B.2 The three-element ANS core ZAQ model

Geometry:

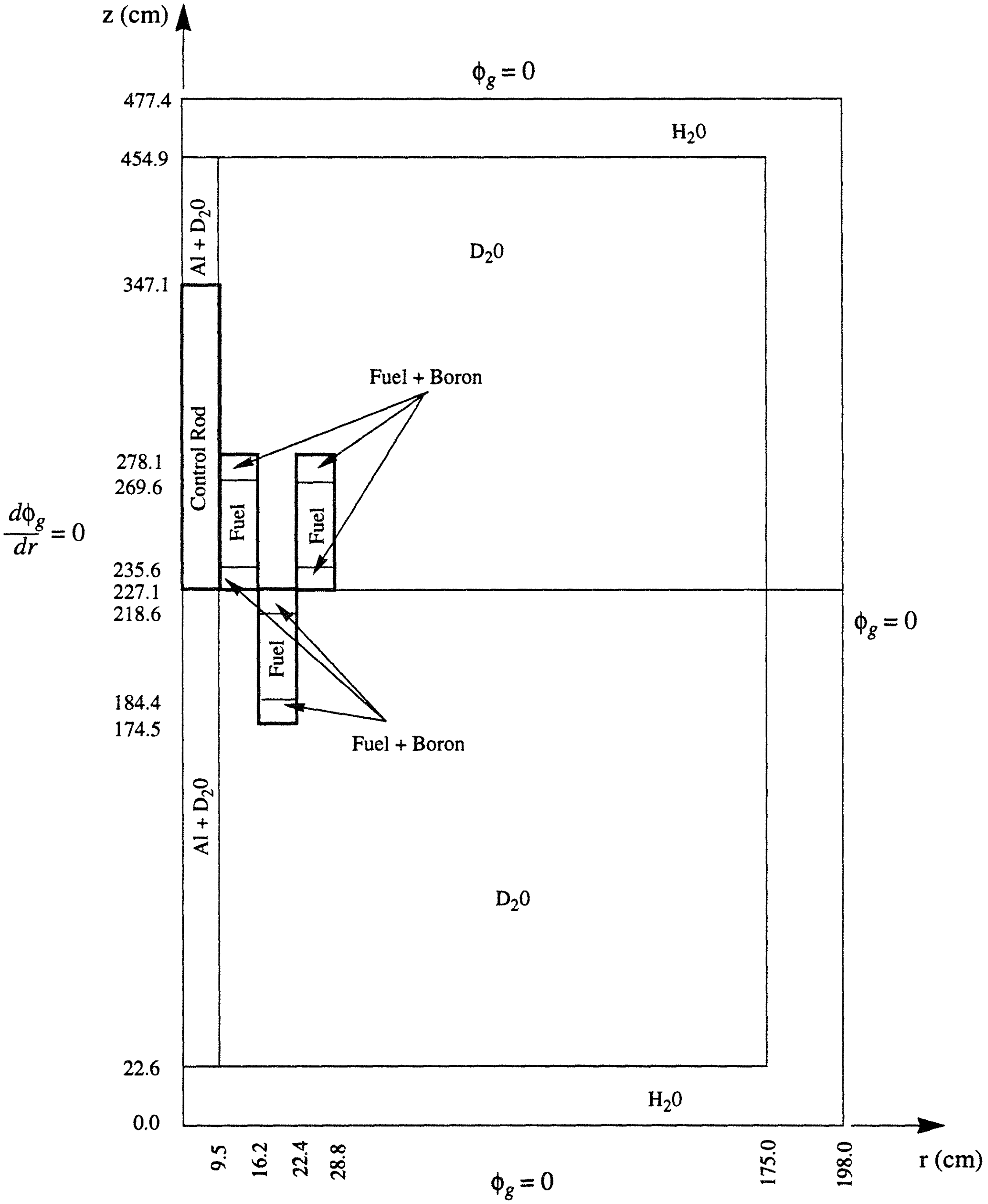

Material Properties:

Because each node (19x48) in the model has its own cross section and discontinuity factor ratio sets, they are not given.

Energy Group Structure:

Group g	Upper Energy (eV)	Lower Energy (eV)	υ_g (cm/s)	χ_g
1	$2.00\text{x}10^7$	$9.00\text{x}10^5$	$2.0186\text{x}10^9$	0.731
2	$9.00\text{x}10^5$	$1.00\text{x}10^5$	$6.7937\text{x}10^8$	0.255
3	$1.00\text{x}10^5$	$1.00\text{x}10^2$	$4.9264\text{x}10^7$	0.014
4	$1.00\text{x}10^2$	$3.00\text{x}10^0$	$5.9128\text{x}10^6$	0.000
5	$3.00\text{x}10^0$	$6.25\text{x}10^{-1}$	$1.7003\text{x}10^6$	0.000
6	$6.25\text{x}10^{-1}$	$2.70\text{x}10^{-1}$	$8.8095\text{x}10^5$	0.000
7	$2.70\text{x}10^{-1}$	$1.00\text{x}10^{-2}$	$4.1009\text{x}10^5$	0.000
8	$1.00\text{x}10^{-2}$	$1.00\text{x}10^{-5}$	$1.0157\text{x}10^5$	0.000

$\chi_1 = 1.0$

$\chi_2 = 0.0$

Two-group speeds are reduced from eight-group using space dependent spectrum

Delayed Neutron Data:

Family, d	β_d	λ_d (s^{-1})
1	$2.64470\text{x}10^{-4}$	0.0133
2	$1.32845\text{x}10^{-3}$	0.0325
3	$1.13600\text{x}10^{-3}$	0.1219
4	$2.37677\text{x}10^{-3}$	0.3169
5	$1.20761\text{x}10^{-3}$	0.9886
6	$6.16701\text{x}10^{-4}$	2.9544

Thermal-Hydraulic Parameters:

C_f = 199.0 + 0.104T (T in °C) J/kg/K

C_{clad} = 1,051.0 J/kg/K

$C_{coolant}$ = 4,300.0 J/kg/K

ρ_f = 1.20×10^4 kg/m^3

ρ_{clad} = 2.71×10^3 kg/m^3

k_f = 170.0 W/m-K

k_{clad} = 180.7 W/m-K

W = 547.04, 746.48, 884.10 kg/m^2 *(Inner, Middle, Outer Fuel Elements)*

h = 100,000 J/m^2/s

r = 0.03

Pressure = 2.4 MPa

Coolant Inlet Temperature = 45°C

Initial Power = 330.0 MW$_{th}$

Appendix C

Thermal-Hydraulic Model

C.1 Fuel Heat Transfer Model

The model described here was developed by Meyer [M-1]. Recently it has been used in MIT Research Reactor Simulation by Trosman [T-1]. The following derivation is taken from the second reference.

The heat conduction equation for the fuel plate illustrated in Figure 5.1.b is given by

$$(mC_p)_p \frac{dT_p}{dt} = q'' - U_p(T_p - T_b) \tag{C.1}$$

where

T_b = bulk coolant temperature,

T_p = average plate temperature,

U_p = plate overall heat transfer coefficient,

q'' = plate surface heat flux

The plate mass per unit surface area, m_p, and the average heat capacity of the fuel plate, $(C_p)_p$, are defined as fallows:

$$m_p = \frac{A_{fuel}}{P_T}\rho_{fuel} + \frac{A_{clad}}{P_T}\rho_{clad} \tag{C.2}$$

$$(C_p)_p = \frac{(mC_p)_{fuel} + (mC_p)_{clad}}{m_p} \tag{C.3}$$

where A is cross sectional surface area of the fuel and clad, P_T is the total outside perimeter of the fuel plate, and ρ is density.

Assuming the steady-state arithmetic average temperature can be used to represent the energy storage, and that the thermal conductivities and capacities are uniform in the plate, the average fuel plate temperature is calculated by using:

$$T_p = \frac{(mC_p)_{clad}(T_f+T_c)_{fuel} + (mC_p)_{fuel}(T_{center}+T_f)}{2(mC_p)_p} \tag{C.4}$$

where

T_f = fuel meat surface temperature

T_c = clad surface temperature

T_{center} = fuel meat centerline temperature.

Two temperature ratios, f_p and f_1 are defined as fallows:

$$f_p = \frac{T_p - T_c}{T_{center} - T_c} \tag{C.5}$$

and

$$f_1 = \frac{T_f - T_c}{T_{center} - T_c} \tag{C.6}$$

Substituting Equation (C-5) and (C-6) into (C-4) results in the following expression

$$f_p = \frac{(mC_p)_p f_1 + (mC_p)_f}{2(mC_p)_p} \tag{C.7}$$

Making the steady-state assumption, and expressing the fuel surface heat flux for the fuel, the clad and the entire plate, and doing some algebraic manipulations yield the temperature ratios and the overall heat transfer coefficient:

$$f_1 = \frac{U_T}{U_{clad}} \tag{C.8}$$

$$\frac{1}{U_p} = \frac{1}{h_p} + \frac{f_p}{U_T} \tag{C.9}$$

where h_p is the film heat transfer coefficient and

$$\frac{1}{U_T} = \frac{1}{U_{clad}} + \frac{1}{U_{fuel}} = \frac{t}{k_{clad}} + \frac{d}{2k_{fuel}}$$

d = the fuel meat thickness,

t = clad thickness.

Once the heat transfer parameters are defined, the heat conduction equation (C.1) can be solved and average fuel plate temperature, T_p^n, at any time step can be found. Finally, the plate surface temperature is related to the average plate temperature as follows:

$$T_c^n = T_p^n - \left[(q'')^n \left(\frac{f_p}{U_T} \right) \right]. \tag{C.10}$$

The model described above was used to modify the heat transfer coefficient appearing in Equations (5.1) and (5.2). (Notice that, because of a difference in notation, the term replaced by U_p is $1/U + 1/h_0$ in these equations and T_f in Equations (5.1) and (5.2) is used for T_p.)

In Figure C.1, for 100% step increase in the core power, the lumped model is compared against a two-region (fuel and clad) model. The core average fuel temperatures from the two different calculation are 5 to 6 degree apart. Notice also that the asymptotic temperatures are attained in ~0.1 seconds.

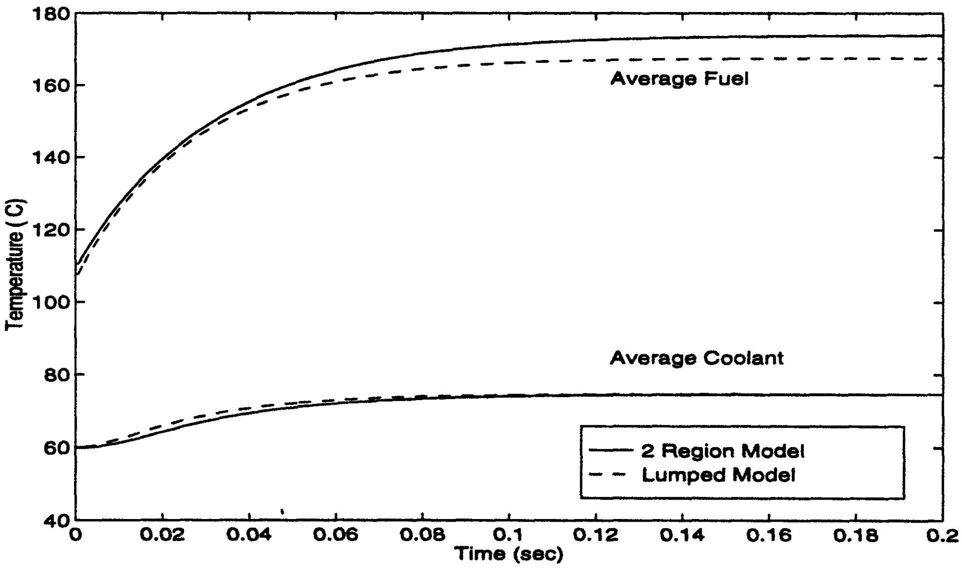

Figure C.1: Core average fuel and coolant temperatures response to 100% step increase in the core power

C.2 Single-Phase Forced-Convection Heat Transfer Coefficient

The single phase-heat transfer coefficient, h_p, in Equation (C.9) is determined by the

Petukhov and Popov correlation with some modifications for variable physical properties and rectangular channels [Y-2]. The coefficient is determined as follows:

$$h_p = \frac{k_b}{D_e} \frac{(f_d/8) Re_b Pr_b (\mu_b/\mu_w)^{0.11}}{(1+3.4f_d) + \left[11.7 + \frac{1.8}{Pr_b^{1/3}}\right] (f_d/8)^{1/2} \left(Pr_b^{2/3-1}\right)} \qquad \text{(C.11)}$$

where

h_p = forced-convection heat transfer coefficient (kW/m^2.K)
k_b = bulk coolant thermal conductivity (kW/m.K)
D_e = equivalent channel diameter (m),
f_d = Darcy friction factor,
Re_b = bulk coolant Reynolds number,
Pr_b = bulk coolant Prandtl number,
μ_b= bulk coolant dynamic viscosity (Pa.s),
μ_w = wall dynamic viscosity (Pa.s);

with the Filenenko correlation used for the Darcy friction factor:

$$f_d = \frac{[1.0875 - 0.1125(b/s)]}{(1.82 \log_{10} Re_b - 1.64)^2}, \qquad \text{(C.12)}$$

where

b = gap of a rectangular channel or annulus (m),
s = span of a rectangular channel (m).